

Experimental and numerical investigations of convective cooling configurations for gas turbine combustors

Von der Fakultät Luft- und Raumfahrttechnik und Geodäsie
der Universität Stuttgart zu Erlangung der Würde eines
Doktor-Ingenieurs (Dr.-Ing.) genehmigte Abhandlung

von

Dipl.-Ing. Michael Maurer
aus Herbolzheim im Breisgau

Hauptberichter:	Prof. Dr. Jens von Wolfersdorf
Mitberichter:	Prof. James R. Ferguson, PhD, PE
Tag der mündlichen Prüfung:	09.01.2008

Institut für Thermodynamik der Luft- und Raumfahrt (ITLR)
Universität Stuttgart

Stuttgart 2008

D93

Acknowledgements

First and foremost I would like to thank my advisor, Professor Dr. Ing. Jens von Wolfersdorf, deputy of the Institute of Aerospace Thermodynamics (ITLR) at the Universität Stuttgart. Back in my days as an engineering student, he already encouraged me to come back to the institute after I would have finished my diploma thesis and take the opportunity to work in a scientific project, which proved to be challenging and interesting. In addition, he gave me the chance to present results of my scientific work at several international conferences.

I want to thank Prof. Dr. Ing. habil. Bernhard Weigand, head of the Institute of Aerospace Thermodynamics, for helpful discussions. He was always willing to spend time with me and supported my project with his expertise. I am also indebted to Prof. James R. Ferguson, PhD, PE. Knowing the immense workload, he was willing to act as an examiner without hesitation.

In addition, I gratefully acknowledge the financial support provided within the research and innovation initiative KW21 by the Ministry of Baden-Württemberg, Germany and ALSTOM Power. I am indebted to all people, which made this research program possible. Also, I owe special thanks to Dr. Michael Gritsch from ALSTOM. During several meetings, the main goals of my project were discussed and clarified. With his support, he helped me to complete all tasks successfully.

Furthermore, I am very grateful to have met Dipl.-Ing. Rico Poser. He was my room mate within the last three years. He managed to simplify the post-processing of my experimental data, so that a lot of time and a great deal of annoyances could be spared. Without him and his support, my life at the ITLR would not have been so enjoyable. This holds also true for all colleagues, which I met at the ITLR.

As described within this dissertation, experimental setups had to be constructed and built. Despite his immense workload, I'm glad that I have met Mr. Harald Hettrich at ITLR. I owe him special thanks for his support in all kinds of design issues. In my opinion, the realization of the test rig was only possible due to the handy work of our maintenance team. Among others, I would like to point out Mr. Heinz Maschke, Mr. Christian Otto and Mr. Eberhard Meyer from the mechanical shop and Mr. Thomas Bertnik and Mr. Uli Schwaderer, our electricians.

To come to an end, I must not forget to thank Mrs. Waltraud Wurster, our secretary. She always supported me in all kinds of administrative issues. It was a pleasure to work with her.

Finally, I would like to express my great gratitude to my parents. With their support throughout my education, they made all this possible.

Bad Säckingen, February 2008

Michael Maurer

Abstract

Within the present study, experiments and numerical computations are conducted to analyze the cooling performance of different convective cooling techniques for backside cooled combustor walls. For all investigated configurations, the pressure loss and the heat transfer enhancement is observed. As possible candidates for a convective cooling scheme, rib turbulators, channels with dimples and channels with hemispheres are considered.

The data bases for such convective cooling techniques, which have already been reported in literature, arise from the experience in internal blade cooling. Compared to the typical conditions found for backside cooled combustor walls, the Reynolds number and the mass flow rates are lower in the case of internal blade cooling. Additionally, the ribs or other convective cooling techniques are applied to two opposite channel walls within the blade. For backside cooled combustor walls, the heat transfer on only one channel wall needs to be enhanced.

For the experimental setup, several measurement techniques are applied. The heat transfer coefficient between two successive ribs is obtained with a steady and a transient measurement technique. A comparison of the two measurement techniques is also provided. Averaged heat transfer coefficients on the rib itself are measured by using the lumped heat-capacitance method.

For the numerical setup, the commercial solver FLUENTTM is applied together with two different turbulence models. In the case of rib turbulators, a standard k- ϵ turbulence model is used. It could be demonstrated that for dimpled surfaces or surfaces with hemispheres, a Reynolds Stress Model performs better. In general, the experimental results are underpredicted, whereas the trends are predicted correctly. It is concluded, that the present numerical approach is applicable to preliminary design studies.

One result of this study is to extend the Reynolds number range of typical rib turbulators to Reynolds number levels found in backside cooled combustor walls. In contrast to internal blade cooling, the design requirements of a backside cooled combustor wall are a moderate pressure loss at higher Reynolds numbers and at the same time a good heat transfer enhancement. It could be demonstrated, that the geometry of rib turbulators need to be adjusted to satisfy the mentioned design requirements.

The investigations on V-shaped, W-shaped and WW-shaped ribs revealed the following fact. The existence of a second ribbed wall has an influence on the heat transfer of the opposite wall. It is therefore suggested not to directly use heat transfer correlations, which are derived from experimental data of two-sided ribbed channels, for the design of one-sided ribbed channels.

Additionally, it could be demonstrated, that for higher Reynolds numbers the rib height has to be reduced to obtain lower levels of pressure losses. As the rib geometry is changed from V-shaped to W-shaped rib, the pressure losses are increased for an equal rib spacing and rib height. WW-shaped ribs resulted in even higher pressure losses. For V-shaped and W-shaped ribs, a reduction of the rib spacing leads to a lower pressure loss. For WW-shaped ribs, an opposite trend is observed.

In the case of W-shaped ribs, the heat transfer enhancement on the rib itself is obtained. It could be demonstrated that a reduction of the rib spacing has no impact on the heat transfer enhancement on the rib. A combination of the heat transfer data between two successive ribs and the data on the rib reveals, that heat transfer levels of around three times higher than the heat transfer of a smooth channel wall are realized for the investigated Reynolds number range.

The possibility to replace the commonly used rib turbulators with dimples or hemispheres is also addressed in this study. For channels with hemispheres or dimples on one channel wall, a lower pressure loss and at the same time only moderate heat transfer enhancement levels are observed.

For the design of a convective cooling technique for convectively cooled combustor walls, W-shaped ribs should be preferred. This configuration shows the best thermal performance for the typical Reynolds numbers found in backside cooled combustor walls. In cases, where the convective cooling has to be achieved with very low pressure losses, dimpled channels represent an interesting alternative to ribbed configurations.

Zusammenfassung

Die vorliegende Arbeit umfasst experimentelle und numerische Untersuchungen von konvektiven Kühlkonfigurationen, die in konvektiv gekühlten Brennkammerwänden von stationären Gasturbinen eingesetzt werden. Dabei wurden für alle Konfigurationen Druckverluste und Wärmeübergangserhöhungen gegenüber glatten Kanälen ermittelt.

Bisher werden solche Kühlkonfigurationen vornehmlich zur internen Kühlung von Turbinenschaufeln benutzt. Die dort vorherrschenden Massenströme sind allerdings geringer wie die in einer konvektiv gekühlten Brennkammerwand. Darüber hinaus werden in der internen Schaufelkühlung meist zweiseitig berippte Kanäle eingesetzt. Bei konvektiv gekühlten Brennkammerwänden besteht jedoch nur der Bedarf eine Kanalwand intensiv zu kühlen. Es stellt sich also die Frage, wie gut man die existierenden Korrelationen von zweiseitig berippten Kanälen zur Auslegung von einseitig berippten Kanälen verwenden kann. Es ist weiterhin festzustellen, dass der in der Literatur untersuchte und bekannte Parameterbereich bisher nicht ausreichend bzw. nur unzureichend ist für eine Auslegung einer konvektiv gekühlten Brennkammerwand.

Ziel dieser Arbeit ist es, den Wertebereich für bereits bekannte Kühlkonfigurationen hin zu höheren Reynolds Zahlen zu erweitern und in einem weiteren Schritt, die gängigen Konfigurationen durch die Änderung der Geometrie an den erweiterten Reynolds-Zahlen Bereich anzupassen. Als eine gängige Methode werden zunächst Rippen genutzt, um den Wärmeübergang in internen Kanälen anzuheben. Innerhalb dieser Studie wurde auch untersucht, ob die berippten Kanäle, welche nun für den neuen Reynolds-Zahlen Bereich optimiert sind, durch Kanäle mit so genannten Dimples oder durch Kanäle mit gleichmäßig verteilte Hemisphären ersetzt werden können.

Für die Ermittlung der Wärmeübergänge wurden verschiedene Messmethoden angewendet. Zunächst wurde der Wärmeübergang mit einer stationären Messmethode untersucht, später wurden die Experimente mit einer transienten Methode durchgeführt. Es konnte an einer Kühlkonfiguration gezeigt werden, dass die Ergebnisse unabhängig von der gewählten Messmethode sind.

Für die numerische Simulation wurde das kommerzielle Programm FLUENTTM verwendet. Es kamen zwei Turbulenzmodelle zum Einsatz. Die berippten Kanäle wurden mit einem standard k- ϵ Turbulenzmodell simuliert. Für die Kanäle mit Dimples und die Kanäle mit gleichmäßig verteilten Hemisphären wurde eine Re-Spannungs Modell angewendet. Für alle Simulationen waren die numerischen Ergebnisse für den Wärmeübergang unterhalb der experimentell gewonnenen Daten zu finden. Die tendenziellen Trends bei einer Änderung der Geometrie wurden richtig vorhergesagt. Es konnte gezeigt werden, dass die gewählte Vorgehensweise der numerischen Simulation für eine erste Designstudie ausreichend ist. Werden genauere Daten gebraucht, erscheint

es im Moment noch nicht möglich, diese mit einem vertretbaren Zeitaufwand numerisch zu ermitteln.

Die Untersuchungen der V-förmigen, W-förmigen und WW-förmigen berippten Kanäle ergaben folgende Schlüsse. Das Vorhandensein einer zweiten berippten Wand hat einen Einfluss auf den Wärmeübergang der gegenüberliegenden Wand. Daher sollten Korrelationen, welche auf der Datenbasis von zweiseitig berippte Kanäle entstanden sind, nicht direkt auf einseitig berippte Kanäle angewendet werden.

Es wurde gezeigt, dass bei höheren Reynolds-Zahlen die Rippenhöhe verringert werden sollte, damit die entstehenden Druckverluste reduziert werden können. Bei gleich bleibender Rippenhöhe und bei gleichen Rippenabständen erhöht sich der Druckverlust, wenn von V-förmigen Rippen zu W-förmigen Rippen übergegangen wird. WW-förmige Rippen erzielen im Vergleich zu W-förmigen Rippen noch höhere Druckverluste. Wird der Rippenabstand halbiert, so sinken im Fall von V-förmigen und W-förmigen Rippen die Druckverluste. Für WW-förmige Rippen ereignet sich das Gegenteil.

Im Fall der W-förmigen Rippen wurde auch der Wärmeübergang auf der Rippe selbst ermittelt. Es zeigte sich, dass eine Halbierung des Rippenabstands keinen Einfluss auf die Höhe des Wärmeübergangs auf der Rippe hat. Werden die Wärmeübergangsdaten auf der Rippe und zwischen den Rippen kombiniert, so lassen sich für W-förmige Rippen dreimal so hohe Wärmeübergänge realisieren im Vergleich zum Wärmeübergang eines glatten Kanals.

Die Untersuchung von Kanälen mit Dimples ergab, dass die Druckverluste noch einmal reduziert werden konnten im Vergleich zu den berippten Kanälen. Jedoch kann mit dieser Kühlkonfiguration nicht der gleiche Wärmeübergang realisiert werden. Die Werte für den Wärmeübergang liegen unterhalb der berippten Kanäle.

Für die Kanäle mit Hemisphären ergab sich ein ähnliches Bild. Im Vergleich zu Kanälen mit Dimples sind die Druckverluste jedoch höher bei einer gleichzeitig nur geringen Steigerung des Wärmeübergangs.

Für die Auslegung einer rein konvektiv gekühlten Brennkammerwand kann somit empfohlen werden, W-förmige Rippen zu verwenden. Diese Geometrie erreicht bei den typischen Reynolds-Zahlen die höchste Kühleffektivität in einem Kanal mit einem Seitenverhältnis von 2:1. Sollte ein sehr geringer Druckverlust eine entscheidende Rolle bei der Auslegung spielen, so stellen die Kühlkanäle mit Dimples eine interessante Alternative zu den berippten Kanälen dar.

Table of Content

Acknowledgements	i
Abstract	iii
Zusammenfassung	v
Nomenclature	ix
1 Introduction	1
1.1 The stationary gas turbine	1
1.2 Gas turbine combustors	4
1.3 Combustor cooling concepts	6
1.4 Motivation and literature review	9
2 Experimental setup	17
2.1 Test facility	17
2.2 Test section	18
2.3 Pressure loss measurements	20
2.4 Thermochromic liquid crystals (TLC)	22
2.5 Steady measurement technique	25
2.6 Transient measurement technique	28
2.7 Lumped heat-capacitance method	32
3 Numerical setup	37
3.1 Purpose of computational fluid dynamics (CFD)	37
3.2 Fundamentals of CFD	37
3.3 CFD computations of turbulent flows	38
3.4 Grid generation	40
3.5 FLUENT TM	42
4 Rib turbulators	45
4.1 V-shaped ribs (steady measurement technique)	45

4.2 V-shaped ribs (transient measurement technique)	56
4.3 V-shaped ribs (Real geometry effects)	63
4.4 W-shaped ribs (transient measurement technique)	67
4.5 W-shaped ribs (lumped heat-capacitance technique)	73
4.6 WW-shaped ribs (transient measurement technique)	77
4.7 Conclusions on ribbed cooling channels	83
5 Dimples	89
5.1 Dimples with $H/D = 4$	89
5.2 Dimples with $H/D = 0.5, 1, 2$	99
5.3 Conclusions on Dimples	101
6 Hemispheres	103
6.1 Hemispheres with $L/d_0 = 2, 3, 4, 5$	103
6.2 Conclusions on channels with hemispheres	110
7 Conclusions	113
Literature	117
Appendix	123
A PIV measurement	123
B Error analysis	126
Resume	133

Nomenclature

Latin letter symbols

AR	aspect ratio AR = W/H	[-]
A	channel cross section	[m ²]
A _{FOIL}	surface area of heater foil	[m ²]
A _{curvature}	surface area of surface with curvature	[m ²]
A _{projected}	surface area of projected flat surface	[m ²]
A _w	surface area	[m ²]
Bi	Biot number, Bi = he/k	[-]
c _f	loss coefficient of inlet nozzle c _f = 0.992	[-]
c	specific heat capacity	[J/kgK]
c _p	specific heat capacity at constant p	[J/kgK]
c _{p,w}	specific heat capacity of Perspex at constant p	[J/kgK]
D	dimple imprint diameter	[m]
D _h	hydraulic diameter	[m]
d ₀	hemisphere diameter	[m]
e	rib height	[m]
f	friction factor	[-]
H	channel height	[m]
h	heat transfer coefficient on flat surface	[W/(m ² K)]
h _{CURV}	heat transfer coefficient on curved surface	[W/(m ² K)]
k	hemisphere height	[m]
k _{AIR}	thermal conductivity of air	[W/mK]
k _w	thermal conductivity of Perspex	[W/mK]
l	ribbed channel length or channel length covered with dimples or hemispheres	[m]

L	spacing of hemispheres	[m]
\dot{m}	air mass flow	[kg/s]
m	mass	[kg]
Nu	Nusselt number	[-]
	$Nu = hD_h/k_{AIR}$	
\overline{Nu}	area averaged Nusselt number	[-]
P	rib pitch	[m]
P_{FOIL}	electrical power of heater foils	[W]
p	pressure	[Pa]
Δp_{NOZ}	pressure difference $\Delta p = p_\infty - p_{NOZ}$	[Pa]
$\Delta p/\Delta x$	regression line gradient of pressure distribution	[Pa/m]
Pr	Prandtl number of air	[-]
Q_{CON}	convective heat flow	[W]
Q_{RAD}	heat flow due to heat radiation	[W]
\dot{q}_{CON}	convective heat flux at surface	[W/m ²]
\dot{q}_{CLOSS}	heat flux losses due to convection	[W/m ²]
\dot{q}_{RLOSS}	heat flux losses due to radiation	[W/m ²]
R	radius of dimple or hemisphere	[m]
R_{EL}	heater foil resistance	[Ω]
Re_D	Reynolds number based on the hydraulic diameter	[-]
	$Re_D = \rho D_h u_{AVG}/\mu$	
Re_y	turbulent Reynolds number based on the wall distance	[-]
s	entropy	[J/(kgK)]
t	time	[s]
T	temperature	[°C] or [K]
T_B	bulk temperature of air flow	[°C] or [K]
T_W	local wall temperature	[°C] or [K]
T_{TLC}	temperature of Thermochromic Liquid Crystals	[°C] or [K]
T_0	initial temperature of air flow	[°C] or [K]
U_{EL}	voltage potential across heater foils	[V]

u_{AVG}	mean velocity	[m/s]
u^+	dimensionless velocity in wall coordinates $u^+ = u_{AVG} / \sqrt{\tau_w / \rho}$	[-]
V	volume	[m ³]
w	velocity	[m/s]
W	channel width	[m]
x	test section x-coordinate	[m]
X_i	body force acting in x_i -direction	[N/m ³]
y	test section y-coordinate	[m]
y^+	dimensionless wall distance $y^+ = (\tau_w \rho)^{0.5} y / \mu$	[-]
z	test section z-coordinate	[m]

Greek letter symbols

α	rib angle	[°]
β	thermal expansion coefficient	[1/K]
δ	dimple depth	[m]
ε	emmissivity	[-]
η	thermal performance $\eta = (\overline{Nu}_R / Nu_0) / (f / f_0)^{1/3}$	[-]
η_{th}	thermal efficiency	[-]
μ	dynamic viscosity of air	[kg/(ms)]
ρ	density of air	[kg/m ³]
ρ_w	density of Perspex	[kg/m ³]
Θ_{RIB}	dimensionless temperature gradient $\Theta_{RIB} = \frac{T_{RIB} - T_0}{T_B - T_0}$	[-]
Θ_w	dimensionless temperature gradient $\Theta_w = \frac{T_w - T_0}{T_B - T_0}$	[-]
σ	Stefan-Boltzmann constant	[W/(m ² K ⁴)]

τ	discrete time points	[s]
τ_w	shear stress at wall	[Pa]
Φ	dissipation function	[-]

Subscripts

CAR	refers to conditions found at Carnot process
CURV	evaluated on surfaces with curvature
BRAYTON	refers to conditions found at Brayton process
MAX	evaluated at global maximum
MEAS	refers to condition found at measurement location
MIN	evaluated at global minimum
NOZ	evaluated at tightest cross section of inlet nozzle
PROJ	evaluated on projected flat surfaces
R	evaluated at roughened channel wall
RIB	evaluated at aluminum rib
0	evaluated at fully developed flow in a smooth channel
∞	evaluated at ambient conditions

Acronyms

HSL	The HSL color space stands for Hue, Saturation and Lightness
ITLR	Institute of Aerospace Thermodynamics
RGB	The RGB color model stands for Red, Green and Blue
RSM	Reynolds stress model
skε	Standard k-ε turbulence model
TLC	Thermochromic Liquid Crystals

1 Introduction

1.1 The stationary gas turbine

In contrast to jet propulsion, stationary gas turbines power plants are built to produce electrical power. Since the beginning of stationary gas turbine design, a maximized electrical output for a given actual cost is desired. Nowadays not only commercial interests define the design process, also environmental “costs” seem to more and more dictate the final design.

The basic thermodynamic cycles

Any stationary gas turbine consists of at least four major components. At the inlet, the air flow enters the compressor (C). The pressure ratio of actual gas turbine compressors varies from 10 to 35 (e.g. the pressure ratio for ALSTOM’s GT 26 is 33.9). After the compressor air is led to the combustion chamber (B), where the chemical reaction of air and the added hydrocarbon fuel leads to a significant rise in fluid temperature. The maximum fluid temperature in the combustor is around 2000 K as reported by Schulz [54]. Leaving the combustor the air is expanded in the turbine (T). Here, a part of the heat energy is converted into work. The resulting rotational energy drives the shaft and powers the attached compressor and a generator (G). The generator transfers the remaining momentum power to electrical power. A sketch of a typical gas turbine layout is presented in Fig. 1.1.

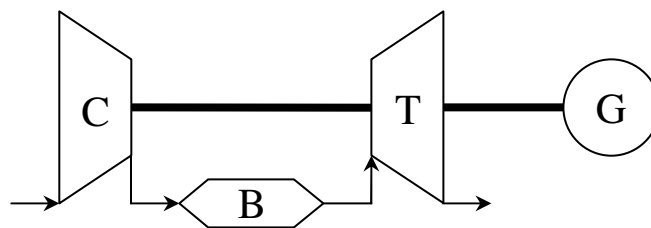


Fig. 1.1: Sketch of a basic stationary gas turbine layout (CBT)

From a thermodynamic point of view, any thermal engine is operating between two temperature reservoirs. The lower temperature boundary T_{\min} is often the environment, whereas the upper temperature limitation T_{\max} is defined by material restrictions. Several cycles are known to operate between two temperature reservoirs. First and foremost the Carnot cycle has to be mentioned. This cycle is known for its high thermal efficiency, because all heat is transferred at the maximum and minimum temperature respectively [28]. This reversible cycle is presented in Fig. 1.2a and the thermal efficiency is given as:

$$\eta_{th,CAR} = 1 - \frac{T_1}{T_3} = 1 - \frac{T_{\min}}{T_{\max}} \quad (1.1)$$

The basic cycle of a stationary gas turbine (CBT) is well described by the so called open Brayton cycle (or Joule cycle), which has been described among others by Schulz [54]. Fig. 1.2b presents this reversible cycle in the temperature-entropy diagram. The work of the compressor is represented by an isotropic compression from $1 \rightarrow 2$. The combustion process can be ideally treated as an isobaric heat addition from $2 \rightarrow 3$. This is different to the Carnot cycle, where the heat addition is isothermal. But this isothermal behavior can not be easily realized by technical applications. The relaxation of the fluid in the turbine is represented by an isotropic expansion from $3 \rightarrow 4$. The thermal efficiency of the reversible Brayton cycle is given as:

$$\eta_{th,BRAYTON} = 1 - \frac{T_1}{T_2} = 1 - \frac{T_{\min}}{T_2} \quad (1.2)$$

The thermal efficiency of a Brayton cycle is always lower than a Carnot cycle operating between similar thermal boundaries, because T_2 is always below T_{\max} . Another fact is that the thermal efficiency of the reversible Brayton cycle is simply defined by the compressor ratio from $1 \rightarrow 2$.

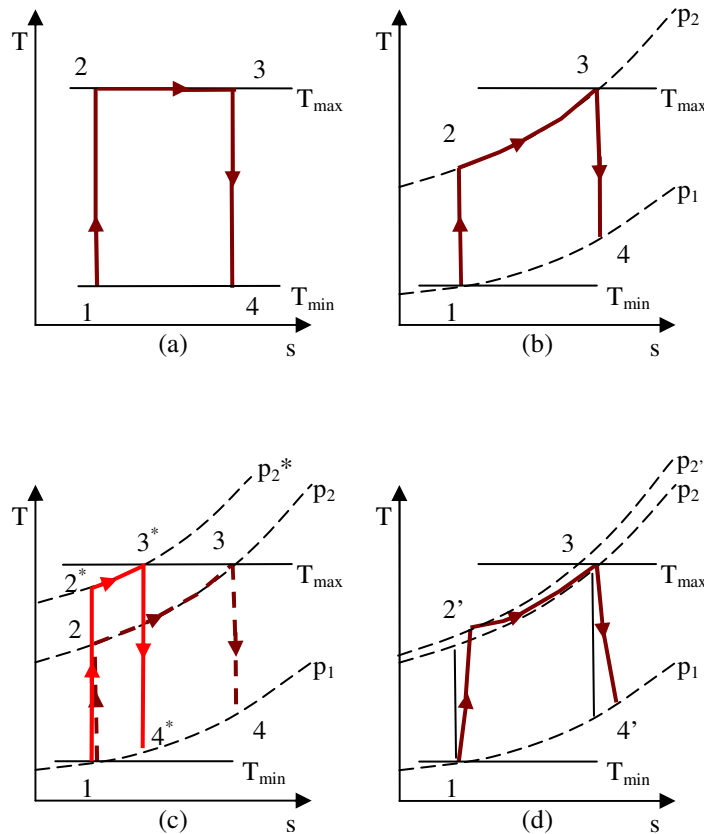


Fig. 1.2: T,s diagrams for (a) a reversible open Carnot cycle, (b) a reversible open Brayton cycle, (c) an adjusted reversible open Brayton cycle and (d) an irreversible open Brayton cycle

For the adjusted reversible open Brayton process (1-2*-3*-4*), as presented in Fig. 1.2c, the working cycle has a higher pressure ratio in the compressor. Based on equation (1.2), the thermal efficiency of the adjusted cycle is higher compared to the open Brayton cycle as presented in Fig. 1.2b. It appears that with an even higher pressure ratio, T_2^* could get close to the value of T_3 , which would lead to a thermal efficiency close to the Carnot cycle. Nevertheless, such a working cycle is of a theoretical nature, because the net heat load, which can be added in the combustor, is significantly reduced. The working output of such a cycle would be close to zero, keeping in mind that the enclosed area by the cycle represents the amount of work output. There are several technical solutions, how a higher compressor ratio can be reasonably used to obtain enhanced thermal efficiencies for a given maximum temperature. One of them is the so-called reheat process, which is described in the following section.

Looking at the irreversible Brayton cycle in Fig. 1.2d performance losses in the gas turbine components aren't neglected. The isentropic changes are now polytropic changes, taking account of the entropy enhancement due to an irreversible process. Also a pressure loss in the combustor is included. As a consequence, the thermal efficiency of an irreversible Brayton cycle as reported in [28] and [37] becomes more complex compared to the thermal efficiency of a reversible Brayton cycle. For the reversible Brayton cycle, the thermal efficiency also depends on the maximum temperature, the losses in the compressor and the turbine and the pressure loss in the combustor. A lower pressure drop in the combustor increases the thermal efficiency. Therefore, the choice of a combustor cooling technique will influence the thermal efficiency of a stationary gas turbine.

Advanced gas turbine design concepts

Besides gas turbines, which operate along the basic gas turbine cycle, the thermodynamic processes can be modified to increase the thermal efficiency or the working output. Hence, modern stationary gas turbines can show variations on the Brayton cycle. In the reheat cycle the turbine is divided into a high pressure turbine (HPT) and a low pressure turbine (LPT). Between the two turbine stages a second combustor provides an increasing fluid temperature (Fig. 1.3).

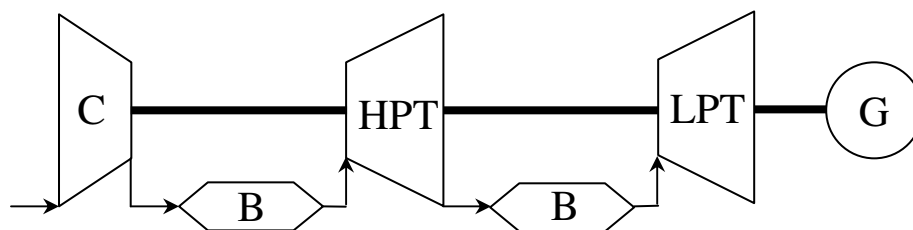


Fig. 1.3: Sketch of reheat gas turbine layout (CBTBT)

The thermodynamic cycle of such a reheat process is presented in Fig. 1.4a and a practical example is shown in Fig. 1.4b. The benefit of this cycle compared with the simple Brayton cycle is an increased working output, while the same maximum

temperature T_{\max} is preserved. Keeping in mind, that the pressure losses in the combustor influences the thermal efficiency, the application of two combustors doubles the influence combustor cooling techniques.

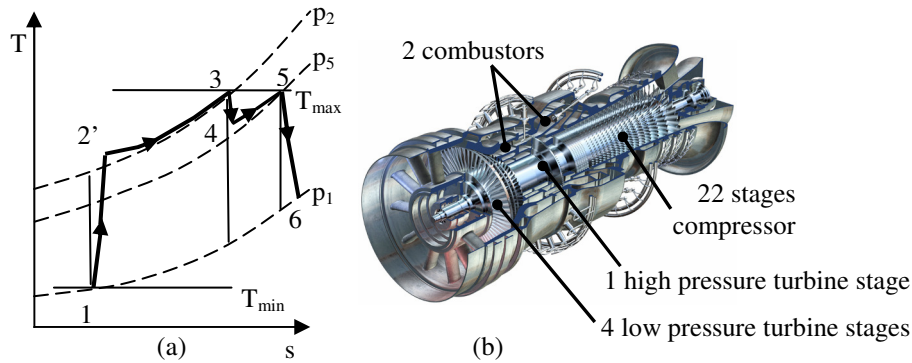


Fig. 1.4: (a) T,s -diagram for reheat cycle and (b) reheat heavy-duty gas turbine (ALSTOM GT26)

Another interesting fact is a higher turbine outlet temperature compared to the simple Brayton cycle. This makes this cycle more attractive for combined cycle gas turbine plants (CCGT), where the hot exhaust gas is used to produce water steam. The steam is utilized to power a steam turbine, which can be either linked to a separate generator (multi-shaft combined cycle gas turbine plants), or is attached to the gas turbine's generator (single-shaft combined cycle gas turbine plants). With a thermal efficiency of about 60% [16] these power plants are a common alternative to other power plants.

In some gas turbine combustion concepts the steam vaporized by the hot exhaust is injected directly into the combustor of the gas turbine for emission control and increased power output. In contrast to the combined cycle gas turbine plants mentioned before, with this concept a steam turbine is not required. A simple steam boiler is used to provide the steam. Due to the steam injection the thermal efficiency and the maximum working output can be increased, whereas the installation cost of such a power plant is reduced due to the economized steam turbine. Unfortunately, it has been reported in [28] and [37] that the thermal efficiency is limited to 45-52% and is therefore below the reachable thermal efficiency of a combined cycle power plant.

1.2 Gas turbine combustors

During the development in stationary gas turbine design, several gas turbine combustor types have been developed, each having their advantages and disadvantages. An overview of the different combustor designs is presented in Fig. 1.5.

Early stationary gas turbines were equipped with a single or with two silo combustors [37]. A big silo combustor is equipped with a single diffusion burner. The combustion of the injected fuel leads to a relatively high flame temperature, so that the combustor walls close to the primary flame zone have to be cooled intensively. This is achieved by providing a film of cooling air at the combustor wall facing the flame. The backside of

the silo combustor chamber is additionally cooled with convective cooling. Due to the length of the combustor a long residence time of the reacting components is the result. This can lead to low amounts of unburned hydrocarbons but high levels of nitrogen oxides. The intense application of film cooling quenches the burning process near the wall, increasing the production of unburned hydrocarbons in the close wall region. To date, this combustor design is not used anymore in modern gas turbines. Only for the combustion of difficult to burn fuels this combustor design is still relevant due to its stable combustion behavior.

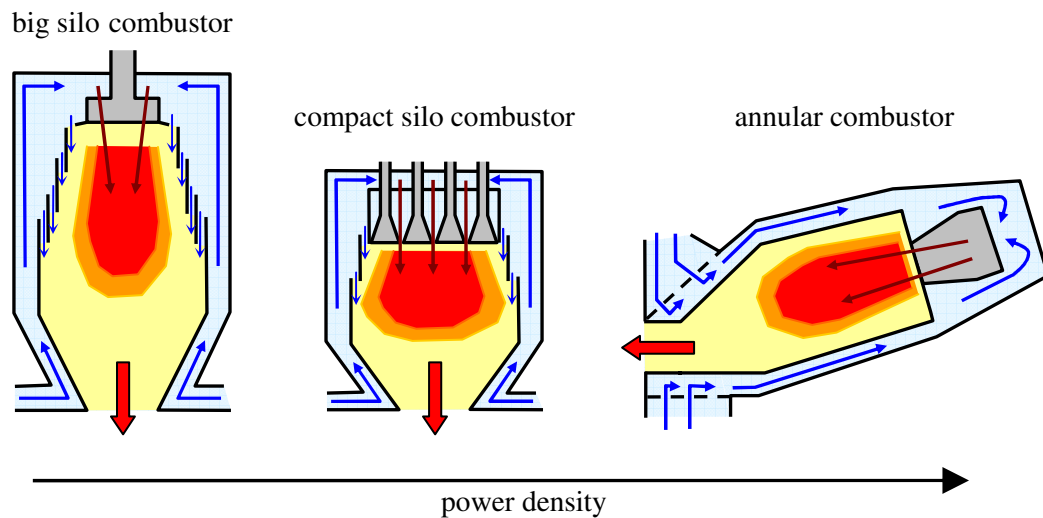


Fig. 1.5: Different combustor design concepts

An advanced approach to realize silo combustors is found in the compact silo combustor design. Here, the single diffusion burner is replaced by a larger number of burners. With this design a lean pre-mixed combustion concept is feasible, which has the advantage of a lower flame temperature. Therefore, the amount of film cooling air can be reduced and more compressor air is directly available for the lean air-fuel mixture. The compact design reduces the residence time, which has together with the lower flame temperature a reduced impact on the undesired nitrogen oxides production. In addition, silo combustors have the disadvantage of non-uniform temperature distributions and high temperature peaks at the turbine inlet due to non-annular exit of the combustion chamber outlet.

To obtain a more homogenous temperature distribution at the turbine inlet an annular combustion chamber is necessary. The power density is tripled compared to silo combustors [54]. Also the residence time of the reacting gases in the combustion chamber is reduced, leading to lower nitrogen oxides emissions. Looking at the cooling concept of this combustor type, the usage of film-cooling with its negative effects on the production of unburned hydrocarbon emissions and CO in the near wall regime is avoided. Therefore, the liner cooling air is kept fully available for the combustion process. The amount of compressor air available for lean and premixed combustion has increased from 30% as typically found in early gas turbines to 80% [16]. The combustor

walls are backside cooled using efficient convective cooling techniques. At positions with high thermal loads impingement cooling is also found. To provide the necessary heat resistance of the combustor wall material, highly heat-resistant nickel-based alloys are used together with thermal barrier coatings or ceramic coatings on the inner combustor wall.

Another type of annular combustor concept has been established in some industrial modern gas turbines. The annular combustor is replaced by a number of combustor cans. The benefits are a better maintenance of the single combustor can and that the experimental investigation of the fluid and temperature field of the single combustor is simplified compared to annular combustors in the development phase. Looking at the cooling aspect, this concept increases the combustor wall area and, therefore, enhances the overall cooling demands compared to a fully annular combustor [48].

1.3 Combustor cooling concepts

In principle, the heat transfer from a surface is always a combination of heat radiation and forced convection, due to the distinct flow field situation on the inside and outside of a combustion chamber wall.

The level of heat flow due to heat radiation Q_{RAD} is mainly defined by the temperatures of all involved surfaces, the geometry, the surface properties and the existence of emitting gases. Within the infrared band emitting gases as CO, CO₂, H₂O and CH₄ are found in the combustion process [5]. The influence of heat radiation on the overall heat transfer rises with an increasing temperature level and with an increasing temperature difference. Therefore, heat radiation should not be neglected for an assessment of the heat transfer situation on a combustor wall facing the combustion process. Otherwise, for investigations of the heat transfer condition on the outer combustor wall, which is attached to a cooling channel, the heat radiation is in most cases neglected.

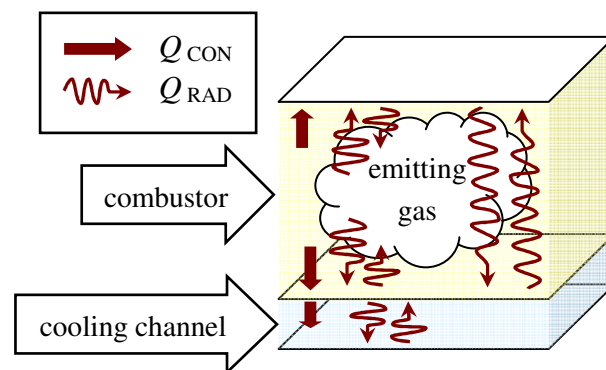


Fig. 1.6: Heat flow situation in a combustor and a cooling channel

The level of heat flow initiated by forced convection Q_{CON} is defined by the temperature difference between wall temperature T_{W} and mass-averaged fluid temperature T_{B} . An increased wall area A_{W} amplifies the total heat transferred, as does

the magnitude of the heat transfer coefficient h , which is proportional to the dimensionless temperature gradient at the wall. The heat transfer coefficient has high magnitudes for sharp temperature gradients. This relationship is defined as:

$$Q_{CON} = hA_W(T_B - T_W) \quad (1.3)$$

A sketch of the heat flow situation is presented in Fig. 1.6.

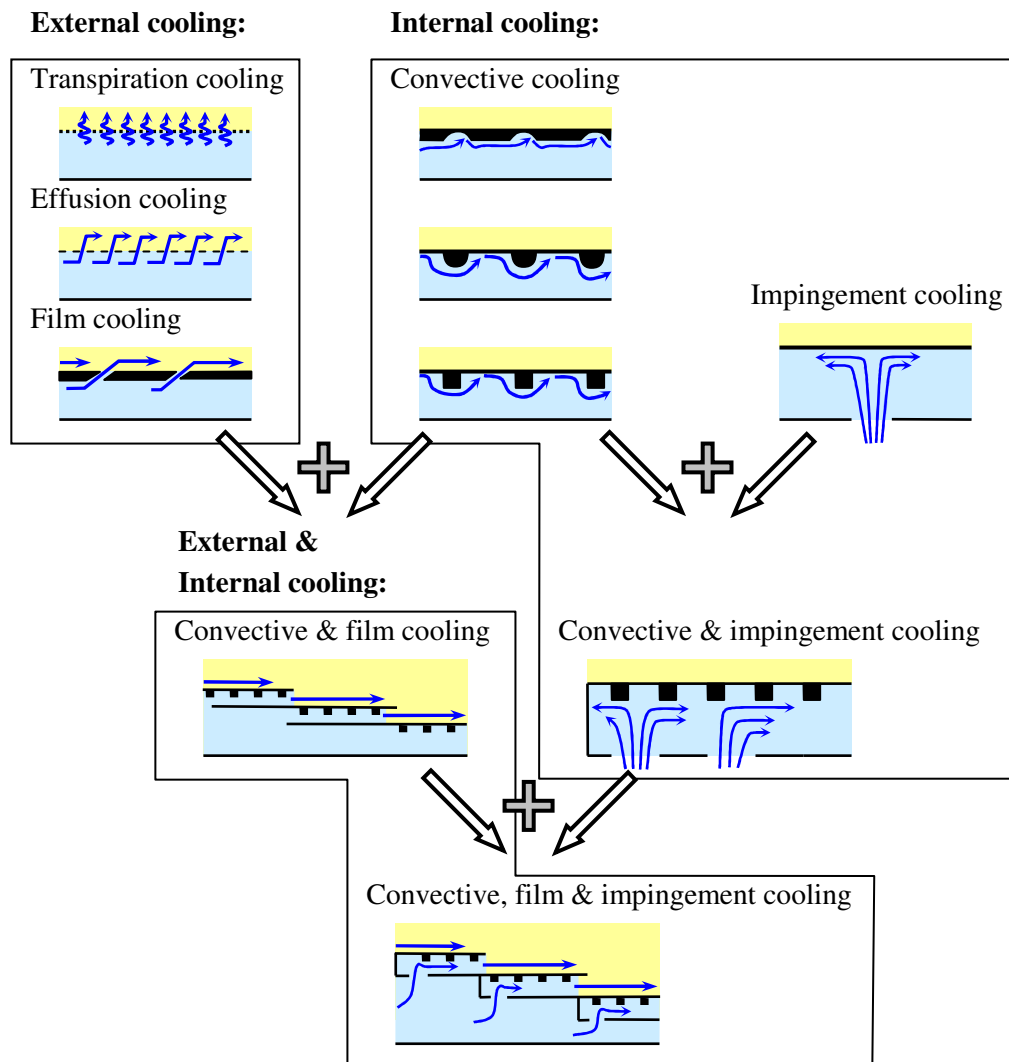


Fig. 1.7: Overview of different liner cooling concepts

There are many different cooling concepts available to protect the combustor wall from the hot flow inside the combustor. All enhanced cooling techniques have a disturbed boundary layer in common. In fundamental literature, it is distinguished between internal and external heat transfer techniques. The classification depends on the location of the boundary layer alteration. If the boundary layer is disturbed at the wall facing the cooling channel, the description is internal cooling. If the boundary layer is altered on the combustion chamber surface e.g. due to a coolant film, the appropriate name would

be external cooling. An overview of the different combustor cooling techniques and their classification into internal and external cooling is presented in Fig. 1.7.

External heat transfer

External cooling techniques are film, effusion and transpiration cooling. The basic idea is to reduce the heat flow into the surface. Therefore, a cool mass flow is transferred from the cooling channel to the opposite hot surface. This mass flow typically increases the turbulence level of the boundary layer, which results in an undesired enhancement of the heat transfer coefficient. Otherwise a layer of coolant is created close to the surface, if the momentum of the exiting mass flow is below the separation limit. This lowers the driving temperature difference for the convective heat transfer, leading to a reduced heat flow. Challenges in this technical field are to minimize the mass flow required to provide an intact coolant layer close to the surface.

In the case of film cooling the coolant is lead through thin slots or drilled holes. Current investigations suggest using fan-shaped holes for their higher cooling efficiency. A dense arrangement of holes is the basic idea of effusion cooling. The diameter is reduced compared to film cooling holes. With a distribution of drilled holes the level of cooling within the effusion holes rises due to an increased surface area, which is accompanied by additional convective cooling. This reduces the wall temperature and allows more efficient usage of the cooling mass flow. Looking only at cooling interests a transpiration cooled surface would be the optimum cooling technique. A coolant mass flow through a porous material strongly reduces the wall temperature, due to the large surface area, which is applicable for convective heat transfer.

However a perforated surface could lead to lifetime problems. The notch effect causes higher mechanical stresses, which are induced by high thermal heat loads and the elevated pressure levels inside the combustion chamber. Another disadvantage of external cooling techniques is the problem of particles in the coolant air. Dirt particles could plug cooling holes, which leads to higher wall temperatures. At hot spots, where the wall temperature is already close to the temperature limit of the material, plugged film cooling or effusion holes could lead to a local overheating.

Internal heat transfer

In contrast to external cooling concepts, the main purpose of internal heat transfer techniques in combustor cooling channels is to achieve an enhanced heat transfer at the wall and to realize a low or moderate pressure loss at the same time. If accomplished, the wall temperature is limited to sustainable temperature levels, whereas the pressure losses in the combustor component are minimized. To enhance the heat transfer, either the surface area or the heat transfer coefficient must be increased. To accomplish this, the thermal boundary layer has to be minimized, which leads to sharp temperature gradients and results in higher heat transfer coefficients at the wall. This can be realized with several cooling techniques.

Enhanced convective cooling techniques are known to provide a disturbance of the boundary layer. To do so, geometrical features are attached to the surface, which lead to a regular separation and re-attachment of the near wall flow field. This is achieved by rib turbulators with ribs aligned perpendicular to the main flow direction. In addition, angled ribs, dimpled surfaces or surfaces with hemispheres induce vortices that provide an enhanced mixing of the coolant. With these techniques cooler air from the core flow is transported towards the hot channel wall.

Impingement cooling is a successful method to cool surfaces with a high heat load. In the area of the impinging jet, high heat transfer coefficients are realized. On the other hand, the enhanced heat transfer coefficient is accompanied by a rise in pressure losses. Therefore, the application of impingement cooling to cool a combustion chamber wall should be limited to locations with high local thermal loads.

Combined heat transfer techniques

The strengths and limitations of the presented cooling techniques suggest that a combination of them would lead to a superior combustor cooling design. Examples for combined heat transfer techniques are presented in Fig. 1.7. A grouping of impingement and convective cooling can be found in combustors of stationary gas turbines [6]. For additional cooling those locations at a wall that have a high heat load are also cooled with impinging jets.

Arrangements of external and internal cooling techniques are realized with the so-called double-wall concepts. Here, the combustion chamber wall accommodates an additional thin channel, in which convective cooling reduces the wall temperature. At the end of the thin channel the “used” air is ejected to form a film cooling layer. In technical applications this idea has been realized [37],[48].

1.4 Motivation and literature review

This investigation is focused on convective cooling techniques. The intent is to expand the data base of convective cooling techniques to conditions typically found on backside cooled combustion chamber walls, where the Reynolds-numbers Re_D varies up to 500,000 and the convective cooling features are usually placed on one channel wall only. To date, only a limited number of experiments and numerical simulations are found in literature providing detailed information on heat transfer enhancement and pressure losses of convective cooling techniques for cooling passages in combustors at these conditions.

Within this study, three different convective cooling techniques are investigated. These cooling features can be categorized as rib turbulators, dimpled surfaces and surfaces with hemispheres. A sketch of the backside cooled combustor wall with the applied cooling technique is presented in Fig. 1.8.

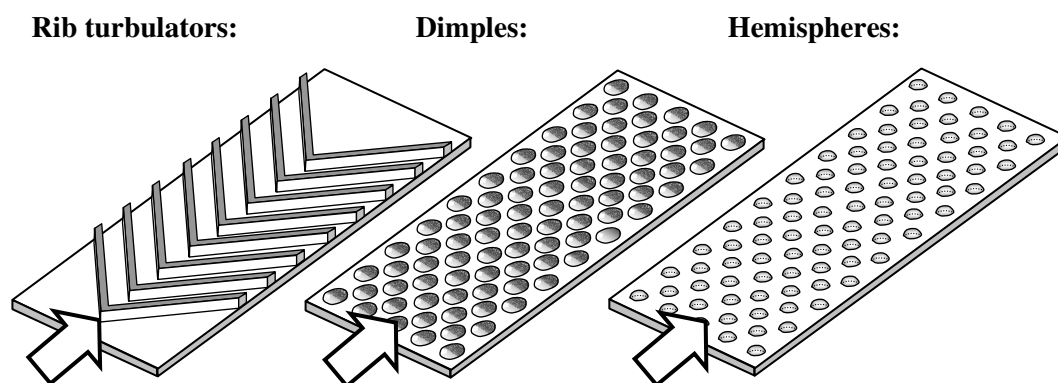


Fig. 1.8: Classification of investigated cooling techniques

Rib turbulators

Most investigations on rib turbulators applied in internal cooling channels arise from the experience of internal cooling in cooling passages of turbine blades and nozzle guide vanes. Early studies used cooling channels equipped with ribs, which are aligned perpendicular to the main flow direction. Further investigations suggested an implementation of angled ribs.

Han et al. [23] and Çakan [11] published an overview of multiple investigations on rib turbulators and provided detailed data of heat transfer enhancement and pressure losses. The influence on the variation of the dimensionless rib pitch-to-height P/e , the rib angle and the dimensionless rib height e/D_h on the heat transfer enhancement and the pressure loss have been reported. Han et al. [23] also presented a correlation for the heat transfer enhancement and the friction factor enhancement. The so-called R- and G-functions provide data for Reynolds numbers from 10,000 to 60,000 and rib pitch-to-height ratios of 10 and 20. The dimensionless rib height e/D_h is varied between 0.021 and 0.078 and the channel aspect ratio changed from $AR = 1:1$ to $AR = 4:1$. The ribs were placed on two opposite channel walls and the rib angle α between main flow direction and rib varied from 30° to 60° .

The authors concluded that reducing the dimensionless rib height e/D_h is lowering the heat transfer enhancement and the pressure losses. An optimum rib pitch-to-height P/e was found to be between 7 and 13. A rib pitch-to-height $P/e < 7$ has the negative effect of enclosing a vortex between two successive ribs, which prohibits a mass transfer from the core flow towards the channel wall and vice versa. Increasing the rib pitch-to-height above $P/e > 13$ allows the thermal boundary layer to grow and therefore, the temperature gradient at the channel wall is reduced. For 90° ribs no secondary flow features were detected. The inclination of ribs induces longitudinal vortices filling out the complete channel cross section. The vortices enhance the mixture between core flow and fluid close to the surface. A definition of the important rib parameters and an overview over the reported flow phenomena are presented in Fig. 1.9.

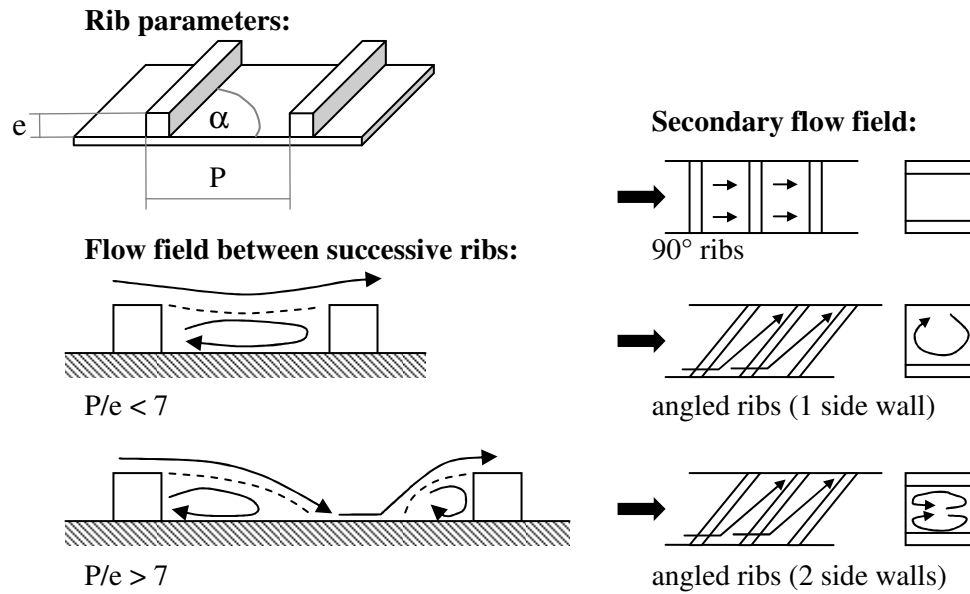


Fig. 1.9: Rib parameters and flow field in ribbed channels

In further progress, other rib geometries were introduced. Straight ribs were replaced by V-shaped ribs and later W-shaped ribs. Several investigations have been conducted regarding V-shaped and W-shaped ribbed cooling passages. An overview over the studies and the investigated parameter variations is presented in Table 1.1. It has been reported that replacing straight ribs with V-shaped ribs increases the heat transfer enhancement and the pressure losses, but the efficiency is superior to straight ribs.

Table 1.1: Investigations on V-shaped and W-shaped ribs

Reference	Configuration	Aspect Ratio	e/D_h	P/e	α	Re_D	Type
[35]	V-shaped two sided	1:1	0.0625	10/20	45° 60°	10,000 - 60,000	Exp.
[20]	V-shaped two sided	8:1	0.06	10	60°	1,000 - 6,000	Exp.
[38]	V-shaped two-sided	4:1	0.078	10	45°	5,000 - 40,000	Exp.
[25]	V-shaped two sided	1:1	0.0625	10	45°	15,000 - 90,000	Exp.
[57]	V-shaped two sided	1:1	0.0833	10	45°	5,000 - 30,000	Exp.
[2]	V-shaped two sided	2:1	0.094	10	45°	5,000 - 40,000	Exp.
[13]	V-shaped two sided	6.82:1 5:1 3:1	0.04 0.06 0.078	10	60°	10,000 - 30,000	Exp.

Reference	Configuration	Aspect Ratio	e/D_h	P/e	α	Re_D	Type
[59]	V-shaped W-shaped two sided	4:1	0.078	10	45°	10,000 - 40,000	Exp.
[56]	V-shaped two sided	4:1	0.078	10	45°	10,000 - 500,000	CFD
[43]	V-shaped one sided	10.15:1	0.02 0.022 0.028 0.034	10	30° 45° 60° 75°	2,500 - 18,000	Exp.

As seen from Table 1.1, no experimental data is found providing detailed information on a V-shaped and W-shaped rib configuration in cooling passages for conditions found in combustor liners.

Dimples

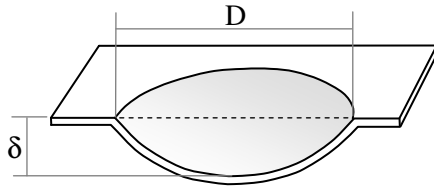
Khalatov [32] wrote a summary of the development of dimpled surfaces in the field of heat transfer augmentation. According to the author, dimples were first quoted in literature in 1976 and have originally been used to reduce the drag coefficient of golf balls. Dimples are known to disturb the laminar boundary layer and to create a turbulent boundary layer. The detachment of a turbulent boundary layer at a flow around a sphere is later in contrast to a laminar boundary layer. Therefore, the region of the detached flow behind a dimpled sphere is reduced compared to a smooth ball.

Early heat transfer and pressure loss measurements of dimpled surfaces have been conducted by Russian researchers and were first available after the breakup of the former Soviet Union. Nagoga [47] conducted substantial investigations on dimpled surfaces. The dimensionless dimple depth δ/D varied from 0.13 to 0.66 and the dimensionless channel height H/D was altered from 0.07 to 0.5. It was reported, that dimples on one channel surface with a dimensionless dimple depth of $\delta/D=0.5$ provide the highest heat transfer augmentation of around 300% compared to a smooth channel. But this heat transfer augmentation is also accompanied by the highest pressure losses. A significant reduction of the dimensionless channel height H/D lead to an increased heat transfer intensification.

In another investigation, Afanasyev et al. [1] reported detailed measurements on the thermal und hydrodynamic boundary layer above a dimpled surface. The dimensionless dimple depth was $\delta/D=0.067$ and the dimensionless channel height H/D varied from 10.67 to 17.78. They concluded that shallow dimples in relatively high channels have a negligible influence on the hydrodynamic boundary layer and do not noticeably increase the friction factor, whereas simultaneously a heat transfer augmentation of 30-40% was observed. Also Khalatov [32] used the dimensionless dimple depth δ/D to classify the spherical dimples in terms of the typical in-dimple flow pattern. He postulated that there are no separation zones inside a shallow dimple, whereas the vortex structure becomes

very complex for deep dimples as reported by Mahmood et al. [41]. A sketch of the simplified flow structure inside a dimple, the definition of dimple parameters and dimple patterns is presented in Fig. 1.10.

Dimple parameters:

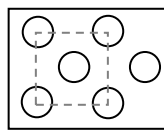


Simplified flow structure in a dimple:

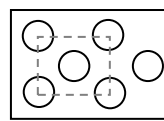


$\delta/D < 0.1$ (shallow dimple)

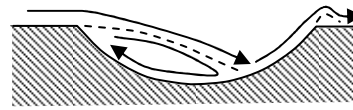
Dimple pattern:



square



rectangular



$\delta/D > 0.1$ (deep dimple)

Fig. 1.10: Dimple parameters and simplified flow structure in a dimple

In recent years, several studies have been conducted dealing with cooling passages equipped with one or two dimpled channel side walls. An overview of the investigated parameters is presented in Table 1.2.

In the literature, there are a few studies available considering the typical conditions found on a backside cooled combustor wall. To be in a position to assess the implementation of dimpled surfaces in combustor cooling passages, more investigations are necessary.

Table 1.2: Investigations on dimpled cooling channels

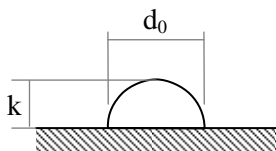
Reference	Configuration	Aspect Ratio	H/D	δ/D	Pattern	Re_D	Type
[15]	one sided	12:1	0.33	0.25	rectangular	15,000 - 35,000	Exp.
	two sided	4:1	1				
		2:1	2				
[39]	one sided	-	1	0.25	rectangular	23,000 - 46,000	CFD
	two sided		2				
[44]	one sided	16:1	0.37	0.19	rectangular	12,000 - 60,000	Exp.
		7.4:1	0.74				
		5.1:1	1.11				
		3.8:1	1.49				
[41]	one sided	8:1	0.5	0.2	square	19,000 - 115,000	Exp.
[9]	one sided	4:1	1	0.2	square	21,000 - 124,000	Exp.
				0.3			

Reference	Configuration	Aspect Ratio	H/D	δ/D	Pattern	Re_D	Type	
[8]	one sided	4:1	1	0.1	square	21,000 - 124,000	Exp.	
[22]	one sided	4:1	2	0.3	square	5,000 - 40,000	Exp.	
[60]	one sided	1:1	4.88	0.29	rectangular	7,000 - 21,000	Exp.	
[45]	one sided	1:1		0.134	rectangular	10,000 - 65,000	Exp.	
				2.65				0.167
				2.86				0.191
				3.31				0.204
				3.97				0.226
			0.250					
[33]	one sided	4.18:1	0.75	0.2	rectangular	120,000 - 380,000	Exp.	

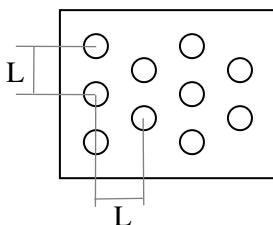
Hemispheres

The interest in surfaces, which are equipped with hemispheres, started in 1936. Schlichting [53] conducted experiments to obtain the friction factor of several roughened surfaces. Among other features, hemispheres were placed on a flat surface in a regular arrangement. Schlichting's purpose was to present an experimental approach to obtain an equivalent sand-grain roughness for any surface with a regular arrangement of roughness elements. Unfortunately, no heat transfer enhancements were investigated. Several years later, a correlation was reported by Sigal et al. [55], with which a calculation of the equivalent sand-grain roughness was possible.

Hemisphere parameters:



Hemisphere pattern:



Characteristic flow around a hemisphere:

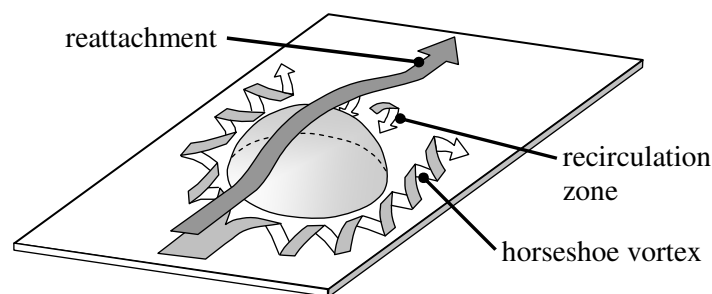


Fig. 1.11: Parameters and characteristic flow field of a hemisphere

Dipprey and Sabersky [17] provided an experimental investigation on the relation between heat transfer and friction of smooth and rough channels. The authors studied a smooth tube and three tubes with irregular roughened surfaces. One of the first

investigations on the heat transfer of regular roughened surfaces was reported by Hosni et al. [29]. They measured the heat transfer enhancement and the friction factor in a developing turbulent boundary layer for different roughness densities with L/d_0 from 2 to 10. The roughness height-to-hydraulic diameter k/D_h was 0.0038. For the highest roughness density investigated, a heat transfer augmentation of 75% was observed. A sketch to define the mentioned parameters and a sketch of the characteristic flow around a hemisphere is presented in Fig. 1.11.

To assess the effect of the geometry of the roughness element, the local heat transfer distribution of several features have been investigated by Chyu and Natarajan [14]. They placed a single cylinder, a cube, a diamond, a pyramid and a hemisphere respectively on a smooth surface. Typical areas of heat transfer enhancement were observed as a result of the characteristic flow conditions as presented in Fig. 1.11. The authors reported that in the stream wise direction a single hemisphere has a noticeable influence on the heat transfer augmentation of 2.5 hemisphere diameters d_0 . In transverse direction the region of heat transfer enhancement is reduced to around half a diameter d_0 on each side of the hemisphere. Compared to other geometries, hemispheres have a slightly smaller region, in which the heat transfer is enhanced.

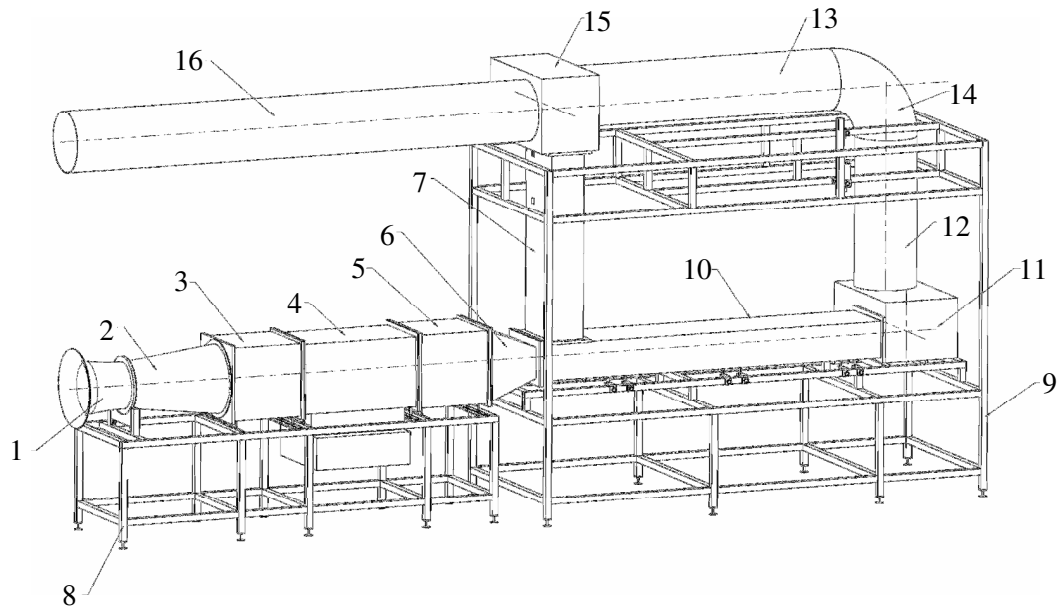
Moskvina et al. [46] reported heat transfer and friction data of surfaces equipped with two different hemispheric roughness elements. The roughness density L/d_0 varied from 8 to 8.5 and the roughness height-to-hydraulic diameter k/D_h was 0.043 and 0.0635. A heat transfer augmentation of 90% was detected and accompanied by a friction factor enhancement, which was two-times higher than the friction factor of a smooth surface. An overview of the mentioned studies and the investigated range of parameters is shown in Table 1.3.

Table 1.3: Investigations on cooling channels equipped with hemispheres

Reference	Configuration	Aspect Ratio	L/d_0	k/D_h	Pattern	Re_D	Type
[29]	developing boundary layer	5:1	2 4 10	0.0038	Rectangular	67,000 - 740,000	Exp.
[46]	one sided	-	8 8.5	0.043 0.0635	Rectangular	4,000 - 100,000	Exp.

2 Experimental setup

2.1. Test facility



1+2	Inlet nozzle	8+9	Supporting frame
3	Square cross section adapter	10	Test section
4	Heater (80kW)	11	Round cross section adapter
5	Passage with flow mixer and flow straightener	12+13	Transition
6	Converging nozzle	14	90° bend
7	Bypass	15	Adapter box
		16	Transition to blower

Fig. 2.1: Schematic sketch of the test facility

An open loop wind tunnel has been used for this study. A schematic of the test facility is shown in Fig. 2.1. In addition to the presented sketch, a blower, which operates in suction mode, is attached to the test facility. The blower produces pressure below ambient and thus provides the necessary air flow. The rate of air flow is adjusted by altering the rotational speed of the motor driving the blower, which can be varied from 500 to 1450 revolutions per minute. At maximum speed pressures below ambient of around 3000 Pa are feasible.

The air flow enters the test facility via the inlet nozzle, which is equipped with pressure taps at the tightest cross section. With the pressure readings, the mass flow entering the test facility can be calculated as given in (2.1). It is assumed that the test facility is gas-tight, so that the calculated mass flow enters completely the test section.

$$\dot{m} = A_{NOZ} c_f \sqrt{2(p_\infty - p_{NOZ}) \rho_{NOZ}} \quad (2.1)$$

After passing a square cross section adapter, the air flow enters a heater, which has an electrical heating power of 80 kW. The installed heater can provide air flow temperatures from 50°C and 90°C for mass flows between 1 and 3 kg/s. If an air flow with ambient conditions is desired, the heater is switched off. Behind the heater, the air flow passes a short passage. Within this segment a flow mixer is installed to homogenize the temperature field at the exit of the heater. At the end of this passage the flow is lead through a flow straightener to eliminate any possible large vortex structures. In the following nozzle the cross section is altered to fit the rectangular cross section of the test section. Once the air flow reaches the beginning of the test section, a valve selects whether the air flow is lead through the bypass, or it is directed through the test section. The valve is driven by a pneumatic cylinder allowing a fast switching mechanism.

At the end of the test section, which is described in detail in the following chapter, the air flow enters a small plenum. From here, the air flow is lead through a circular tube towards the blower. The bypass is also connected to this circular tube. The exit of the blower is 1.5m in front of the inlet nozzle. Before the air flow enters the blower a water-cooled heat exchanger removes the added heat and decreases the air temperature close to ambient conditions.

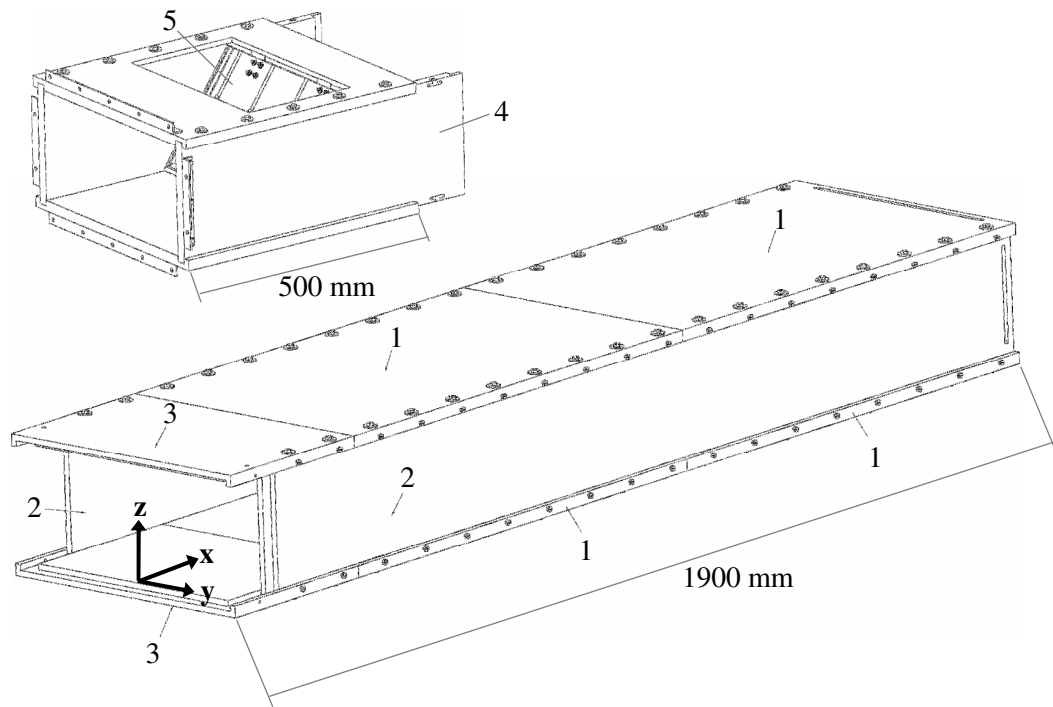
2.2. Test section

The test section has a total length of 2.4m with a constant rectangular cross section of 400x200 mm². Within the first 500mm the bypass adapter is located, which is made from wood. The rear part of the test section is 1900mm long and is made from Perspex. All Perspex plates have a thickness of 20mm. The advantages of using Perspex are the visual accessibility and a high thermal insulation due to its low thermal conductivity. The material properties of Perspex are given in Table 2.1 and a schematic of the test section and the bypass adapter is presented in Fig. 2.2.

Table 2.1: Material properties of Perspex

density	thermal conductivity	Heat capacity
1190 kg/m ³	0.19 W/(mK)	1470 J/(kgK)

A modular concept of the test section allows the re-movement of single bottom planes, without having to dismantle the whole test section. This provides high accessibility to the inner side of the passage. All wall features, which have been implemented on the bottom wall, are also made from Perspex to guarantee equal material properties as the test section walls.



- | | | | |
|---|---|---|----------------|
| 1 | Bottom plate (800x464 mm ²) | 4 | Bypass adapter |
| 2 | Side plate (1810x220 mm ²) | 5 | Valve |
| 3 | Bottom plate (300x464 mm ²) | | |

Fig. 2.2: Test section with separate bypass adapter

For realizing an alternative channel height H and thus a different aspect ratio two successive bottom plates can be replaced by special modules, which are presented in Fig. 2.3. Using different spacers within the modules, additional channel heights H' of 25, 50 and 100 mm are feasible. The total length of the test section with a reduced cross section is 1.6 m.

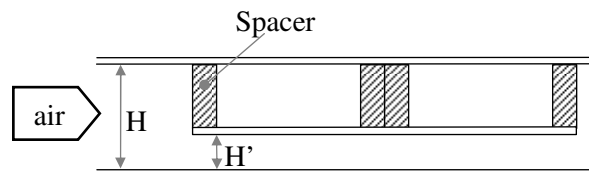


Fig. 2.3: Channel with implemented modules

A characteristic number to categorize the nature of the air flow is the Reynolds number Re_D . It is defined by the mass flow \dot{m} , the hydraulic diameter D_h , the cross section of the test section A_{MEAS} and the dynamic viscosity of air μ_{MEAS} at the measurement location as presented in equation (2.2). For the design a Reynolds number range of $90,000 < Re_D < 500,000$ was desired. This is achieved for the higher channel heights, whereas for reduced channel heights the topmost Reynolds numbers could not be realized due to the significant increase of the overall pressure losses.

$$\text{Re}_D = \frac{\dot{m}D_h}{\mu_{MEAS} A_{MEAS}} \quad (2.2)$$

The channel dimensions have been selected to realize a similarity of the Reynolds number and the Mach number between real geometry and experiment. Therefore, the typical scaling factors vary from 5 up to 10 for conditions found in backside cooled combustion chambers, which leads to an enlarged geometry within the experimental investigation. The enlargement is accompanied by two major benefits. The velocity range within the experiments stays at test conditions below 0.3 times the speed of sound, which is similar to the engine. For this reason, the air flow can be treated as incompressible and, therefore, the experimental and numerical complexity is simplified. An increased spatial resolution provides a more detailed view on the local heat transfer situation in between successive heat transfer augmentation features.

2.3. Pressure loss measurements

To obtain the pressure loss, pressure taps at several positions at the test section side wall have been installed in the direction of the x-coordinate (see Fig. 2.2 for the definition of the co-ordinate system). At these locations static pressures are measured. The static pressure is decreasing along the x-coordinate of the test section. In theory, the resulting pressure gradient along the x-coordinate is linear, if periodicity in the air flow is realized. This is achieved by aligning successive periodic segments of convective cooling features. It has to be ensured, that a sufficient number of convective cooling features is situated on the channel wall before the static pressure readings are taken into account. There are different studies addressing the periodicity depending on the used criteria. Han et al. [24] showed that six rib pairs were required based on his heat transfer results. Graham et al. [21] reported that 10 ribs based on the flow field and 4 ribs based on the static pressure were needed for fully developed conditions.

For the static pressure measurements the pressure taps are linked to a SCANIVALVE digital sensor module and an integrated A/D converter, which allows high frequency data acquisition. The digital sensor module consist of sub-modules from the type DSA3016, which are each able to accommodate a total of 16 pressure tap pipes. Within this study, two different sub-modules have been used, which have a measurement range up to 25 mbar and 69 mbar respectively. A total of 60 successive measurements have been conducted for a single measurement point, whereas each measurement point consists of a mean average of 32 readings.

The static pressure readings with their individual x-coordinate are then used to form a regression line for the pressure losses. With the gradient of the regression line the friction factor f can be calculated as presented in (2.3).

$$f = \frac{(\Delta p / \Delta x) D_h}{2 \rho_{MEAS} u_{AVG}^2} \quad (2.3)$$

The friction factors presented in this study are normalized by the friction factor of a smooth wall f_0 . For the smooth channel a correlation ($10^4 < Re_D < 10^6$) proposed by Blasius is used and the evolving friction factor ratio f/f_0 is presented in (2.4).

$$\frac{f}{f_0} = \frac{f}{0.046 Re_D^{-0.2}} \quad (2.4)$$

The application of the Blasius equation to normalize the friction factor values has been verified. Therefore, experimental data of the friction factor in the smooth test section is presented in Fig. 2.4 together with the values from the Blasius equation. Above a Reynolds number of $Re_D > 200,000$, the measured values are slightly higher than the results of the Blasius equation, whereas the trend for an increasing Reynolds number is well captured. The resulting friction factor ratios vary between 0.74 and 1.3, resulting in an overall adequate agreement. To complete, it has to be mentioned, that the measurements proved to be very sensitive due to the relative low pressure differences in the smooth channel especially at the lower Reynolds numbers.

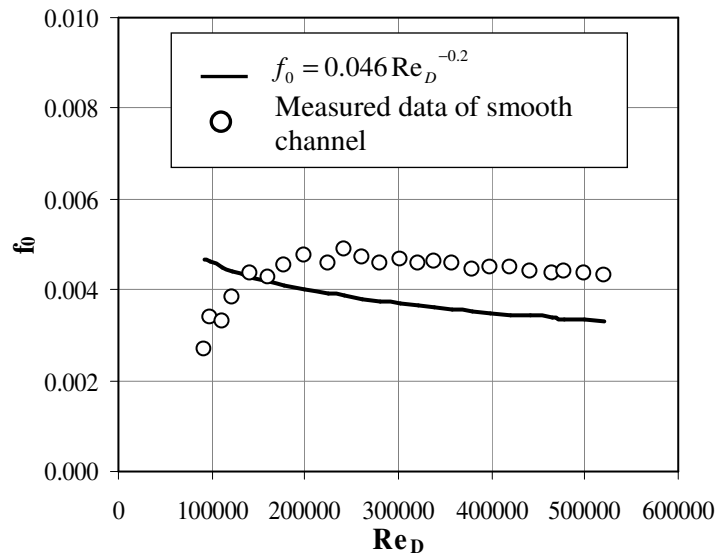


Fig. 2.4: Comparison between Blasius equation and measured data

An example of the implemented pressure taps and their location at the channel side wall is given in Fig. 2.5. Here, a total of 14 pressure taps are installed on the mid-plane of the smooth channel sidewall. For other channel heights for instance the positions of the pressure taps had to be adjusted to be located on the mid-plane respectively. This lead to a various number of different pressure tap locations. The detailed locations of the pressure taps are presented as the corresponding result of the pressure loss measurements.

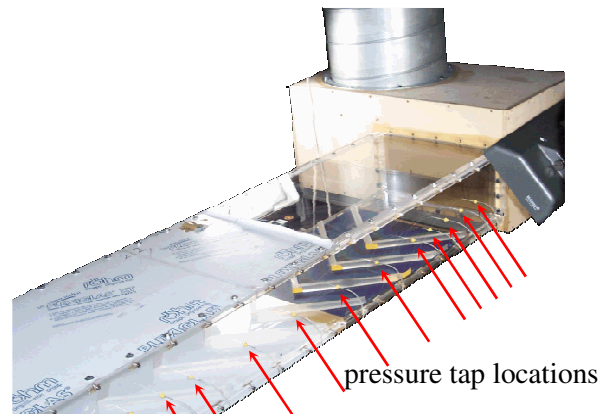


Fig. 2.5: Example of pressure tap locations at rear part of test section

2.4. Thermochromic liquid crystals (TLC)

Thermochromic liquid crystals are widely used in experiments to determine spatially resolved information on surface temperatures. Ireland and Jones [30] summarized the history of using TLCs within experimental setups and presented an overview on how TLCs can be used as temperature sensing layers on surfaces. A short summary of the nature of the TLC material is presented in the following passage.

A useful feature of TLCs is that within a certain temperature range a change in color throughout the visible light spectrum (400-800 nm) is observable, which is due to the change from solid phase (nematic structure) to liquid phase of the TLC material. In the solid and liquid phase the TLCs are optical inactive. Only in-between, when the TLCs are in a transition phase (cholestric structure), a certain temperature-dependent wavelength is reflected. It is possible to realize a sharp temperature-wavelength behavior, so that the change of color occurs within one or two degrees. Also a broader temperature-wavelength behavior is possible having a change of color within 20 degrees.

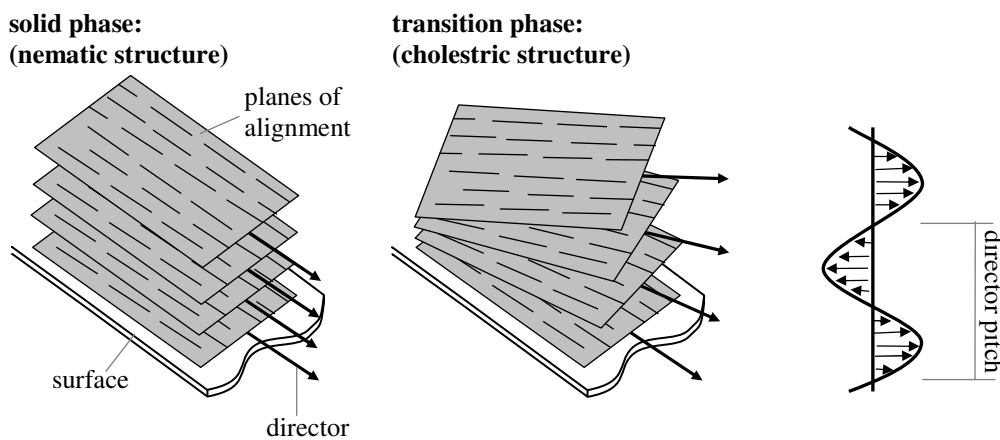


Fig. 2.6: Schematic of TLC behavior at solid and transition phase (taken from [30])

Within the solid phase the bar-like molecules show a so-called nematic structure. The spatial distribution and the orientation of the bar-like molecules is fixed and aligned, resulting in an anisotropic behavior of the TLC material. The vector of orientation of the bar-like molecules is the so-called director. If the temperature is rising, the spatial distribution breaks down, however the orientation of the molecules is still aligned. TLCs used for heat transfer experiments have a special feature. The orientation of the molecules is equal within a layer but changes slightly from one to another layer. This structure is called cholestric structure. The reason is that the molecules are skewed, which leads to the observed arrangement of planes with different orientations. A sketch to clarify the situation is presented in Fig. 2.6. The director rotation of the TLC layers has a helix-like structure. Within the transition phase of the TLC material, its director pitch is temperature dependent having a decreasing director pitch for an increasing temperature. Due to this behavior, visible light is reflected for a given TLC temperature range within the transition phase. Triggered by the temperature of the TLCs, the director pitch is changing and the wavelength of the reflected light is shifting. Passing the whole transition phase, the complete spectrum of light is successively visible on the surface covered with TLCs. If the temperature rises above the melting point, the liquid phase is reached. The alignment of the molecules is completely lost and the TLC material is reacting isotropically.

The basic idea of using TLCs in the steady and transient measurement technique is to know the local temperature gradient between air flow and surface. The air flow temperature is measured with thermocouples, the value of the surface temperature is provided with TLCs. To be in a position to use TLCs for a temperature sensing on surfaces the exact relation between reflected wavelength and surface temperature has to be identified. Therefore, TLCs are calibrated before they are applied in an experiment. The TLC calibration unit used is presented in Fig. 2.7.



Fig. 2.7: TLC calibration unit

A block of copper is coated with black paint to increase the contrast of the TLCs. On top of the black paint a layer of TLCs is sprayed. The copper block is fabricated to accommodate water cooling at one end and an electric heater on the other end. After

reaching a steady state a nearly linear temperature gradient is realized within the copper block. The video system acquires an image of the TLC color distribution and the temperature recorder obtains the temperature readings from a total of eight thermocouples, which are located along the copper sidewall. A detailed sketch of the instrumented copper plate is presented in Fig. 2.8.

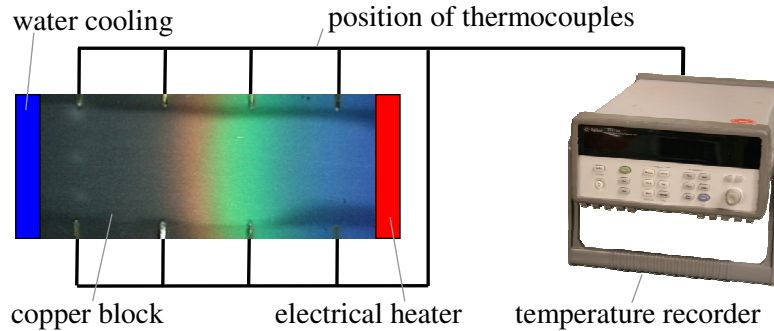


Fig. 2.8: Detailed sketch of copper plate used for TLC calibration

The color information is analyzed in the HSL and RGB color space. A typical HSL calibration is presented in Fig. 2.9a. The HSL color space is usually used for stationary experiments. Here, an H-range between $100 < H < 130$ is considered to obtain the desired surface temperatures. Within this H-range the temperature dependency of the H-values has a nearly linear character.

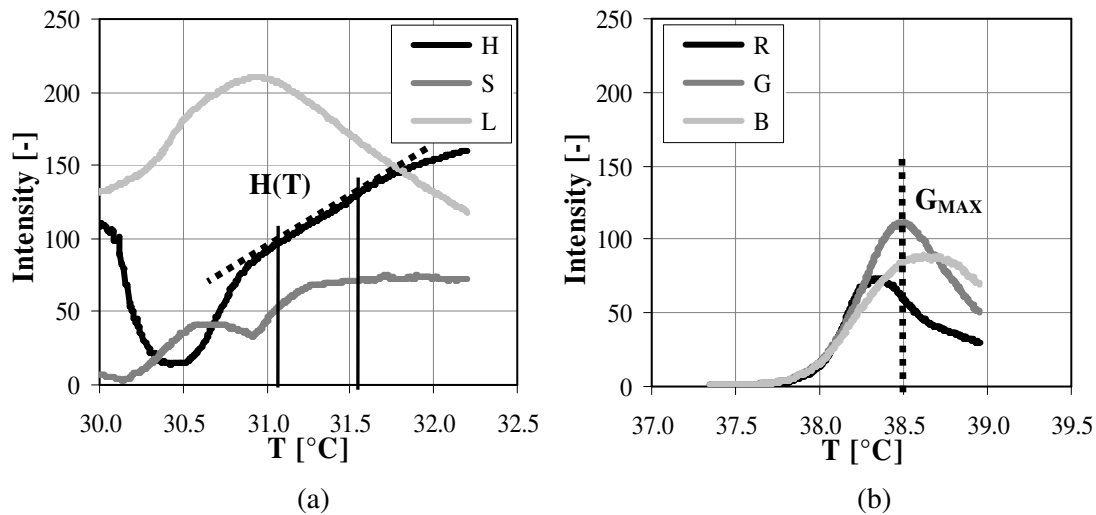


Fig. 2.9: (a) HSL calibration of TLC type BM/R31C1W/C17-10 with linear $H(T)$ approximation and (b) RGB calibration of TLC type BM/R38C1W/C17-10 with location of G-maximum

For the transient measurement technique a so-called maximum intensity method is used. Looking at Fig. 2.9b a global maximum of the R-, G- and B-values can be recognized respectively. For an observed point of time in an experiment, when the maximum intensity of the G-value is reached, a defined temperature can be associated. A more

detailed explanation of the different measurement techniques together with their advantages and disadvantages is found in a following chapter.

2.5. Steady measurement technique

One possibility to measure heat transfer enhancement on a surfaces is the steady measurement technique [30]. With this method it is feasible to obtain detailed information of the local heat transfer situation.

The basis for this measurement technique is the definition of the heat transfer coefficient h at a wall with a constant heat flux boundary condition, which is presented in (2.5).

$$h = \frac{\dot{q}_{CON}}{T_{TLC} - T_B} \quad (2.5)$$

To be in a position to evaluate the heat transfer coefficient h , a constant heat flux boundary condition has to be realized. Therefore, thin metallic heater foils ($\sim 25\mu\text{m}$) are attached on the rear part of the test section. A picture of the installed heater foils is shown in Fig. 2.10a. The surface contact of the heater foils is obtained by gluing them on top of a very thin adhesive layer ($\sim 25\mu\text{m}$). On top of the heater foils first a layer of black paint is added, which provides a high visual contrast for the later pictures from the color change of the TLCs, which are finally added on top of the black paint. The small thickness of the all layers is necessary to be able to neglect temperature gradients within these layers. Therefore, the real surface temperature can be assumed to be equal to the surface temperature of the Perspex plates. A sketch of the layer configuration is offered in Fig. 2.10b.

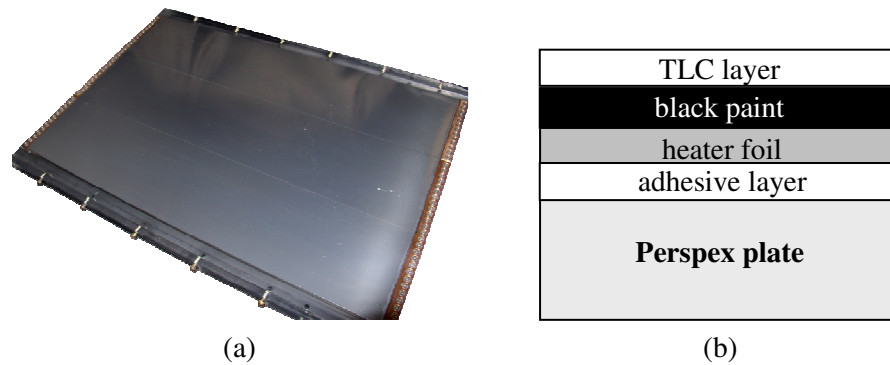


Fig. 2.10: (a) Perspex plate with mounted heater foil and (b) layer setup

To provide a constant heating of the covered surface, a total of three metallic lanes are connected in series to a DC power supply. The electric power P_{FOIL} released in the heater foils is obtained by measuring the resistance of the heater foils R_{EL} and the voltage potential U_{EL} across the heater foils. The equation is given in (2.6). Due to

conductivity and radiation losses the electric power has to be corrected to obtain the convective heat flux, as presented in equation (2.7).

$$P_{FOIL} = U_{EL}^2 / R_{EL} \quad (2.6)$$

$$\dot{q}_{CON} = P_{FOIL} / A_{FOIL} - \dot{q}_{RLOSS} - \dot{q}_{CLOSS} \quad (2.7)$$

The radiation losses are obtained by the Stefan-Boltzmann law, as given in equation (2.8). The emissivity of the black channel wall is considered to be close to unity ($\epsilon = 0.95$), which is valid for most non-metallic materials. Especially for surfaces covered with black paint, this assumption is justified.

$$\dot{q}_{RLOSS} = \epsilon \sigma A_{FOIL} (T_{TLC}^4 - T_B^4) \quad (2.8)$$

For the estimation of the conductivity losses through the Plexiglas plate, a 1D heat transmission model is applied. The unknown heat transfer coefficient on the backside of the test channel is estimated using a correlation for natural convection. As the surrounding temperature is known, the heat conduction losses can be iteratively calculated.

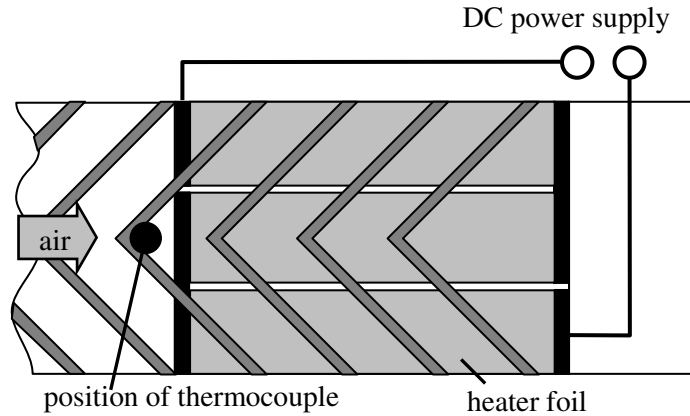


Fig. 2.11: Sketch of bottom surface rear part of the test section (taken from [42])

The mass flow bulk temperature T_B is measured by a K-type thermocouple. The wall temperature is given by the temperature indication of the Thermochromic liquid crystals T_{TLC} . The position of the thermocouple and the electric configuration is presented in Fig. 2.11.

For the steady measurement technique it is necessary, that the experiment is in thermal equilibrium, before measurements are taken. Therefore, the experiment is started beforehand and kept running for a certain period of time. This period is in the range of 20 to 30 minutes to assure nearly steady conditions.

As presented in Fig. 2.12 only a small area of the TLC-coated surface shows a change in color for a certain electrical power setting. To obtain full-coverage of the area between two successive ribs, the electric power has to be varied. Starting from relatively

high electrical power levels, the TLC change of color indicates a high heat transfer coefficient. As the electric power is reduced successively, the location of green color moves from the lower to the upper end of the respective pictures. The electric power is reduced until the lowest heat transfer coefficients have been identified and the TLCs are optically inactive. For each Reynolds number at least 15 different power settings have to be investigated.

The LABVIEW program DIPS [58] is used to process the single pictures of each power setting. Here, the H-values in the desired range, where beforehand a linear temperature-H-value relation (Fig. 2.9a) has been observed during the TLC calibration, are isolated and stored in a file separately. Another LABVIEW program translates the H-values into heat transfer coefficient data and combines the single files to one data file.

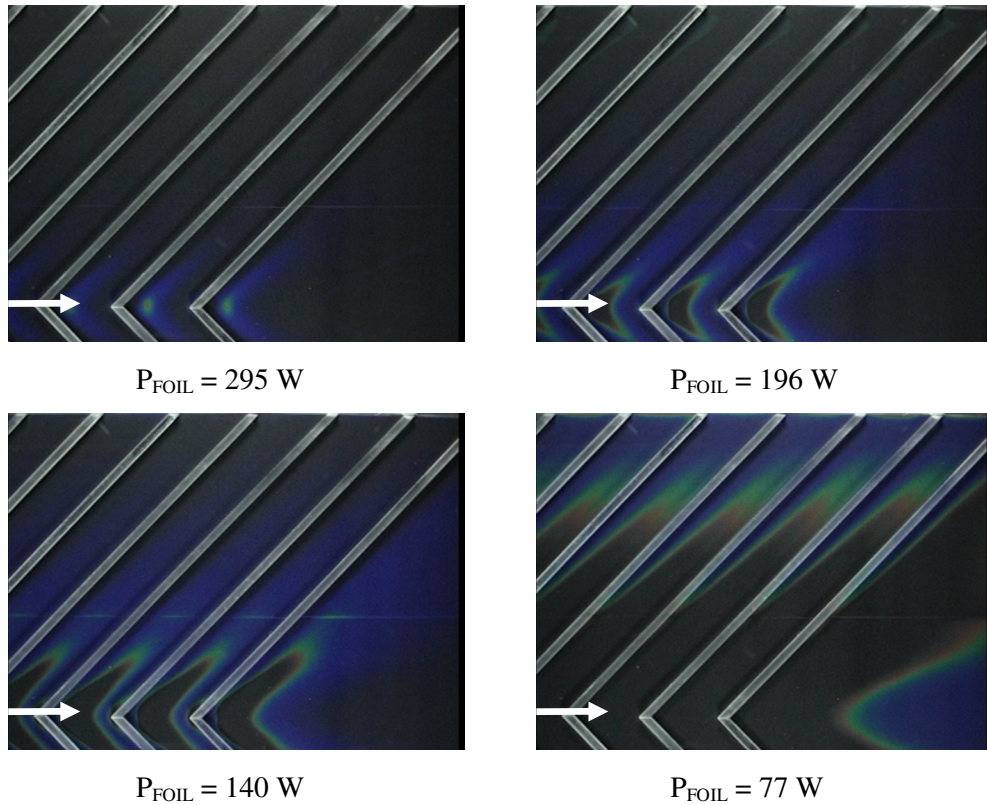


Fig. 2.12: TLC color response for different electrical power levels at $Re_D = 130,000$

For the data reduction all heat transfer coefficients are transferred into non dimensional Nusselt numbers and the results are normalized by the Nusselt numbers for a fully developed turbulent flow in a smooth channel. Here, the so-called Dittus-Boelter correlation as presented in (2.9) is applied.

$$\frac{Nu}{Nu_0} = \frac{Nu}{0.023 Re_D^{0.8} Pr^{0.4}} \quad (2.9)$$

The advantage of this measurement technique is the relatively low effort to evaluate heat transfer coefficient data out of the experiment due to the absence of numerical solving schemes. Unfavorable is the long total measurement time to obtain the experimental results of one Reynolds number and the difficulties during the application of the heater foil onto the channel surface.

2.6. Transient measurement technique

Unlike the steady measurement method, where a constant heat flux boundary condition is simulated, the transient measurement technique [30], [18] is based on the one-dimensional solution of Fourier's equation with a semi-infinite wall and a convective boundary condition.

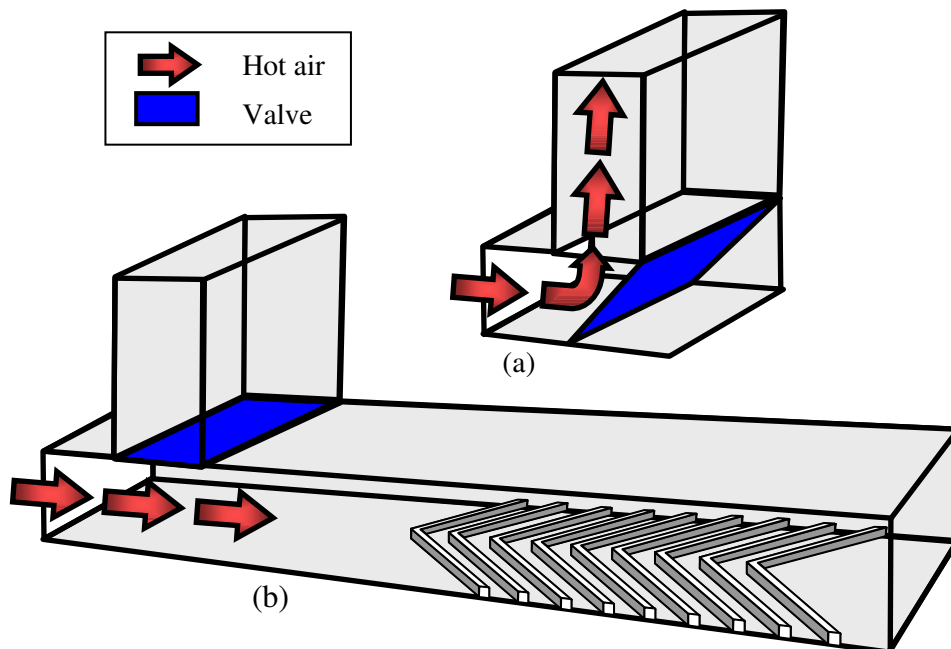


Fig. 2.13: Schematic of air flow in test section with (a) closed valve and (b) opened valve

To be applied a sudden change in the channel flow's temperature is needed, which initiates a heat flux into the channel wall. This sudden change in temperature is realized by the bypass system. As described before, a valve is installed in the front part of the test section. The valve system is pneumatically driven by a pressure reservoir of 6 bars to ensure rapid switching times of the valve of around 0.5 seconds. At the beginning of a transient experiment, the valve is closed and the air flow circulates through the bypass leaving the rear part of the test section unaffected. The air heater is switched on and the air flow is heated up to the desired level. Once the temperature in the bypass is steady the valve is opened and an air flow with a defined temperature step enters the rear part of the test section. A sketch of the air flow situation is presented in Fig. 2.13. From this time point a temperature gradient develops into the surface material and the surface temperature of the inner channel wall is rising.

On the locations, where the surface temperature is high enough, the TLCs start to change their color. Hence, in one single experiment a continuously TLC color response can be observed and recorded by a VCR system. The camera is aligned in a way that one half of the bottom wall and at least two successive periodic units of convective cooling devices are captured. A sketch of the rear part of the test section with the installed measurement devices is given in Fig. 2.14.

The opening of the valve is indicated by an LED, which is situated on the top wall of the test section as seen from Fig. 2.14. This device is used to synchronize the valve opening, which defines the starting time of the transient experiment, and the starting time for the evaluation of the video. The time dependent flow temperature readings are obtained by two K-type thermocouples, which are located on the mid-plane between top and bottom wall of the test section. The temperature level is read out every 0.3 seconds and the data thus obtained is stored in a data acquisition unit. To acquire the corresponding Reynolds number, the static pressure measurements at the inlet nozzle are conducted in the meantime of the transient experiment to ensure equal air properties. Further temperature readings of the bulk temperature of the air flow in the inlet nozzle and the higher temperature level in the test section are considered.

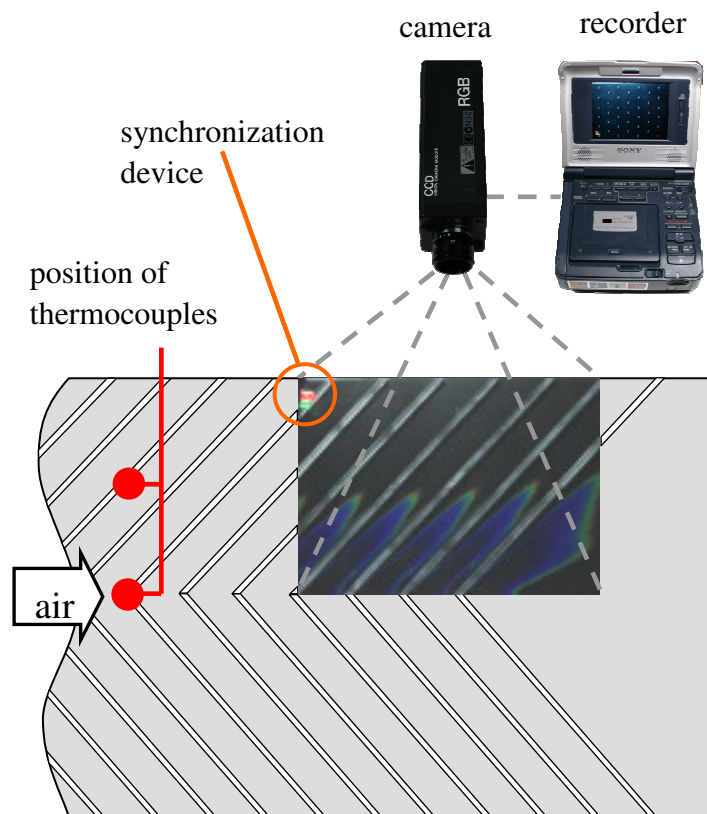


Fig. 2.14: Bottom rear part of test section with installed measurement devices for transient measurement method

Due to the semi-infinite assumption the experiment has to be finished before the temperature response reaches the outer surface of the channel wall. For this test setup the duration of an experiment varied typically between 50 seconds and 2 minutes.

Flat surfaces

The ITLR software package PROTEIN [50] is used to process the obtained videos and to evaluate the local distribution of the heat transfer coefficients. Therefore, the solution of the 1D heat conduction equation for semi-infinite solids is used, which is presented in (2.10). This equation can only be used if the temperature step in the channel is ideal, which is difficult to realize in most experiments.

$$\frac{T_W - T_0}{T_B - T_0} = 1 - e^{\beta^2} \operatorname{erfc}(\beta)$$

$$\text{with } \beta = h \sqrt{\frac{t}{\rho_W c_{p,W} k_W}}$$
(2.10)

To account for the real temperature step, the Duhamel principle is employed as presented in (2.11). As equation (2.10), it can not be solved explicitly. To calculate the heat transfer coefficient, numerical solution schemes have to be applied.

$$T_W - T_0 = \sum_{j=1}^N \left[1 - e^{\beta^{*2}} \operatorname{erfc}(\beta^*) \right] \cdot \Delta T_{B(j,j-1)}$$

$$\text{with } \beta^* = h \sqrt{\frac{t - \tau_j}{\rho_W c_{p,W} k_W}}$$
(2.11)

Surfaces with curvature

In contrast to the evaluation of the heat transfer coefficients on flat surfaces as described above, equation (2.11) can not be directly applied to obtain data on surfaces with curvature. In this study, dimpled surfaces and channel walls covered with hemispheres are investigated.

Buttsworth and Jones [10] presented an approximate solution of the 1D heat conduction equation, which accounts for surface curvature, as given in (2.12). In their equation, the minus sign is used for convex surfaces, the plus sign is applied for concave surfaces, $\xi = 1$ for a cylinder and $\xi = 2$ for a sphere. For an infinite radius R , equation (2.12) would reduce to equation (2.11).

$$\frac{T_W - T_0}{T_B - T_0} = \frac{1}{1 \pm \frac{\xi k_W}{2h_{CURV} R}} \left[1 - e^{\chi^2} \operatorname{erfc}(\chi) \right]$$

$$\text{with } \chi = \left(h_{CURV} \pm \frac{\xi k_W}{2R} \right) \sqrt{\frac{t}{\rho_W c_{p,W} k_W}}$$
(2.12)

Kotulla et al. [34] investigated the effect of surface curvature and finite wall thickness for a cylinder. They evaluated heat transfer coefficients on surfaces with curvature with equation (2.10) and equation (2.12) and reported that using equation (2.10) for surfaces with curvature can lead to errors up to 10 % depending on the experimental conditions. As done for the evaluation of heat transfer coefficients on flat surfaces, the actual temperature step is accounted for by using the Duhamel principle, which is given in (2.13).

$$T_w - T_0 = \sum_{j=1}^N \frac{1}{1 \pm \frac{\xi k_w}{2h_{CURV} R}} \left[1 - e^{\chi^2} \operatorname{erfc}(\chi^*) \right] \cdot \Delta T_{B(j,j-1)} \quad (2.13)$$

$$\text{with } \chi^* = \left(h_{CURV} \pm \frac{\xi k_w}{2R} \right) \sqrt{\frac{t - \tau_j}{\rho_w c_{p,w} k_w}}$$

Data reduction

To be able to compare the rate of heat transfer augmentation from different convective cooling features, Nusselt numbers are normalized with the corresponding Nusselt number of a fully turbulent flow in a smooth channel. Contrary to the steady measurement technique, for which it is difficult to obtain values of the heat transfer coefficient on the smooth channel wall for fully developed flow and thermal conditions, the transient measurement technique is capable of conducting appropriate heat transfer experiments on the smooth channel wall. The results of the experiments are plotted in Fig. 2.15, together with the so-called Dittus-Boelter correlation (2.9) and a correlation for isothermal walls presented by Kays et al. [31], which is shown in (2.14).

$$\frac{Nu}{Nu_0} = \frac{Nu}{0.021 \operatorname{Re}_D^{0.8} \operatorname{Pr}^{0.5}} \quad (2.14)$$

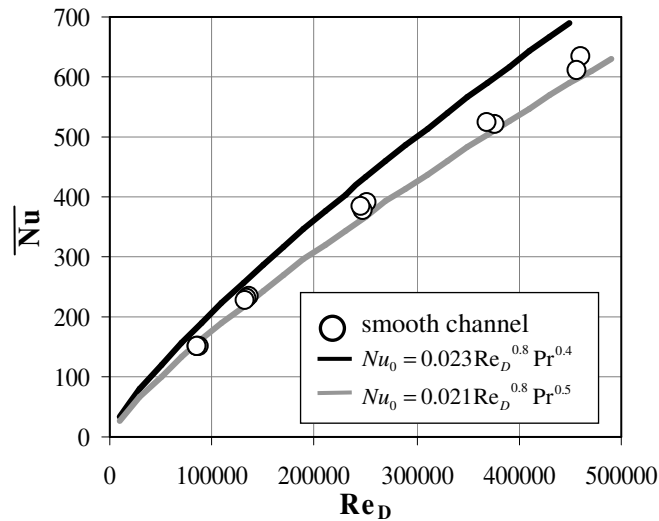


Fig. 2.15: Area averaged Nusselt number of smooth channel

As can be seen from Fig. 2.15, the experimental data fit well with the correlation provided by Kays et al. [31] and, therefore, this correlation is used to normalize all experimental results, which are obtained with the transient measurement technique.

In the case of dimpled surfaces or surfaces covered with hemispheres, the total surface area consists of a mixture of flat surfaces and surfaces with curvature. To compare the experimentally obtained heat transfer coefficients of dimpled surfaces with the results of ribbed channels, which are completely treated as semi-infinite flat solids, several steps have to be conducted. The heat transfer coefficients on the flat surface area are evaluated by using equation (2.11). For the dimples or the hemispheres themselves, equation (2.13) is used. A combination of the two data fields leads to the final local heat transfer distribution. To be able to calculate a representative area-averaged Nusselt number ratio, the effect of additional surface area on surfaces with curvature needs to be considered. Due to the larger surface area of surfaces with curvature, the obtained heat transfer coefficients are multiplied by an area enlargement factor. This factor is calculated by dividing the area of the surface with curvature with its projected flat surface. To provide an example, the evaluation process is illustrated in Fig. 2.16.

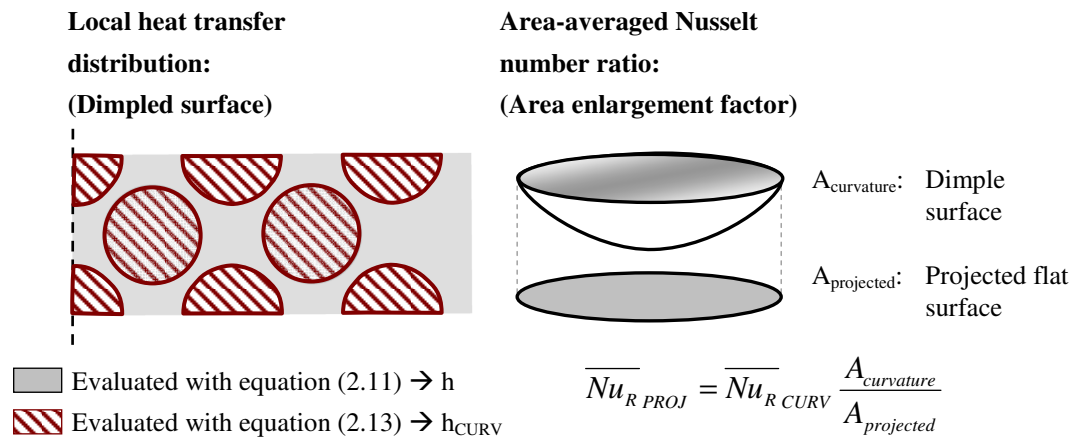


Fig. 2.16: Evaluation process of channel walls with flat surfaces and surfaces with curvature

The transient measurement technique offers the opportunity to conduct more experiments in a given period of time than would be possible with the steady measurement method. Otherwise, the effort to process the experimental raw data is intensified. The data reduction process for the transient measurement method is more complex compared to the steady measurement method and, therefore, more sensitive to measurement uncertainties (see Appendix B for error analysis) and application errors.

2.7. Lumped heat-capacitance method

With the above described steady and transient measurement technique, it is difficult to obtain heat transfer coefficients for the rib itself. For the steady measurement technique, it would have been challenging to cover the various ribbed elements with the thin heater

foil. Furthermore, it would have been unavoidable to create sharp kinks within a heater foil lane. This could cause an inhomogeneous heat flux distribution on the ribs. For the transient measurement method, the approach of assuming a semi-infinite solid and one-dimensional heat conduction is not valid. To gather information on the level of heat transfer on obstacles in a channel, Chen et al. [12] applied the so-called lumped heat-capacitance method. A brief description of this method is provided here.

Thermal model of the lumped heat-capacitance method

The thermal model of the heat-capacitance method is presented in Fig. 2.17. As for the transient measurement method, the rib is exposed to a sudden temperature change of the test channel air flow. It is important for the lumped heat-capacitance method, that the material, on which heat transfer coefficients are obtained, possesses a high thermal conductivity and therefore a much lower Biot number than the material it is placed on. Therefore, the rib itself consists of an aluminum alloy AlCuMgPb, which has a much higher thermal conductivity than Plexiglas. The heat capacity of the used aluminum alloy is presented in Table 2.2. The exact quantity of the thermal conductivity has not been measured, but considered to be similar to the thermal conductivity of pure aluminum.

Table 2.2: Material properties of AlCuMgPb

T_B	density	heat capacity
20°C	2834 kg/m ³	847 J/(kgK)
40°C	-	859 J/(kgK)
60°C	-	872 J/(kgK)

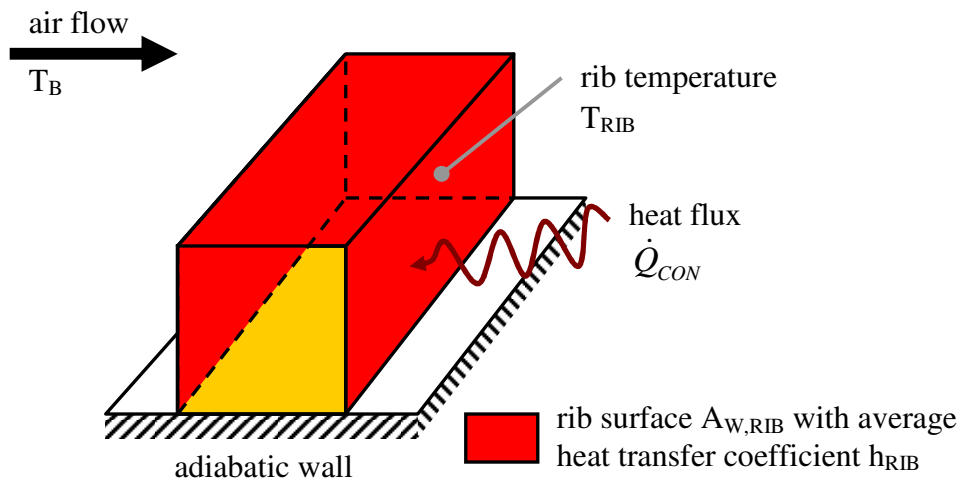


Fig. 2.17: Thermodynamic model of lumped heat-capacitance method

Having a low Biot number, it can be assumed, that there are no significant spatial temperature variations within the rib. Furthermore, the heat flux from the aluminum rib into the Plexiglas is neglected, due to the low thermal conductivity of the Plexiglas material. With these assumptions, the thermal problem can be described by equation (2.15). The driving temperature difference between air flow and rib initiates a heat flux into the rib through the rib surface with an average overall heat transfer coefficient and leads to a temperature rise of the aluminum rib.

$$\dot{Q}_{CON} = m_{RIB} c_{RIB} \frac{dT_{RIB}}{dt} = h_{RIB} A_{W,RIB} (T_B - T_{RIB})$$

with

$$T_{RIB} = T_0 \text{ at } t = 0$$
(2.15)

The solution to the above equation is equation (2.16).

$$\frac{T_{RIB} - T_0}{T_B - T_0} = 1 - e^{(\gamma)}$$

with $\gamma = \left(-\frac{h_{RIB} A_{W,RIB} t}{m_{RIB} c_{RIB}} \right)$

(2.16)

As for the solutions presented for the transient measurement method, the Duhamel principle, which accounts for a real temperature increase rather than an ideal temperature step, is considered as presented in equation (2.17).

$$T_{RIB} - T_0 = \sum_{j=1}^N [1 - e^{\gamma^*}] \cdot \Delta T_{B(j,j-1)}$$

with $\gamma^* = \left(-\frac{h_{RIB} A_{RIB} (t - \tau_j)}{m_{RIB} c_{RIB}} \right)$

(2.17)

As equation (2.17) is similar to equation (2.11) of the transient measurement method, the very same solver, provided by the ITLR software package PROTEIN, can be used to compute the average heat transfer coefficients.

Experimental setup of the lumped heat-capacitance method

The experimental setup of the lumped heat-capacitance method as presented in Fig. 2.18 is similar to the transient measurement method. In contrast to the transient measurement method, three successive Plexiglas ribs are replaced with aluminum ribs. This guarantees comparable conditions between the lumped heat-capacitance experiment and the corresponding experiment using the transient measurement method, which has been described before.

The aluminum ribs are covered with black paint and TLCs. Once the experiment is started and a distinct temperature is reached, the TLC color response on the rib surface is visible and captured by a video recording system.

In contrast to the transient and steady measurement method, it is not possible to obtain a local distribution of the heat transfer coefficients, if the rib is made of one piece. Due to the high thermal conductivity of the aluminum rib, the TLC color response on the aluminum rib is visible at nearly the same time for the whole rib segment as the rib surface reaches the temperature range of the TLC color response.

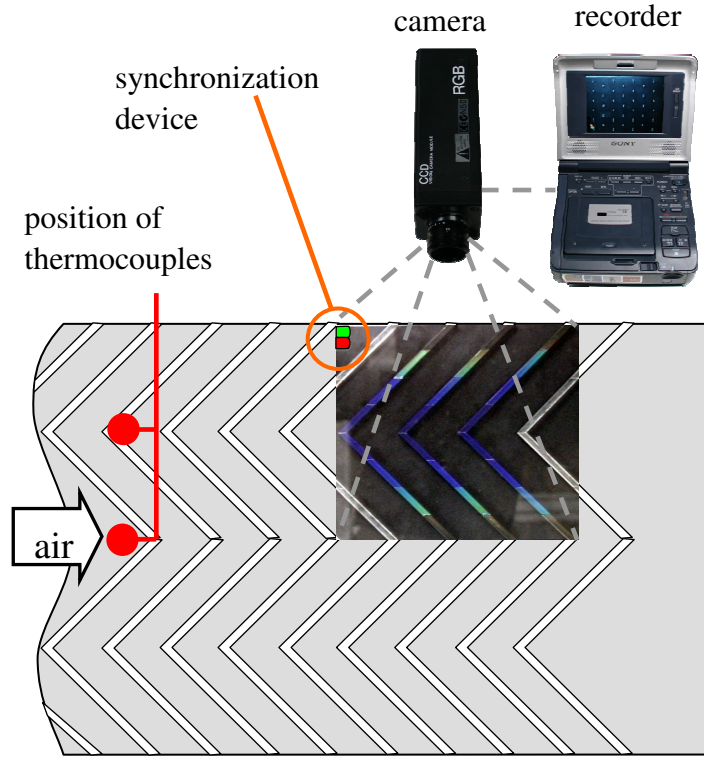


Fig. 2.18: Bottom rear part of test section with installed measurement devices for lumped heat-capacitance method

In this study, the aluminum rib consists of a total of eight pieces to provide a segment wise distribution of the average heat transfer coefficients on the rib surfaces. To prevent heat conduction from one rib segment to another, the segments are thermally isolated using a low conductive adhesive tape with a thickness of 30 μm . Due to the short duration of the experiment, which is normally finished within 45 seconds, the heat flux through this insulation layer is considered to be small.

To obtain a representative area-averaged Nusselt number of the roughened channel wall, the area-averaged Nusselt number on the smooth channel wall between two successive ribs and the area-averaged Nusselt number on the rib are combined as presented in equation (2.18).

$$\overline{Nu}_{R+RIB} = \frac{\overline{Nu}_{RIB} A_{W,RIB} + \overline{Nu}_R A_W}{A_{W,RIB} + A_W} \quad (2.18)$$

It has to be noted, that a representative area-averaged Nusselt number of the roughened channel wall could also be defined by dividing the numerator of equation (2.18) with the surface area of the corresponding smooth wall. According to this proposal, the area-averaged Nusselt number of test cases with a rip pitch-to-height of $P/e=10$ would be enhanced by an additional 20 %. For test cases with a rip pitch-to-height of $P/e=5$, the area-averaged Nusselt number would be increased by an additional 40 %.

3 Numerical setup

3.1 Purpose of computational fluid dynamics (CFD)

Most technical problems, which deal with fluid flows in channels or around bodies, are too complex to be solved analytically. In times, before numerical simulations could be conducted, scientists had only the chance to carry out experimental investigations, which as well have their limitations. For instance, conducting experiments over a large parameter range is costly, because it's always accompanied by the necessary sophisticated experimental setups.

With the development of computational fluid dynamics engineers have an instrument to check the influence of parameter variations before experiments are conducted. Such a preselection of interesting parameters aides to reduce the total experimental effort. To date, improvements in numerical simulations and growing computing power allow the use of CFD in a wide range of challenging fluid flow situations, such as combustion processes or multiphase flows.

In this study, the main scope of the numerical investigations is to simulate the main flow structures and to reveal the existence and the location of secondary flow features. Details on the flow field could have been also obtained by the usage of additional experimental methods as e.g. the particle image velocimetry (PIV) as described in the Appendix. With CFD an insightful view into the flow field is available without the need to conduct further experiments.

The knowledge of the flow situation is helpful and necessary to understand pressure loss and heat transfer behavior obtained from the experiment. A kind of "standard industrial" numerical setup as used in industrial design processes is applied to investigate the accuracy of such an approach to high Reynolds number flows for combustor liner cooling. Also, additional heat transfer data on the ribs themselves can be estimated from the numerical investigation.

3.2 Fundamentals of CFD

In principle, any simulation of a real flow phenomena aims to predict the velocity and temperature field. Knowing these distributions allows calculating all desired parameters such as heat transfer coefficient or friction factor. In internal fluid flows the velocity field is mainly determined by the channel geometry and the condition of the surface. The temperature field is primarily influenced by the fluid and wall temperatures and by the existence and the level of heat fluxes at the wall. In many cases the two distributions interact, so that the velocity and temperature field are not allowed to be treated separately. Strong velocity gradients or high viscosities lead to non-negligible amounts

of heat generation within the fluid flow due to friction. Spatial changes of fluid density induced by temperature gradients initiate a lifting force, which influences the velocity field.

This chapter does not aim to present a complete overview of the developments in the field of CFD. In fact, a short introduction into the basic ideas and the terminology is desired. For further information the author refers to standard literature (e.g. [4]).

The fundamentals of analytical and computational fluid dynamics are the conservation of mass and energy and the balance between the momentum within the fluid and the acting forces. These fundamentals have to be obeyed by any fluid flow and lead to a basic set of differential equations [31]: the equation of the conservation of mass, the momentum equations and the equation of the conservation of energy. The density is linking the momentum equation and the equation of the conservation of energy. This variable provides the earlier mentioned interaction between temperature and velocity field. For few circumstances or due to assuming so, the total differential of the fluid's density is set to zero, which means that the fluid can be treated as incompressible. In these cases the velocity and temperature field can be solved separately.

The so-called Navier-Stokes equations, which are generally used for CFD, are derived from the momentum equation. To do so, a declaration of the fluid stress tensor has to be made. For common fluids it is suitable to treat those fluids as Newtonian fluids.

3.3 CFD computations of turbulent flows

Turbulence is always three-dimensional and of unsteady nature. In this study the commercial CFD software FLUENTTM is used to perform the fully three-dimensional numerical calculations. In most technical applications dealing with internal fluid flows the flow is fully turbulent. This means that all fluid particles move in an unsteady and fluctuating manner within the flow. In internal channels a fluid flow is supposed to be turbulent, when the Reynolds number, based on the hydraulic diameter, is above the critical Reynolds number of $Re_{D, CRIT} \approx 2300$. A turbulent flow in general has a higher diffusion compared to a laminar flow, which leads to a higher heat transfer rate, but also to an increased friction factor. The flow character is totally different to a laminar flow, where the flow is oriented in layers, which are aligned parallel to the channel walls.

To be in a position to compute the Navier-Stokes equations, the grid employed has to be fine enough to resolve even the smallest spatial flow variations. Also the time resolution has to be fine enough to resolve fluctuations. This approach is called the direct numerical simulation (DNS). It manages to solve the Navier-Stokes equation without assumptions or simplifications but leads to a tremendous computational and numerical effort. To date, fluid flows with higher Reynolds numbers go beyond the scope of DNS due to the necessary sophisticated computational infrastructure.

An attempt to reduce the computational demand is accomplished by the usage of large eddy simulations (LES). The key of this technique is to resolve the larger eddies only,

since they primarily determine the flow character. Detailed information of smaller eddies and their effect on the larger eddies is obtained by models. Being in a position, where small eddies don't have to be calculated individually, the spatial resolution of the grid can be reduced. Still, the computational effort is high for flows with higher Reynolds numbers.

The software FLUENTTM is used to solve the Reynolds averaged Navier-Stokes equations (RANS). These equations are obtained by splitting each variable into an average part and a turbulent fluctuating part. The next step is to time average the equation. As a result of this averaging, all expressions, which consist of one fluctuating part only, become zero, because the temporal mean of the turbulent fluctuation around its mean is zero. Unfortunately, not all expressions with turbulent fluctuations vanish during the time averaging. There are still non-linear terms in the Reynolds averaged Navier-stokes equation, which can be interpreted as a turbulent shear stress and are normally referred to as Reynolds stresses. In principle, it means that fluids in a turbulent flow have different effective fluid properties than the same fluids in a laminar flow would have. Similar non-linear terms are generated, when the energy equation is time averaged.

There are several turbulence models available in literature, each having their advantages and disadvantages for a varying number of technical applications. To fulfill the scope of this study a "standard industrial" setup is used and analyzed for its accuracy. Therefore, two common turbulence models, both available in the CFD software FLUENTTM, have been used. For channels with implemented ribs a standard k- ϵ type turbulence model (sk ϵ) with enhanced wall treatment is applied. In the case of hemispheres and dimples a Reynolds stress model (RSM) is used.

The standard k- ϵ turbulence model

The standard k- ϵ turbulence model consists of two transport equations. One transport equation is used for the turbulent kinetic energy k and one for the turbulent kinetic dissipation rate ϵ . In the case of the turbulent kinetic energy k , an analytically exact equation can be derived. For the turbulent kinetic dissipation rate ϵ , this is not feasible. Its transport equation is modeled to be a mathematical equivalent compared with the transport equation of the kinetic energy k . Therefore, the standard k- ϵ turbulence model is called to be a semi-empirical model. More details on this turbulence model are available in [19].

The Reynolds stress model

The basic idea of the Reynolds stress model is to compute a transport equation for each Reynolds stress component of shear stress tensor individually. In the transport equation, terms for production, dissipation and diffusion define the level of the single Reynolds stresses. Unfortunately, the problem of solving the unknown non-linear Reynolds stress terms is not solved. New unknown non-linear triple correlations appear which need to

be modeled for a further application of the Reynolds stress turbulence model. In the literature, this problem is referred to as the closure problem. For a more detailed description of this turbulence model the author refers to [19].

Near-wall treatment in FLUENT™

For wall-bounded flows the effect of the wall on the turbulence is most significant. In general, the near-wall region is divided into three layers. Close to the wall, the wall damps the turbulent fluctuations. The molecular viscosity μ of the fluid is mainly determining the flow, which leads to nearly laminar behavior. This layer is called the viscous sublayer. Away from the wall, the turbulent fluctuations dominate the flow behavior. In this fully turbulent region the dimensionless velocity u^+ obeys the so-called logarithmic law of the wall. In between the two layers a blending region is found.

There are two ways to handle turbulence near a wall. One way is to use semi-empirical function, the so-called wall functions, instead of resolving the near wall region completely. One major advantage is that the mesh close to the wall has not to be refined. This leads to a reduction of computational time especially with high Reynolds number flows. For a flow situation with highly three dimensional character or with flow separation in the near-wall region, it is not recommended to use wall functions. Here, the turbulence model is constrained to resolve the turbulence levels down to the wall.

To do so, another approach is available in FLUENT™. To deal with turbulence in the near-wall region, the mesh close to the wall is refined. A slightly modified turbulence model with respect to the viscous sublayer and the blending region is then able to resolve the turbulence levels in the near-wall region. Depending on the turbulent Reynolds number Re_y , which is based on the local wall distance, the treatment of the turbulence is decided. For turbulent Reynolds numbers $Re_y > 200$ the $sk\varepsilon$ or the RSM models are in use. Is the turbulent Reynolds number $Re_y < 200$, further models are employed to resolve the viscous sublayer. This approach is called a two-layer approach. Additional information on the turbulence treatment in the near-wall region is provided in [19].

In this study the standard $k-\varepsilon$ turbulence model is used together with an enhanced wall treatment. With enhanced wall treatment both approaches are feasible. The solver itself decides, whether the wall functions or the two-layer approach is computed, depending on the available grid refinement in the near-wall region. Is the dimensionless wall distance y^+ below or around $y^+ \approx 1$, then the two-layer approach is used. Further information on this topic is available in [19].

3.4 Grid generation

To conduct a CFD computation, one of the first tasks is to create a CAD (Computer Aided Design) model of the real geometry. In this study, the more complex geometries (e.g. dimples and hemispheres) are designed with the commercial software

ProEngineer™, whereas the simpler geometries (e.g. ribbed channels) are setup directly in the supplied meshing software package. To be able to import the ProEngineer™ models in the meshing software, the CAD data is exported as *igs*-files, a common data transfer format. Once the geometry is imported into the meshing software, one major task is to check the geometry on fillets or translation errors. These inaccuracies could cause the CFD computation to not converge, or that the overall mesh quality is insufficient. In this study the commercial tools GAMBIT™ and ICEMCFD™ are used to generate the block-structured grids.

To reduce the need for computing power infrastructure and computational time, the complete channel geometry is reduced and only a periodic segment is considered for CFD computation. To be able to compare the CFD results with the experimental data, a nearly periodic flow has to be realized in the experiment. As far as possible, symmetry planes are used to reduce the computational domain even further. For channels with equally aligned turbulators on one channel wall only, this means that only half of the periodic segment is meshed and analyzed. In the case of channels with turbulators on two opposite channel walls, another symmetry plane is located and the computational domain is reduced to one quarter of the periodic segment. The final domain is then divided into blocks, which leads to a block-structured grid. In one last step the spatial distribution of the single blocks is decided and the mesh created. All grids used in this study meet the requirement of a dimensionless wall distance y^+ between wall and first grid layer being smaller than 1. A schematic of this sequence is presented in Fig. 3.1.

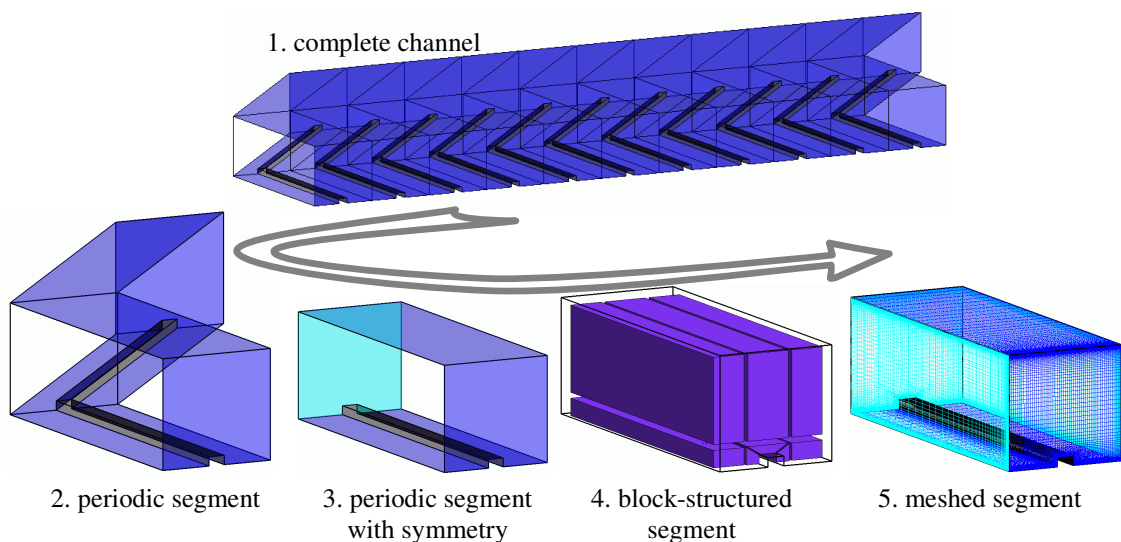


Fig. 3.1: Grid development

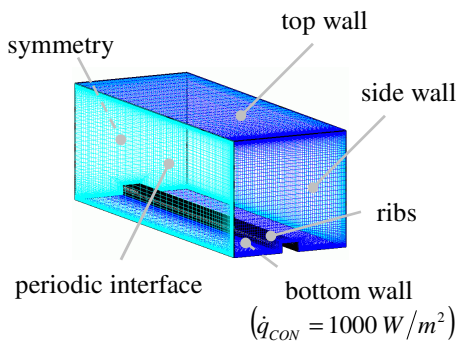
Once the grid is created and the grid quality is sufficient, the boundary conditions are defined. As mentioned in a previous chapter, two different measurement techniques are employed and therefore, two different sets of boundary conditions need to be used to match the respective heat flux situation. A summary of the employed boundary conditions is presented in Fig. 3.2.

For the steady measurement technique, constant heat flux boundary conditions are implemented. Here, the bottom wall is supplied with a constant heat flux of $\dot{q}_{CON} = 1000 \text{ W/m}^2$, whereas all other walls are treated as adiabatic walls. This boundary condition suits best the experimental condition, where a thin heater foil, attached to the bottom wall, is heating up the colder fluid flow.

In the case of a transient experiment, the heat flux situation is different. The hot fluid flow is heating up the channel walls. Due to the heater, the bulk temperature of the fluid flow is kept constant and is typically found to be around $T_B = 333.15 \text{ K}$. As mentioned before, the TLCs indicate the wall temperature by a change in color. The wall temperature, at which the color signal is evaluated, is $T_W = 313.15 \text{ K}$. Therefore, all channel walls are set at this constant temperature.

Boundary conditions for:

constant heat flux



constant wall temperature ($T_W=313.15 \text{ K}$)

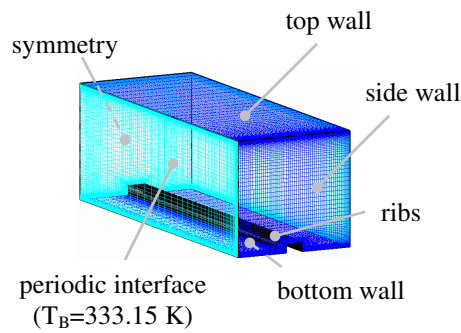


Fig. 3.2: Boundary conditions and boundary identification

3.5 FLUENTTM

The commercial software package FLUENTTM is capable of solving the differential equations for incompressible and weakly compressible fluid flows numerically. To do so, the differential equations are solved for each discrete volume of the generated grid individually. An integration and a following linearization of the differential equations results in a linear system of equations, which can then be resolved by the software. This control-volume-based technique is often called the finite-volume method.

There are two solvers implemented in FLUENTTM. The segregated solver, which is used in this study, solves the equations sequentially. Unfortunately, most of the equations are coupled or have a non-linear character. This leads to several iterations until a converged solution is reached. The software determines the residuals at the end of each iteration. The residuals provide a value of the computed changes for the unknown variables between two successive iterations, whereas a decreasing value is suggesting a converging numerical computation. In this study, a converged solution is

assumed, once all residuals drop below 10^{-5} . An example of a typical residual distribution is presented in Fig. 3.3.

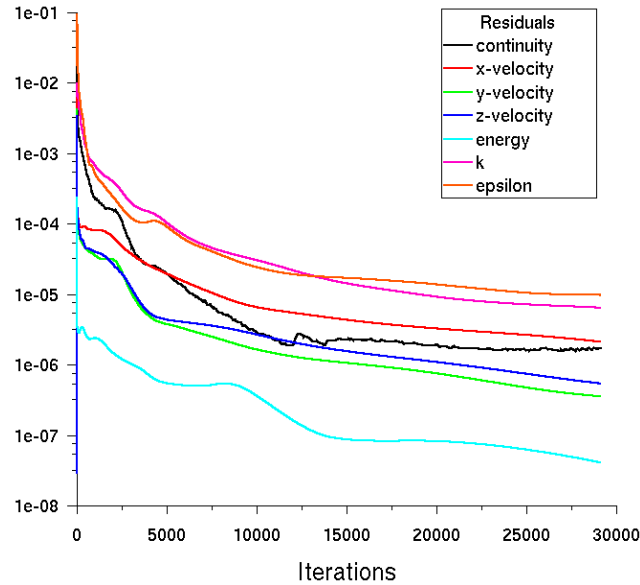


Fig. 3.3: Typical residual distribution

The coupling between the momentum and the energy equation is achieved by using the ideal gas law for the computation of the fluid density. Setting the density to a constant value implies an incompressible fluid flow. Information on the coupled solver, as it's not part of this investigation, is found in [19].

A linearization of non-linear equations could lead to a set of explicit or implicit equations. Within an explicit expression there is only one unknown variable, the unknown variable itself, so the equation can be solved separately. When the segregated solver is used, the linearization results in an implicit expression for every control volume and every governing equation. The single equation contains more than one unknown variable and therefore can not be solved directly. The corresponding equations of all cells in the computational domain have to be solved simultaneously.

Being aware, that a complex solver can not be fully explained in a brief overview, the author refers to the FLUENTTM user's guide [19] for further information.

4 Rib turbulators

4.1 V-shaped ribs (steady measurement technique)

As mentioned in the introduction, straight ribs have been replaced by V-shaped and later W-shaped ribs for various reasons. In this study, a total of four test cases dealing with V-shaped ribs are investigated. One purpose of this study is, to analyze the influence of the dimensionless rib height e/D_h on the heat transfer enhancement and the pressure loss. Therefore, two alternative dimensionless rib heights e/D_h were chosen to be investigated.

With a dimensionless rib height of $e/D_h = 0.0625$, this study examines a dimensionless rib height, which is typically found in applications for internal blade cooling. According to Table 1.1, this rib height is often found in literature, but data has been reported only within a limited Reynolds number range. A reduced dimensionless rib height should lead to a reduction of the pressure losses in a backside cooled combustor wall. Therefore, the non-dimensional rib height is reduced to $e/D_h = 0.02$ and the effect on the heat transfer augmentation and the pressure losses is investigated. As can be seen from Table 1.1, only a few investigations have been conducted on this topic, which also cover only a limited Reynolds number range. This study expands this Reynolds number range to conditions normally found in backside cooled combustor walls.

Another main purpose of this first set of test cases is to examine the effect of the total number of ribbed walls in a cooling channel. In channels with a rectangular cross section, as found in this study, the ribs are located on the larger channel walls. Most studies, dealing with internal cooling, concentrate on channels with ribs on two opposite channel walls, as it is commonly found in the field of internal blade cooling. For backside cooled combustor walls, where in contrast to internal blade cooling the heat load is applied only to one channel wall, a channel with ribs on one channel wall is a typical design layout. The effect of reducing the total number of ribbed channel walls on the heat transfer augmentation and the pressure losses haven't been analyzed sufficiently in the literature. This study aims to extend the information on this topic.

Table 4.1: Test case configuration V-shaped ribs

Test Case	Rib Type	P/e	e/D_h	Rib angle of attack	No. of Ribbed Walls
Smooth	-	-	-	-	-
L-V10-1s	V-shaped	10	0.0625	45°	1
L-V10-2s	V-shaped	10	0.0625	45°	2

Test Case	Rib Type	P/e	e/D_h	Rib angle of attack	No. of Ribbed Walls
V10-1s	V-shaped	10	0.02	45°	1
V10-2s	V-shaped	10	0.02	45°	2

The ribbed channel length-to-hydraulic diameter (l/D_h) is 7.5 for test cases V10-1s and V10-2s and 4.8 for test cases L-V10-1s and L-V10-2s. A minimum of five ribs are placed in front of the measurement region to achieve nearly periodic flow conditions. An overview over the four test cases including their labeling within this study is found in Table 4.1. To obtain a better understanding of the different rib heights, two pictures are presented in Fig. 4.1.

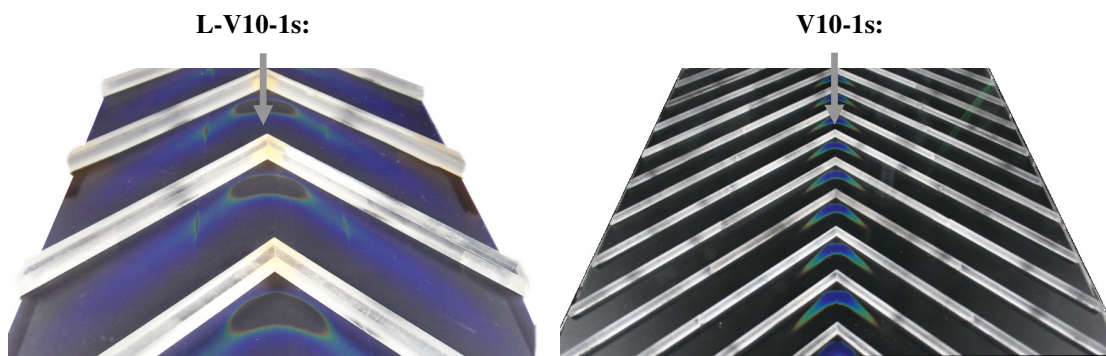


Fig. 4.1: Pictures of test cases L-V10-1s and V10-1s (flow direction from top to bottom)

In Fig. 4.1, one can observe the repeatability of the typical TLC color distribution. The number of ribs placed on the area, which is covered by the heater foil, seems to be sufficient to assume periodic conditions.

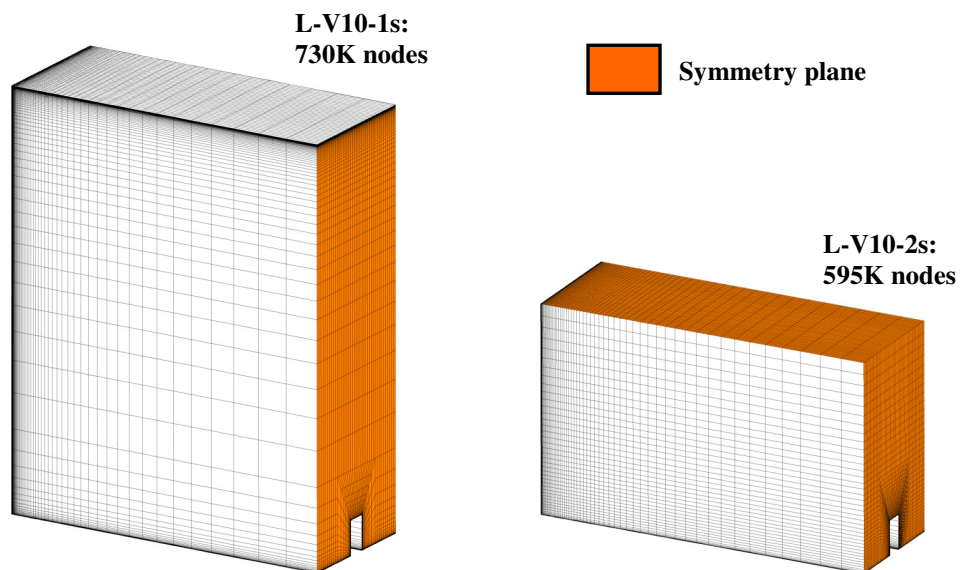


Fig. 4.2: Grids and number of nodes for test cases L-V10-1s and L-V10-2s

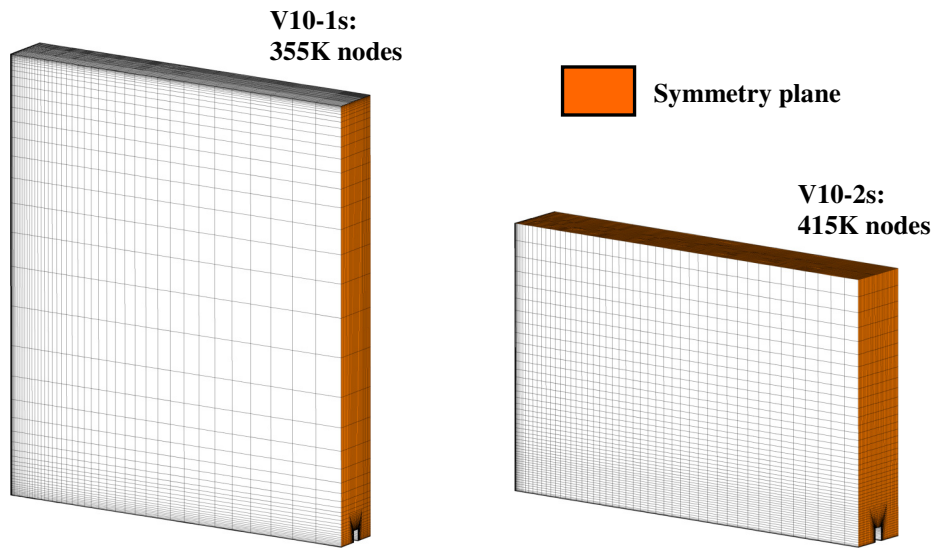


Fig. 4.3: Grids and number of nodes for test cases V10-1s and V10-2s

For the numerical computation, a periodic segment of each test case is meshed. The grid size depends on the overall volume of the computational domain. As mentioned before, the maximum number of symmetry planes found in the respective test cases is used to reduce the computational effort. The grids are skewed with respect to the rib angle of attack. In general, the number of nodes for test cases L-V10-1s and L-V10-2s is higher compared to the test cases V10-1s and V10-2s. For all test cases the demand of a dimensionless wall distance around $y^+ \approx 1$ is satisfied. The total number of nodes varies from 355,000 to 730,000. A sketch of the obtained grids is presented in Fig. 4.2 and Fig. 4.3.

Velocity field

Knowing the flow field structures allows drawing conclusions on the heat transfer and friction factor situation. The identification of separation and re-attachment zones for example can be interpreted as a region of a reduced or intensified heat transfer augmentation. For the present test cases, the rib geometry mainly determines the air flow and its secondary flow structures. Mean velocity profiles for all test cases are presented in Fig. 4.4 for a description of the flow field situation.

The CFD computations reveal the existence of two counter rotating vortices in channels with ribs placed on one channel wall only. Each of the vortices fills out one half of the channel cross section. The distribution of the mean velocity profiles shows that the maximum velocity is aligned with the position of the vortex center and is located in the centre of the presented channel half. This is in contrast to the reported flow field situation for so-called asymmetric channel flows with one roughened channel wall.

Hanjalic and Launder [26] investigated an internal channel flow with 90° ribs on one channel wall. The channel had an aspect ratio of $AR = 6:1$ and the dimensionless rib height was $e/D_h = 0.0589$. The rib pitch-to-height ratio was $P/e = 10$. A diagram of the

reported velocity profile plotted over the dimensionless channel height is presented in Fig. 4.5. The experimental data reveals that the location of the maximum velocity is not found in the middle between the ribbed channel wall and smooth channel wall. In their study, the effect of the ribbed wall on the mean velocity profile results in a displacement of the maximum velocity towards the smooth channel wall. In the present study, the influence of the strong secondary flow vortices due to the V-shape of the ribs shift the velocity profile towards the ribbed channel wall, which leads to a reduced asymmetric flow behavior.

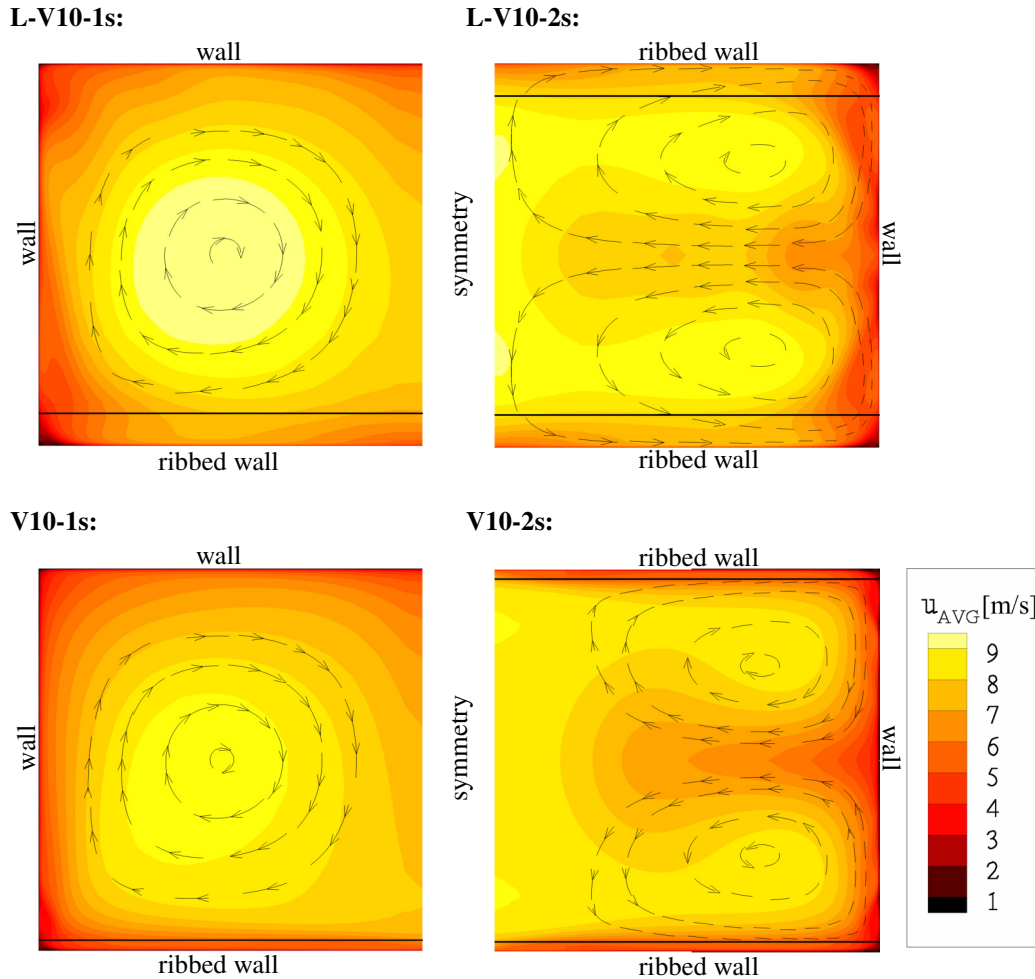


Fig. 4.4: Computational mean velocity profiles and secondary flows for test cases L-V10-1s, L-V10-1s, V10-1s and V10-2s at $Re_D \sim 130K$

In the case of channels with two opposed ribbed channel walls, the numerical computations predicts a total of four vortices. Each quarter of the channel cross section is accommodating one vortex. Looking more closely at the mean velocity profiles, it is noticeable that the location of the vortex center is shifted towards the smooth channel sidewall compared to the channel with ribs only on one channel wall. Again a local mean velocity maximum is aligned with the vortex center.

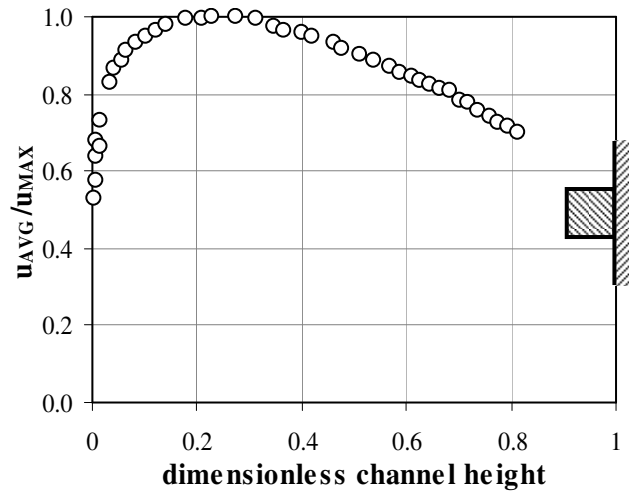


Fig. 4.5: Mean velocity profile in an asymmetric channel with 90° ribs (data taken from [26])

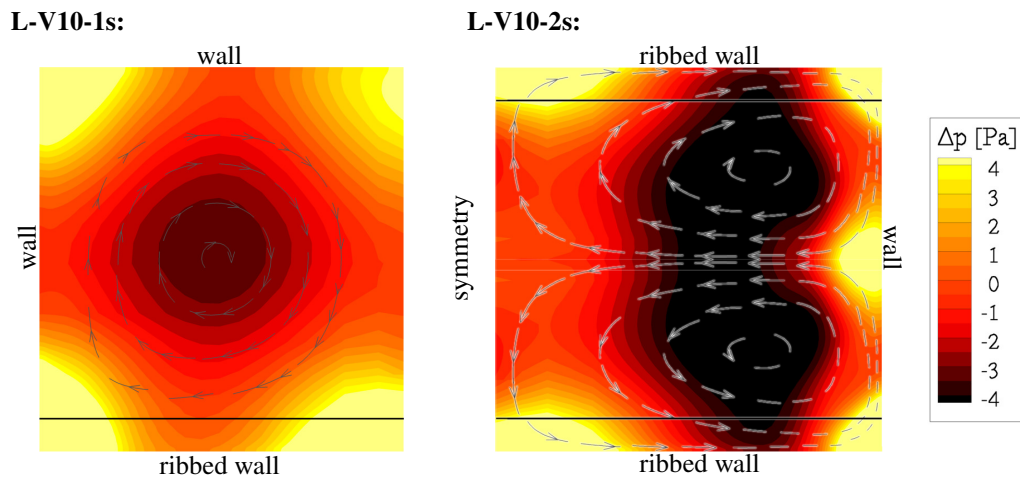


Fig. 4.6: Regions of low and high pressure at cross section of test case L-V10-1s and L-V10-2s at $Re_D \sim 130K$

Looking at the static pressure distribution of test cases L-V10-1s and L-V10-2s as presented in Fig. 4.6, it can be observed, that not only the maximum velocity is found at the location of the vortex center; also the static pressure is below the mean pressure in the cross-section at this position. A region of low pressure always leads to a suction of the nearby mass and provides flow acceleration. It is also noticeable, that in a two-sided ribbed channel the minimum pressure is lower.

In contrast to the test cases with one ribbed channel wall, the location of the global maximum velocity is not in consistence with the location of the vortex center. Two small cells near the symmetry plane right above the rib tip can be observed in Fig. 4.4, at which the mean velocity maximizes. Also, this region of higher velocities is found for a one-sided ribbed channel. The occurrence of these regions with a high mean velocity

can be explained by looking at the static pressure situation close to the ribbed wall as presented in Fig. 4.7.

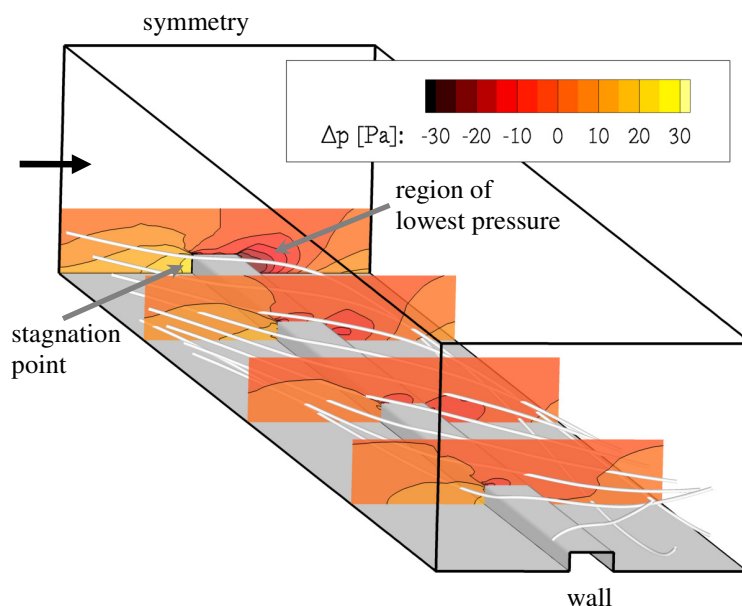


Fig. 4.7: Streamtraces and regions of low and high pressure near the ribbed wall of test case L-V10-1s at $Re_D \sim 130K$

In front of the rib tip close to the symmetry plane a region of high pressure is found. Here, the arriving air flow is retarded until the stagnation point at the rib tip is reached. Right behind the rib, the air flow is detached, which leads to a region of recirculation and low pressure. The lowest values are located behind the rib close to the symmetry wall. As mentioned before this region of low pressure and the associated increased pressure gradient acts as a driving force and accelerates the stream traces beyond it. Proceeding towards the channel side wall, this region of low pressure is reduced and vanishes completely, once the side wall is reached. However, the stream traces, which originate close to the symmetry wall, are accelerated and diverted. Behind the rib the stream traces are more or less aligned parallel with respect to the rib. Keeping in mind, that the strongest acceleration is located close to the symmetry plane, higher mean velocities can be found close to the rib tip.

Here, the acceleration of the flow field is not enough, so that the velocity close to the symmetry plane maximizes. However, the mean velocities above the rib tip show higher values compared to the region on the opposite smooth wall. This indicates clearly that a certain level of acceleration also exists in the case of a one-sided ribbed channel.

In Fig. 4.8 the flow situation close to the ribbed wall is presented for test cases L-V10-1s and L-V10-2s. Once again, it can be observed, that the stream traces are diverted and aligned parallel with respect to the rib. Looking at the cut view presentation, it is noticeable, that two vortices are formed. One of them is located in the stagnation region in front of the rib and one vortex is found in the region behind the rib. But in contrast to 90° ribbed channels the air is not trapped inside these vortices. As can

be seen from the top view, the mass is transported within the vortices from the symmetry plane towards the smooth channel side wall. The general flow situation close to the ribbed wall comparing a one-sided ribbed channel with a two-sided ribbed channels reveals no major differences.

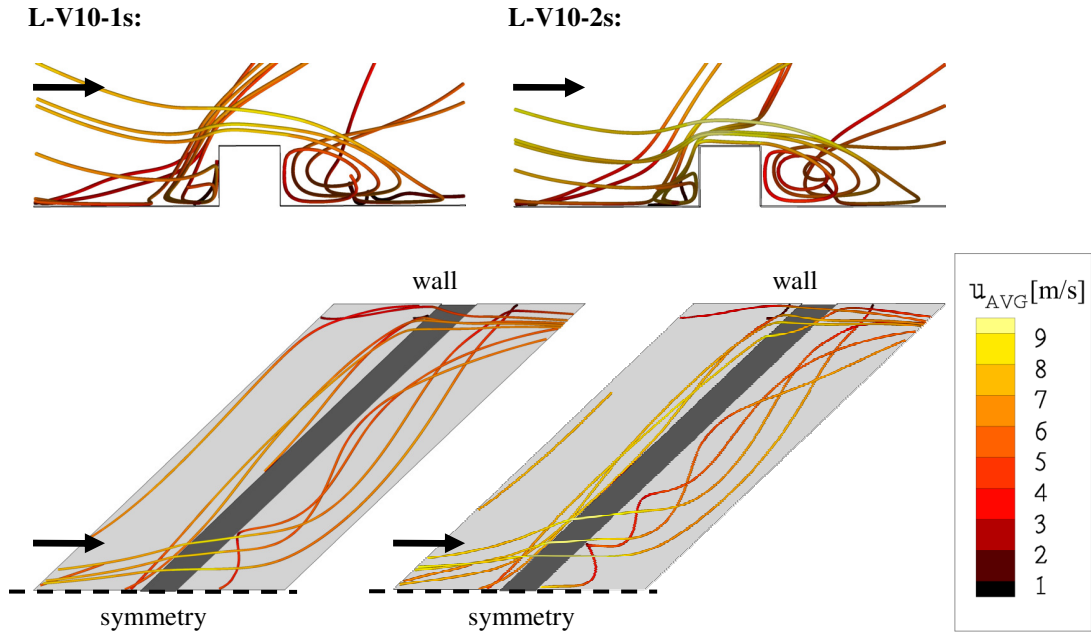


Fig. 4.8: Flow situation of test cases L-V10-1s and L-V10-2s close to the ribbed wall at $Re_D \sim 130K$

Friction factor

As mentioned in the introduction, knowing the friction factor of the tested rib geometries is important to be able to assess the thermal performance η . Besides this, the level of the friction factor is a more critical fact for backside cooled combustor walls, since a high amount of compressor air have to pass through those channels, where the convective cooling technique is applied. A low pressure penalty is therefore desired.

The friction factor ratios f/f_0 of test cases L-V10-1s and L-V10-2s are presented in Fig. 4.9 (see Appendix B for error analysis). Looking at test case L-V10-2s, increasing friction factor ratios f/f_0 for an increasing Reynolds number are noticeable. This increasing behavior is mainly caused by a reduction of the friction factor of a smooth channel f_0 for an increasing Reynolds number. Within this first set of investigations, the friction factor f remains nearly constant above a Reynolds number of $Re_D > 160,000$.

A look at the numerically and experimentally obtained data shows, that the results are in good agreement for Reynolds numbers below $Re_D < 160,000$. Above this Reynolds number, the numerically obtained data seem to underpredict the experimental results. Still the prediction of the computation is within a deviation of approximately 25%. Comparing the results for a one-sided and two-sided ribbed cooling channel it is

observable that the introduction of a second ribbed wall doubles approximately the friction factor ratios.

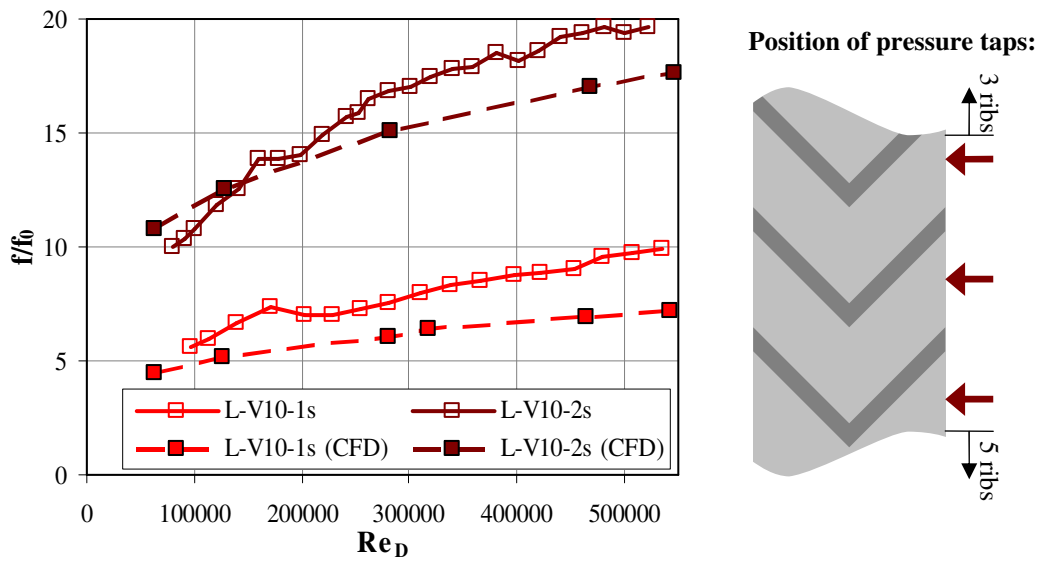


Fig. 4.9: Friction factor ratios f/f_0 for test cases L-V10-1s and L-V10-2s

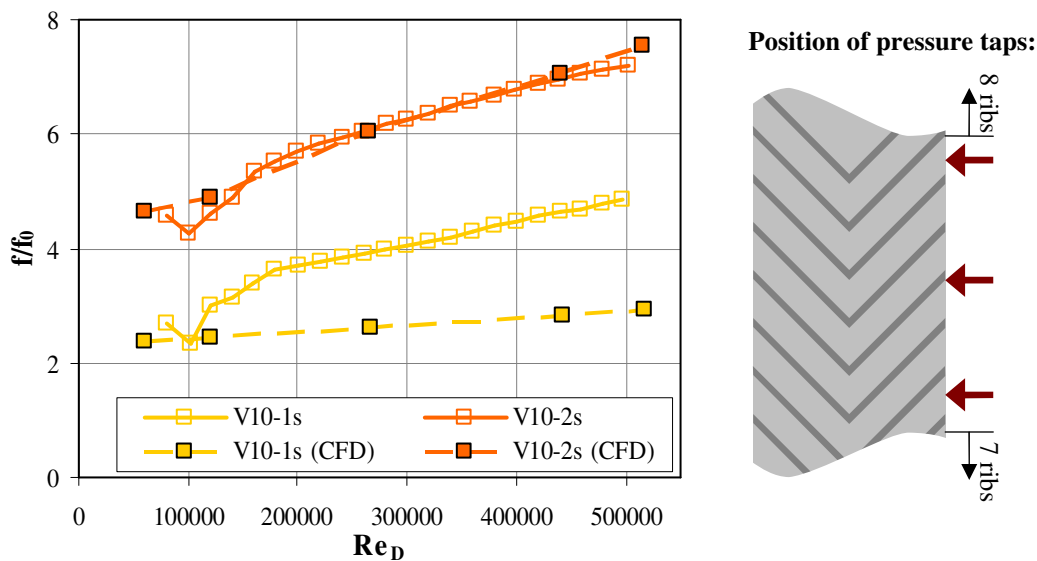


Fig. 4.10: Friction factor ratios f/f_0 for test cases V10-1s and V10-2s

To support the accuracy of the presented results, data from an earlier study conducted by Han et al. [25] is mentioned. They investigated a geometry corresponding to test case L-V10-2s. In their study, a friction factor ratio f/f_0 of 9.98 was measured at a Reynolds number of 90,000. The data agrees reasonably well with the data presented in this study, keeping in mind that Han et al. conducted their study in a channel with an aspect ratio of $AR = 1:1$.

Looking at the results for test case V10-1s and V10-2s as presented in Fig. 4.10, similar conclusions can be drawn. The friction factor ratio increases, if a second ribbed wall is introduced. Also the numerical computations are in good agreement with the experimentally obtained data for Reynolds numbers below $Re_D < 160,000$. Above this Reynolds number the situation is different. For test case V10-2s the agreement is still good, whereas for test case V10-1s the gap between experimentally and numerically obtained results is bigger than it is for all other test cases. The maximum deviation is 60 % for the highest observed Reynolds number. It has to be noted, that for test case V10-1s the highest observed pressure gradient is around 80 Pa per meter, which is lower than for all other test cases. It seems likely, that reaching levels of lower pressure losses has an impact on the prediction capability of the used numerical setup.

It might be obvious, but still worth mentioning, that the reduction of the dimensionless rib height e/D_h leads to a significant reduction of the friction factor ratios. The effect of a reduced rib height on the heat transfer enhancement is discussed in the following section.

Heat transfer enhancement

For backside cooled combustor walls not only the area-averaged level of convective heat transfer enhancement is of interest, but also the local distribution of the heat transfer augmentation has to be investigated. Here, regionally limited high heat transfer peaks could lead to very intense amounts of heat load, which could cause a breakdown of the structure, e.g. due to high thermal stresses. Therefore, it is desired to create a homogenous distribution of heat transfer augmentation.

The experimental local heat transfer ratios of the first set of test cases are presented in Fig. 4.11. Looking at the local distributions two main relations can be observed. For all investigated test cases, the heat transfer enhancement peak, which is located behind the rib tip, is decreasing with an increasing Reynolds number. Similar observations have been reported by Su et al. [56] for a Reynolds number range of 10,000 to 500,000 from a numerical study.

Comparing the experimental results of a one-sided ribbed channel and a two-sided ribbed channel at the same Reynolds number, another interesting fact is noticeable. The heat transfer augmentation peak is more intense in the case of a two-sided ribbed channel. Also the overall local heat transfer enhancement levels are higher, which leads to a higher area-averaged heat transfer augmentation. Looking at the distribution of the local heat transfer enhancement close to the channel sidewalls, it is noticeable that there are regions of low Nusselt number ratios. In general, it is challenging to provide the necessary heat transfer levels in the regions close to the channel sidewalls. Especially here, it is of importance to provide a certain level of heat transfer enhancement to prevent damage due to the high component temperatures. In test cases with smaller ribs, the regions of low Nusselt number ratios are even wider spread.

For the further evaluation of the investigated test cases, the area-averaged Nusselt number ratios have to be evaluated. The experimentally and numerically obtained data of test cases L-V10-1s and L-V10-2s are presented in Fig. 4.12. The overall agreement of experimental results and the numerical computations is within 16 %. All presented data sets show a more or less constant behavior of the Nusselt number ratios with an increasing Reynolds number. More precisely, the experimental data tend to increase slightly for the highest Reynolds number investigated in this study, whereas the numerical computations first show a reduction of the heat transfer enhancement for lower Reynolds numbers and then remains on a constant level.

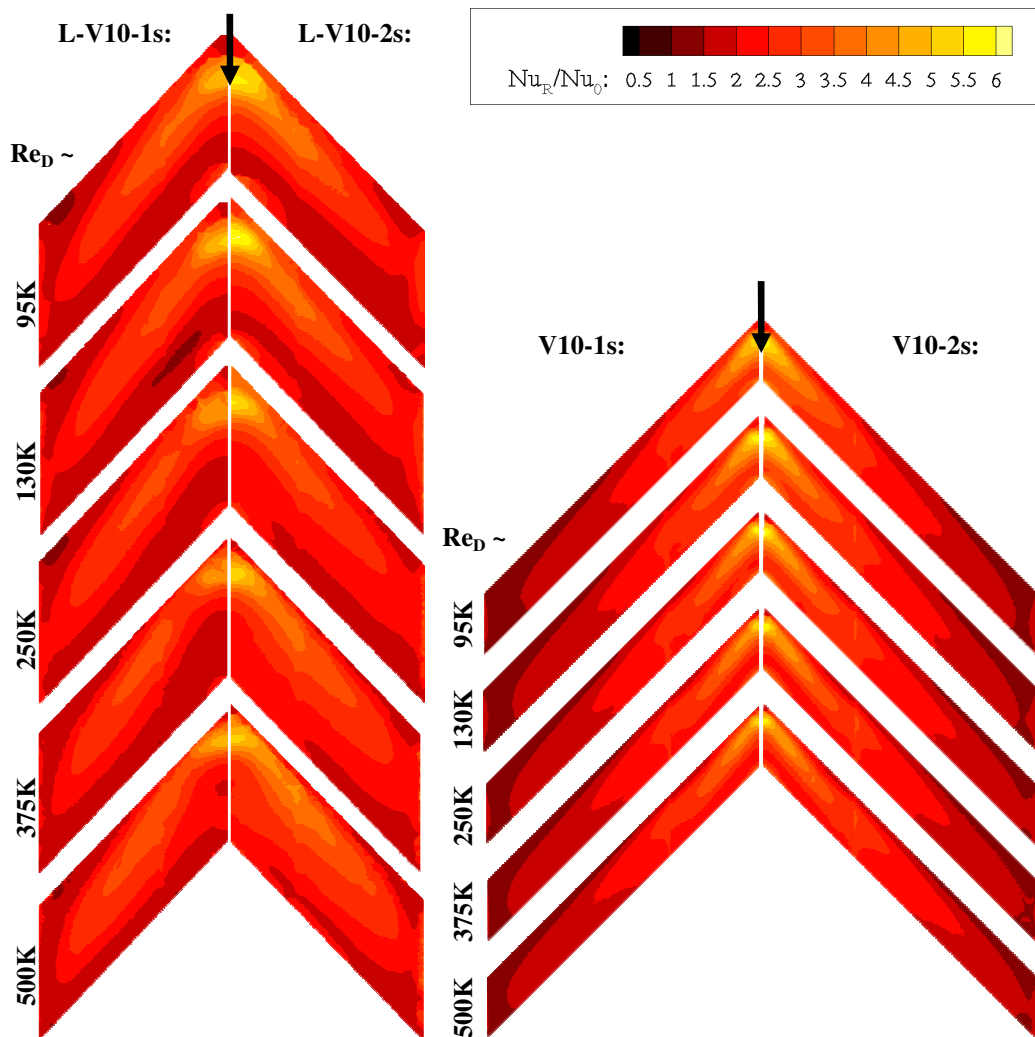


Fig. 4.11: Experimental local heat transfer ratios of test cases L-V10-1s, L-V10-1s, V10-1s and V10-2s

The data set for test cases V10-1s and V10-2s are presented in Fig. 4.13 and the trends are similar to the ones described above. The reduction of the Nusselt number ratios in the numerical computations is now observable up to a Reynolds number of $Re_D < 200,000$. Looking at the experimental results, the constant trend of the heat transfer augmentation with an increasing Reynolds number is even more pronounced.

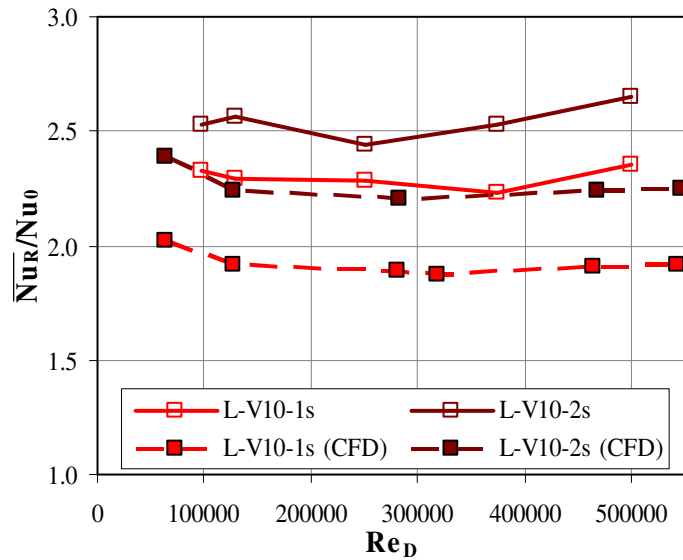


Fig. 4.12: Area-averaged heat transfer enhancement for test cases L-V10-1s and L-V10-2s

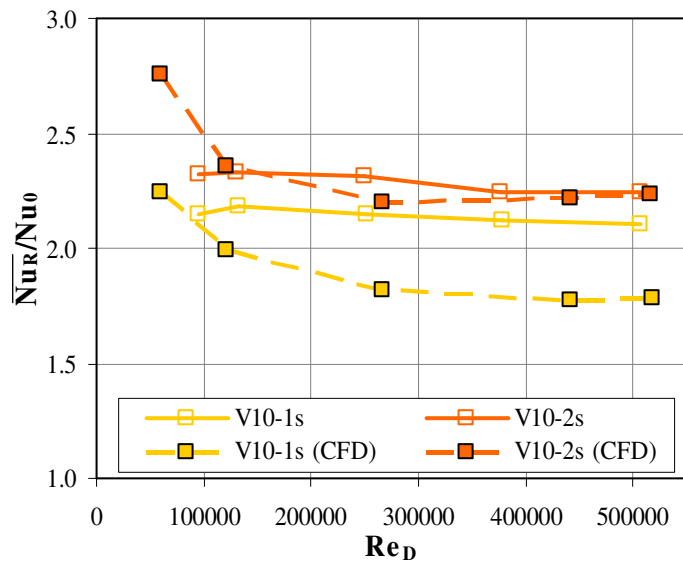


Fig. 4.13: Area-averaged heat transfer enhancement for test cases V10-1s and V10-2s

To summarize, it can be mentioned, that a decline of the rib height is reducing the area-averaged heat transfer augmentation. Introducing a second ribbed wall is increasing the area-averaged heat transfer enhancement. Once again, the data reported by Han et al. [25] is in good agreement. In their study, they investigated a geometry, which corresponds to test case L-V10-2s and measured a Nusselt number ratio of 2.34 at a Reynolds number of 90,000. For completeness, it has to be mentioned that their test section had an aspect ratio of $AR = 1:1$ compared to an aspect ratio of $AR = 2:1$ in the current study.

4.2 V-shaped ribs (transient measurement technique)

As mentioned earlier, the introduction of the transient measurement technique offers many advantages. As a first step, this technique is implemented into the test rig and the results of the new measurement technique are compared with the existing data of the steady measurement technique. This is done experimentally and numerically for test case V10-1s. In another step, further investigations on V-shaped ribbed cooling channels are conducted.

To date, there are very few investigations available in literature addressing a variation of the rib pitch-to-height for rib configurations more complex than straight ribs. Liu et al. [40] presented a rib pitch-to-height variation from 10 to 3 for 45° angled ribs. The dimensionless rib height was kept at $e/D_h = 0.094$ and the Reynolds number varied from 5,000 to 40,000. In their study the best overall thermal performance η including the rib surfaces was found for the closest rib spacing. This indicates, that the optimum of the rib pitch-to-height was not related to $P/e = 10$, the optimum for 90° ribs. Attention is given in this study to investigate the effects of rib pitch-to-height on friction factor and heat transfer enhancement. Due to the promising results from the above mentioned study, the rib pitch-to-height is reduced to a value of $P/e = 5$. An overview over the test cases in this section is presented in Table 4.2.

Table 4.2: Test case configuration V-shaped ribs

Test Case	Rib Type	P/e	e/D_h	Rib angle of attack	No. of Ribbed Walls
V10-1s	V-shaped	10	0.02	45°	1
V5-1s	V-shaped	5	0.02	45°	1

The ribbed channel length-to-hydraulic diameter (l/D_h) is 5 for test cases V10-1s and 2.5 for test cases V5-1s. A minimum of fifteen ribs are placed in front of the measurement region to achieve nearly periodic flow conditions. To obtain an impression of the different rib spacing, images of test case V10-1s and V5-1s are presented in Fig. 4.14.

For the numerical computation of test case V10-1s, the earlier generated mesh is used. At this point the thermal boundary condition is changed from a constant heat flux boundary condition to a constant wall temperature boundary condition. For test case V5-1s a new mesh is created. The total number of nodes is slightly lower than for test case V10-1s due to the smaller computational domain. In all cases, the requirements of a dimensionless wall distance around $y^+ \approx 1$ is satisfied. A sketch of the grids used is presented in Fig. 4.15.

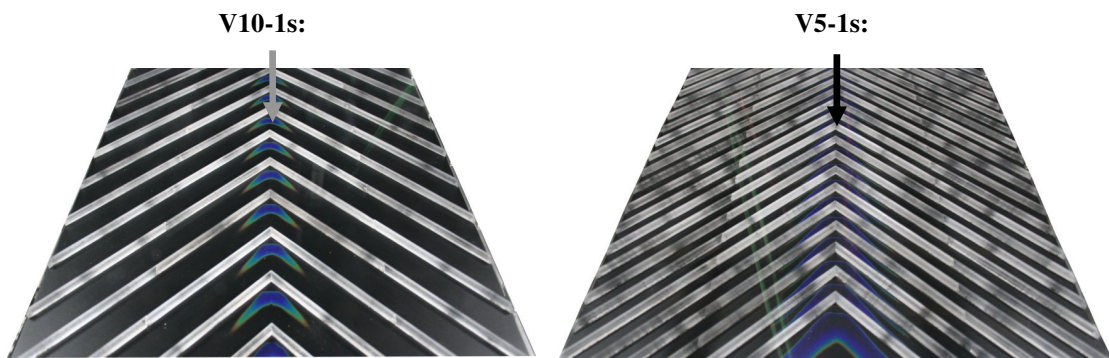


Fig. 4.14: Images of test cases V10-1s and V5-1s

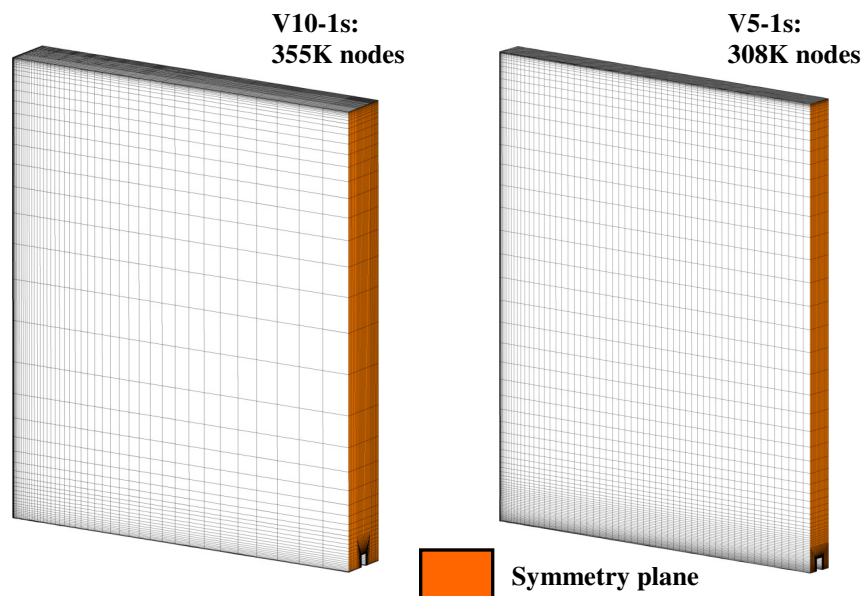


Fig. 4.15: Grids and number of nodes for test cases V10-1s and V5-1s

Velocity field

The discussion of the obtained results is started with the velocity field. The computational mean velocity profiles of test case V10-1s and V5-1s are presented in Fig. 4.16.

Comparing the effect of the changed thermal boundary condition of test case V10-1s, it can be noted, that the overall mean velocity distribution is similar for a constant temperature boundary condition and a constant heat flux boundary condition. Only a slightly higher mean velocity maximum is noticeable in the computation, where a constant temperature boundary condition is applied. During all numerical computations the mass flow is kept constant. Due to the overall higher temperature environment within the computation having a constant wall temperature boundary condition, the mean average velocity is slightly higher, as the volume-averaged density is lower.

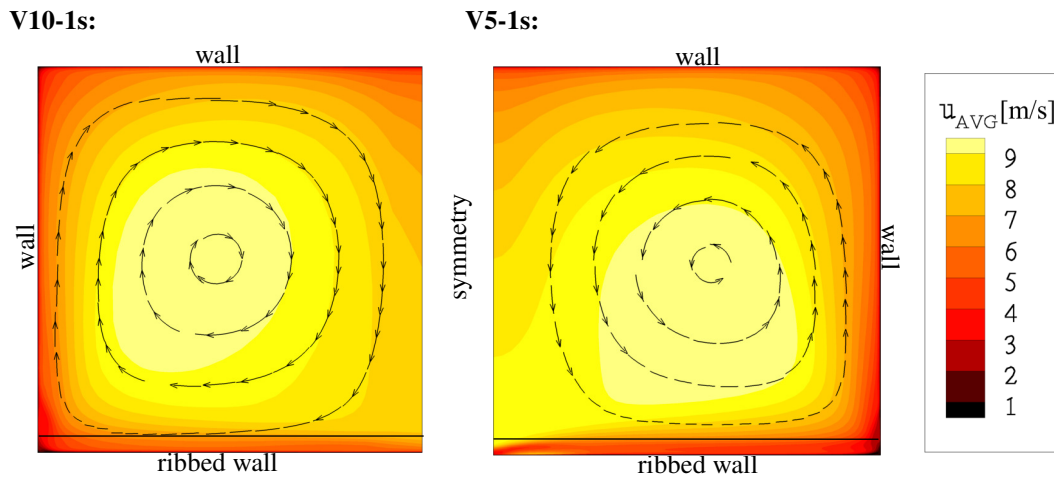


Fig. 4.16: Computational mean velocity profiles and secondary flows for test cases V10-1s and V5-1s at $Re_D \sim 130K$

As for test case V10-1s two counter rotating vortices are found in each half of the channel cross section. In the case of test case V5-1s the region of maximum mean velocity seems to be shifted slightly towards the ribbed wall. Also the mean velocity above the rib tip is higher for test case V5-1s.

For the heat transfer augmentation of the ribbed channel wall, the flow situation close to this wall is of importance. Therefore, sketches of stream traces close to the ribbed wall are presented in Fig. 4.17.

The flow field situation of test case V10-1s is quite similar to the flow field situation of test case L-V10-1s as described before. The stream traces are squeezed together as they approach a V-shaped rib, which leads to an increase of the mean velocity. Once the rib is passed, the flow detaches and a recirculation zone behind the rib is formed. The resulting vortex develops from the symmetry plane towards the channel side wall, where the stream traces are ejected into the main air flow. It is interesting to mention, that close to the symmetry plane, where this vortex is created, the distance to the rib in front is small and that the swirling motion is more intense. This effect can be associated with the region of low pressure, which is located in this very same region.

Further downstream the flow reattaches and the thickness of the developing boundary layer starts to increase, which leads to a decreasing heat transfer augmentation. All stream traces between two successive ribs are aligned parallel to the ribs. As for test case L-V10-1s, a small vortex is located right in front of the rib.

For test case V5-1s, the flow field situation between two successive ribs is different. Here, only one vortex can be observed. As for test case V10-1s, the swirl of this vortex is more intense close to the symmetry plane. Looking at stream traces slightly above the rib, it is noticeable, that only a part of the air flow is diverted into the region of two successive ribs, whereas other stream traces, which are also close to this region, remain

undisturbed. Those are only diverted towards the channel sidewall due to the accelerating force of the vortex between the ribs.

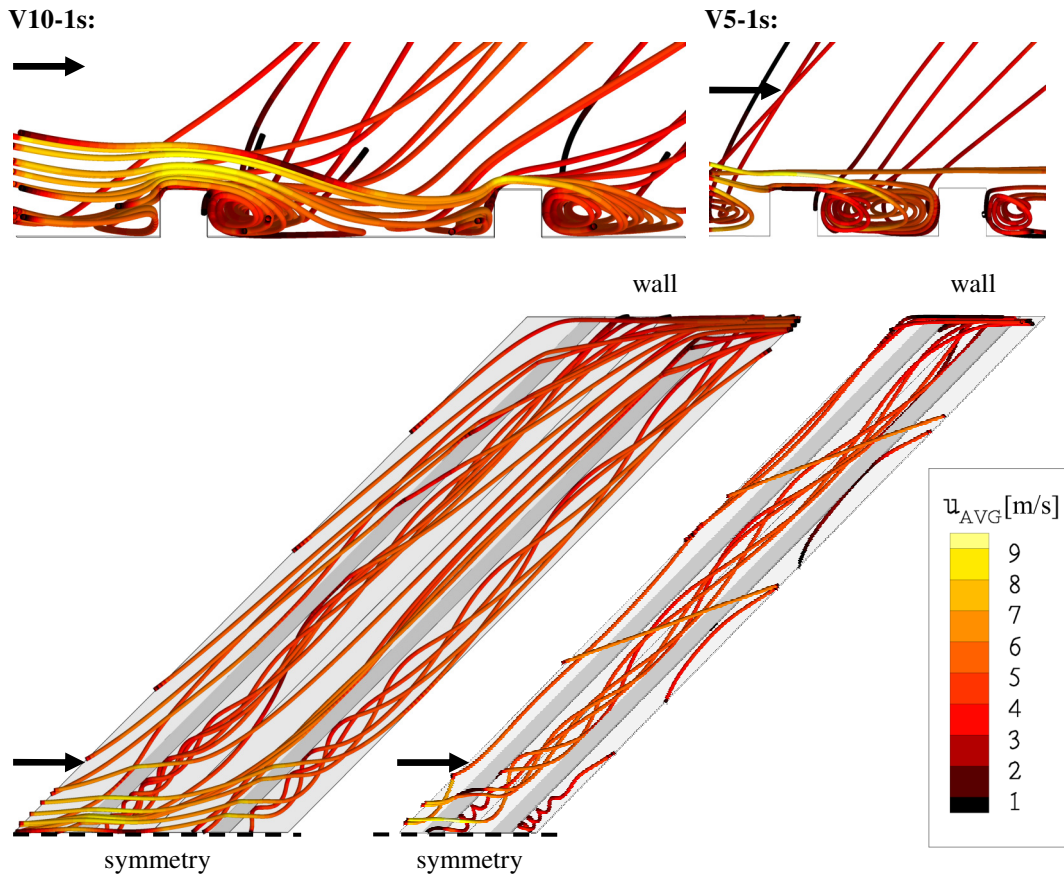


Fig. 4.17: Flow situation of test cases V10-1s and V5-1s close to the ribbed wall at $Re_D \sim 130K$

For a flow situation with straight 90° ribs and a rib pitch-to-height of $P/e = 5$, the flow is continuously kept in between the ribs. In this case, there is no exchange of air from the main flow into the region between two successive ribs. In contrast to this mechanism, the situation changes, if the 90° ribs are replaced by inclined or V-shaped ribs. As could be seen from Fig. 4.17, there is some exchange of air from the main flow into the region between two successive ribs. Therefore, a reduction of the heat transfer augmentation should not be observed as it would be the case for 90° straight ribs. Similar findings have been reported by Liu et al. [40] for a channel with aligned ribs.

Friction factor

It is important to know the friction factor ratios for a comprehensive assessment of the cooling ability of a V-shaped ribbed channel with a reduced rib pitch-to-height. For this reason, the friction factor ratios of test cases V10-1s and V5-1s are presented in Fig. 4.18.

Looking at the obtained data, a significant decline of the friction factor ratio is observed, if the rib pitch-to-height is reduced. A main reason for this is found by

recalling the above described flow field situation. In the case of test case V10-1s, the stream traces close to the rib channel wall show more disturbances, which might lead to a higher pressure loss.

Comparing the numerically and experimentally obtained data, it is evident that the poor prediction of the friction factor ratio of test case V10-1s becomes also evident in the case of test case V5-1s. The standard k- ϵ turbulence model is not able to compute data points close to the experimental data. Still, the offset is reduced in the case of test case V5-1s. Also, the trend of a slightly reduced friction factor ratio with a decreasing rib pitch-to-height is captured by the numerical computation.

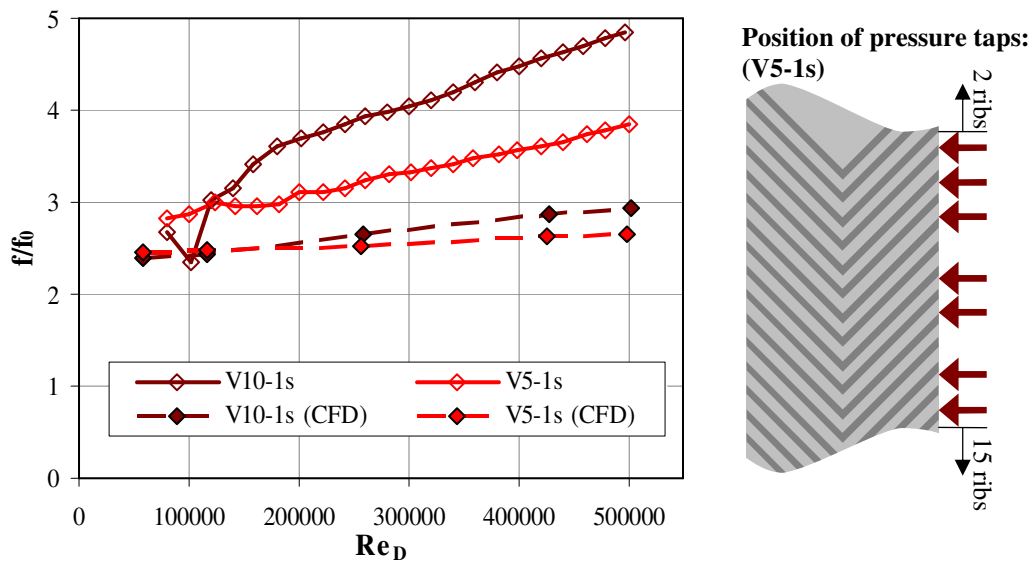


Fig. 4.18: Friction factor ratios ff_0 of test cases V10-1s and V5-1s

Comparison of different heat transfer measurement techniques

The experimentally obtained data is presented in Fig. 4.19. It has to be mentioned, that the area-averaged Nusselt number evaluated from the steady measurement technique is normalized by the so-called Dittus-Boelter correlation (see equation (2.9)). For the transient measurement technique a correlation proposed by Kays et al. [31] (see equation (2.14)) is used. This is done to account for the earlier mentioned Nusselt number measurements of the smooth channel wall and the different thermal boundary conditions. As could be seen from the figure, the experimental data of the different measurement techniques agrees very well.

Kays et al. [31] reported that the different thermal boundary conditions for a fully turbulent internal flow in a smooth tube could lead to a slightly different Nusselt number. Their correlations show that the Nusselt number obtained in an experiment with constant heat flux is generally 4.7 % higher than the Nusselt number found with a constant wall temperature. Nevertheless, the influence of the thermal boundary condition is considered to be minor.

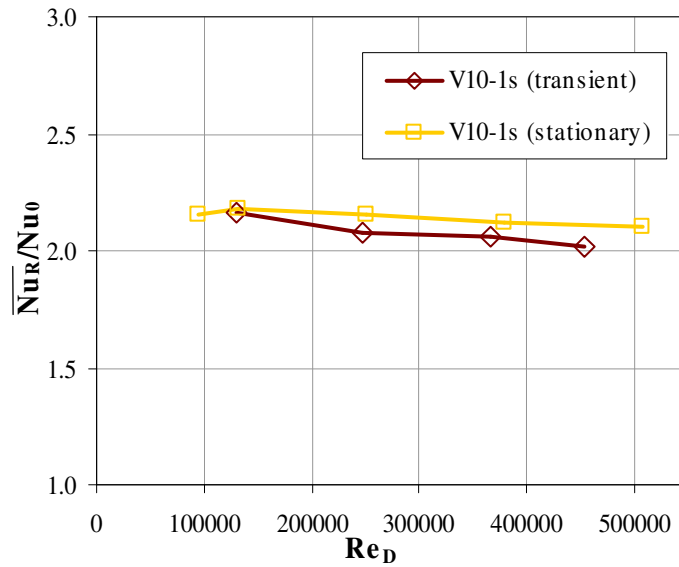


Fig. 4.19: Comparison of area-averaged heat transfer augmentation of test case V10-1s with different measurement techniques

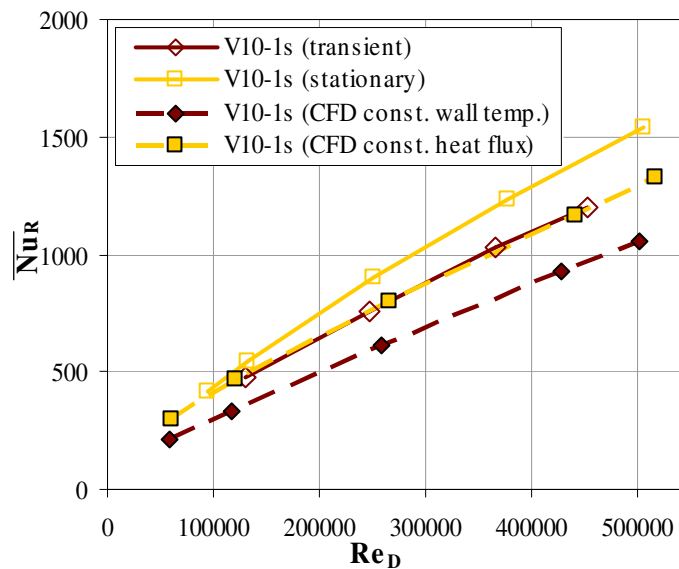


Fig. 4.20: Area-averaged Nusselt number of experiment and numerical computations with two different boundary conditions

In Fig. 4.20 the Nusselt number of the experiment and the numerical computations with the two different boundary conditions are presented. The results show that the difference between the two measurement techniques is somewhat higher than the reported 4.7%. For the numerical computations similar findings are present. The computations with a constant heat flux boundary provide higher Nusselt numbers than the numerical computations with a constant wall temperature. The difference between the two approaches fits well with the difference between the two experimental

techniques. Therefore, the numerical approach to associate the respective thermal boundary conditions with the experimental technique is considered to be appropriate.

Heat transfer enhancement

The local heat transfer ratios, obtained with the transient measurement technique, are presented in Fig. 4.21. Comparing the results of test case V10-1s with the obtained data from the steady measurement technique, as found in Fig. 4.11, reveals, that there are no viewable differences in the resulting local heat transfer characteristics. The maximum heat transfer ratio is located right behind the rib tip and its level is decreasing with an increasing Reynolds number. This is also true for test case V5-1s. For both test cases, the level of heat transfer augmentation is approximately similar in the region close to the symmetry plane. To assess the cooling ability, the decrease of heat transfer enhancement starting at the symmetry plane and proceeding towards the channel side wall has to be investigated. In the case of a rib pitch-to-height of $P/e = 5$, the level of heat transfer augmentation decays faster than it does for test case V10-1s. For test case V5-1s, this leads to a relatively large area between two successive ribs with a low heat transfer augmentation.

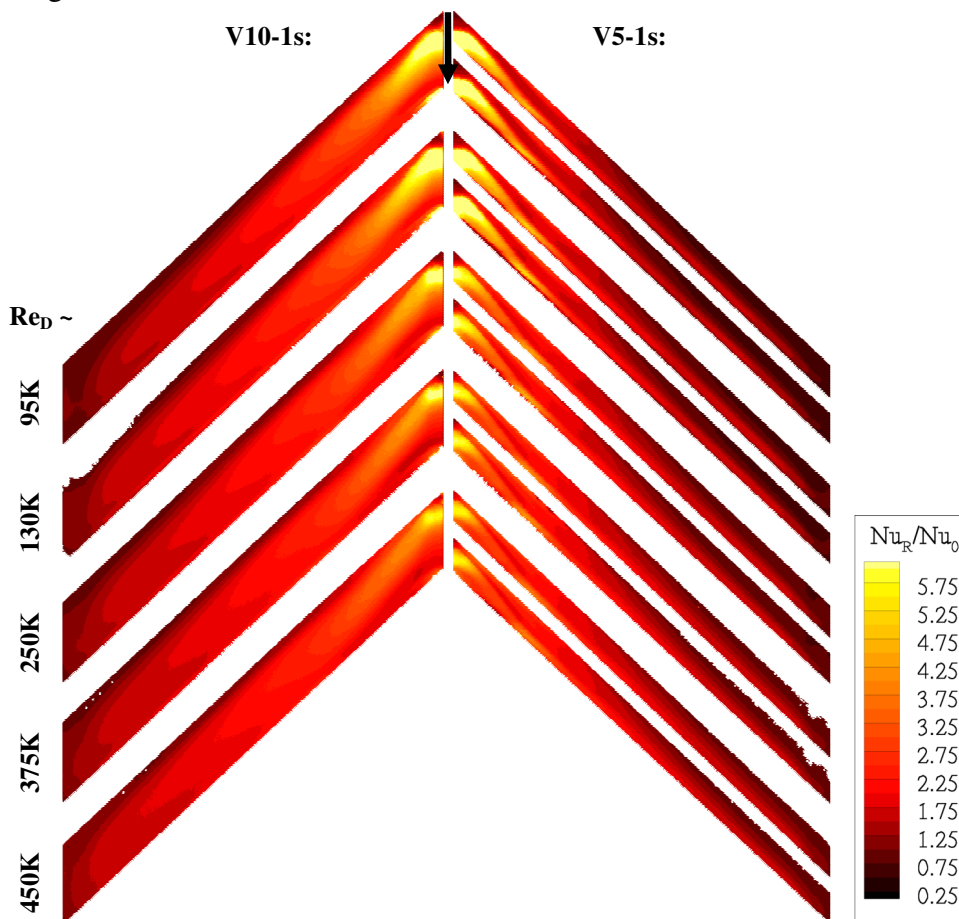


Fig. 4.21: Experimental local heat transfer ratios of test cases V10-1s and V5-1s

In Fig. 4.22 the influence of the rib pitch-to-height ratio on the area-averaged heat transfer ratios is presented. From the local heat transfer ratios, it can be seen, that the area-averaged heat transfer ratios of test case V5-1s are lower compared to the data points of test case V10-1s. The overall trend of the Nusselt number ratios shows a nearly constant behavior with an increasing Reynolds number, except for the smallest Reynolds number investigated. Similar findings have been reported for test cases L-V10-1s, L-V10-2s, V10-2s and by Bunker and Osgood [7] for inclined ribs.

Comparing the numerically and experimentally obtained results reveals, that the numerical computation underpredicts the experiments by approximately 30 %. However, the trend of the experiment is captured.

Adding more ribs onto the channel wall increases the total surface area, which has a favorable impact on the overall heat transfer. In the case of V10-1s, the surface area is increased by 28 %, whereas for test case V5-1s the surface area is increased by 57 %. With this, the heat transfer on the rib itself is no longer negligible, if the cooling ability of ribbed channels is to be assessed. Using the transient measurement techniques only, it is not possible to evaluate experimental data on the rib surface. Using the so-called lumped heat-capacitance technique allows obtaining data of the average heat transfer coefficient for the rib itself. Within this study, only two test case configurations with W-shaped ribs are investigated to study the influence of this effect, to limit the experimental effort.

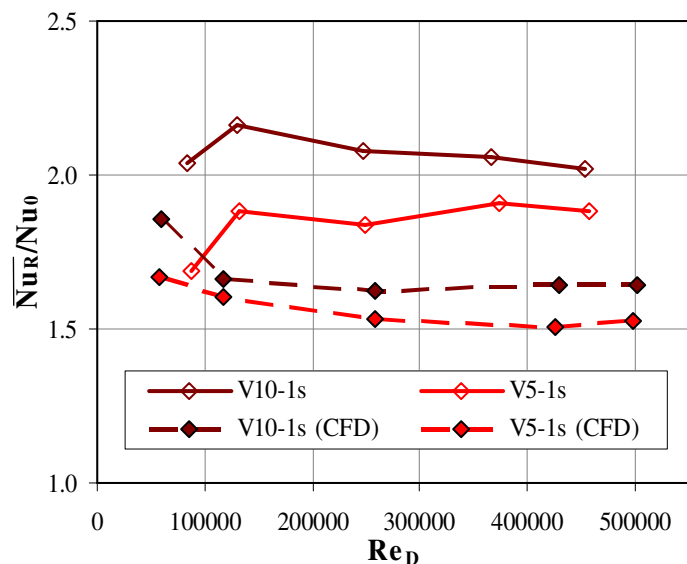


Fig. 4.22: Area-averaged Nusselt number ratio of test case V10-1s and V5-1s

4.3 V-shaped ribs (Real geometry effects)

Backside cooled combustor walls with convective cooling devices are normally manufactured by a casting process. The shrinking of the poured material results in the

formation of rounded edges instead of sharp edges. Therefore, it has to be investigated, how the casting imperfections influence the friction factor and heat transfer ratios. To do so, the rib cross section of test case V10-1s is altered to model the casting imperfections. As presented in Fig. 4.23, bevels have been added to each top edges of the rib's cross section. The overall rib height remained unaltered. The influence of the bottom edge imperfections is assumed to be minor and is therefore neglected. The parameters of the investigated test cases are presented in Table 4.3.

Table 4.3: Test case configuration with modeled casting imperfection

Test Case	Rib Type	P/e	e/D_h	Rib angle of attack	No. of Ribbed Walls
V10-1s	V-shaped	10	0.02	45°	1
V10-1s B	V-shaped with bevel	10	0.02	45°	1

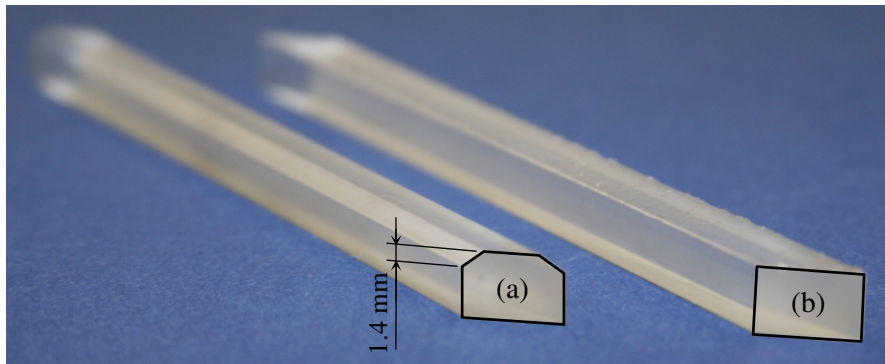


Fig. 4.23: (a) rib with modeled casting imperfections and (b) ideal rib

Friction factor

As a first step in the discussion on the influence of casting effects, the friction factor ratios of test cases V10-1s and V10-1s B are presented in Fig. 4.24.

It is observable, that the modeled casting effects have almost no influence on the friction factor ratios. Test case V10-1s and V10-1s B show similar friction factor ratios throughout the investigated Reynolds number range. In another study conducted by Amro [3], rounded angled ribs with a dimensional rib height of $e/D_h = 0.1$ were investigated. The Reynolds number was varied from 30,000 to 200,000. The author reported a decrease of the friction factor ratio by 33 % in the case of a rounded rib compared to the sharp edge test case. This is in contrast to the results found in this study. As an explanation, it could be possible, that for smaller ribs, as discussed in this study, the effect of the rib's cross section shape becomes negligible and that only the overall rib height is important.

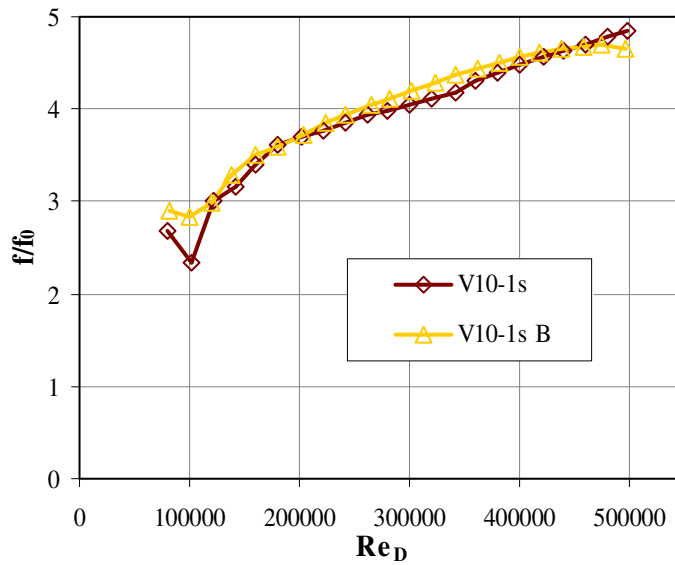


Fig. 4.24: Friction factor ratios f/f_0 of test cases V10-1s and V10-1s B

Heat transfer enhancement

The local distribution of the measured heat transfer ratios of test cases V10-1s and V10-1s R are presented in Fig. 4.25.

As can be seen, the overall heat transfer distribution is similar between the two test cases. The measured values close to the smooth channel side wall show nearly equal values, whereas in the region behind the rib tip, slightly higher heat transfer enhancements are noticeable in the case of the modified rib. Nevertheless, the differences between the two test cases are small.

The observed findings are also present in Fig. 4.26. Here, the area-averaged Nusselt number ratios of the two test cases are given. The values are in good agreement, especially for Reynolds numbers below 300,000. In the case of V10-1s, the heat transfer augmentation tends to decrease slightly with an increasing Reynolds number, whereas the values for test case V10-1s B show a minor increasing trend. Up to this point, all investigated heat transfer enhancement ratios reveal a more or less constant behavior in the higher Reynolds number range. The influence of the rib's cross section on the heat transfer augmentation is, therefore, considered to be minor. It appears that the rib height is the defining parameter on the level of heat transfer enhancement. Similar findings were also reported by Amro [3].

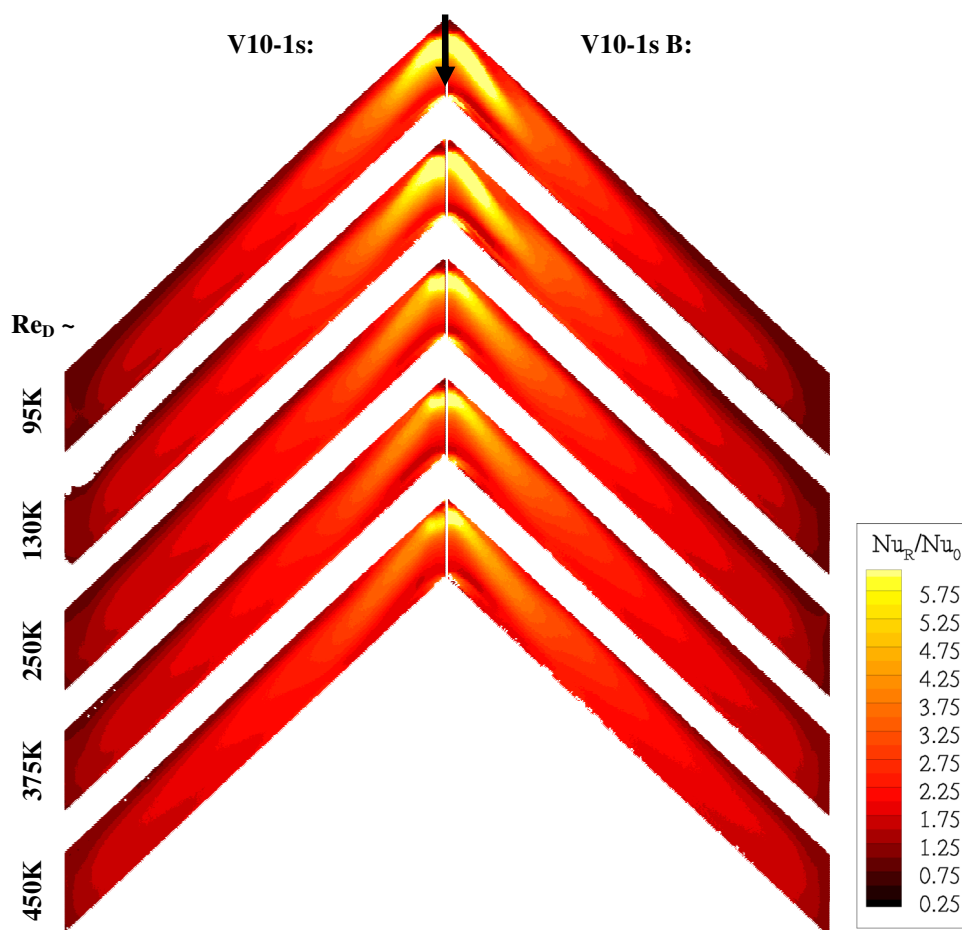


Fig. 4.25: Experimental local heat transfer ratios of test cases V10-1s and V10-1s B

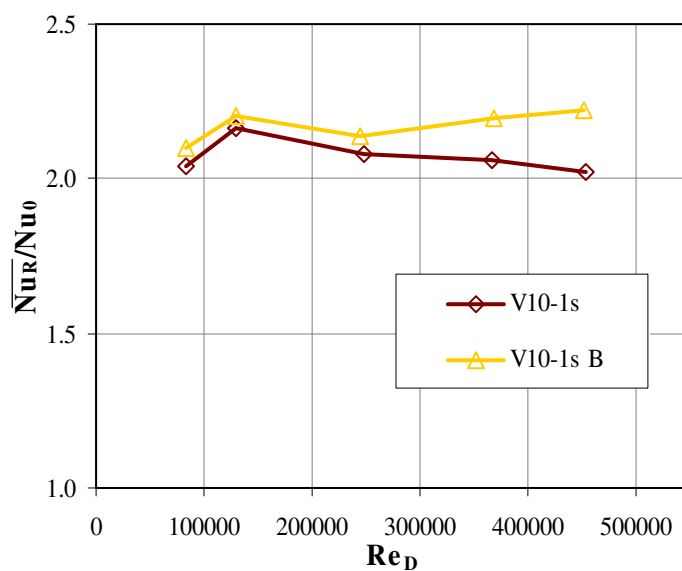


Fig. 4.26: Area-averaged Nusselt number ratio of test case V10-1s and V10-1s B

4.4 W-shaped ribs (transient measurement technique)

In the previous section, V-shaped ribs have been investigated with a variation of rib height and rib spacing. The results show, that the heat transfer augmentation in the region close to the symmetry plane is good, whereas the surface area close to the smooth channel side walls reveals a region of relatively low heat transfer enhancement. A further development to increase the area-averaged heat transfer enhancement and to homogenize the local heat transfer distribution is undertaken. To do so, the rib geometry is changed from V-shaped ribs to W-shaped ribs.

As mentioned in the introduction, there have been very few studies, dealing with W-shaped ribs implemented in convective cooling channels. Wright et al. [59] reported in their study, that using W-shaped ribs instead of V-shaped ribs increases both, the heat transfer augmentation and the pressure losses. The Reynolds number range varied from 10,000 to 40,000, the dimensionless rib height was kept at $e/D_h = 0.078$ and the rib pitch-to-height ratio was fixed at $P/e = 10$ in their study.

No experimental data was available for W-shaped ribs, which could be applied for backside cooled combustor walls. Furthermore, the effect of reducing the rib pitch-to-height has not been reported for W-shaped ribs. It is the scope of this section to investigate these effects on heat transfer augmentation and pressure losses. The parameters of the investigated configurations are presented in Table 4.4.

Table 4.4: Test case configuration W-shaped ribs

Test Case	Rib Type	P/e	e/D_h	Rib angle of attack	No. of Ribbed Walls
W10-1s	W-shaped	10	0.02	45°	1
W5-1s	W-shaped	5	0.02	45°	1



Fig. 4.27: Images of test cases W10-1s and W5-1s

The ribbed channel length-to-hydraulic diameter (l/D_h) is 5 for test cases W10-1s and 2.5 for test cases W5-1s. To realize nearly periodic flow conditions, a minimum of fifteen ribs are placed in front of the measurement region. Images of test case W10-1s and W5-1s are presented in Fig. 4.27.

For the numerical computation, the grids and number of nodes for test cases W10-1s and W5-1s are presented in Fig. 4.28. The total number of nodes is comparable to the quantities used for the V-shaped geometries. Again, the requirement of a dimensionless wall distance around $y^+ \approx 1$ is satisfied. For the thermal boundary condition, the isothermal boundary condition is applied.

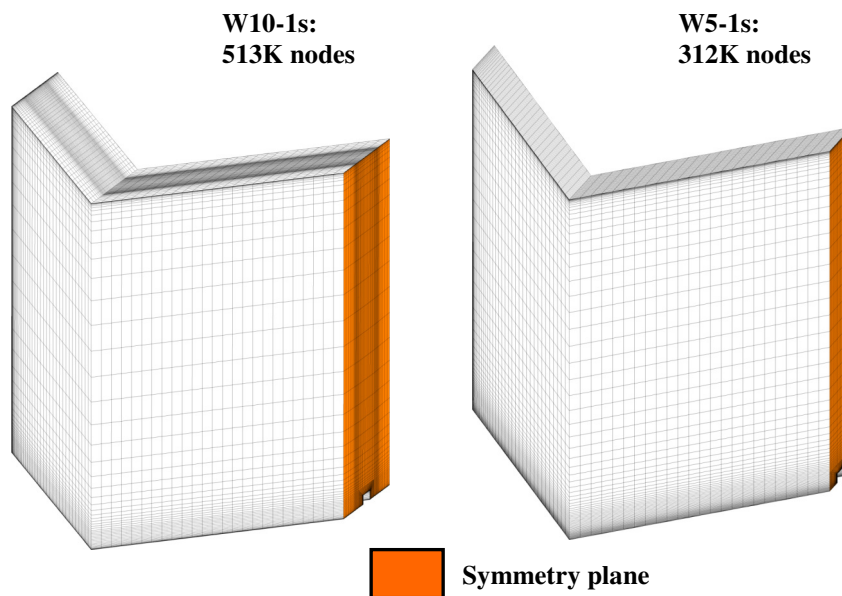


Fig. 4.28: Grids and number of nodes for test cases W10-1s and W5-1s

Velocity field

As in the previous investigations, the discussion of the effect on heat transfer enhancement and pressure losses of W-shaped ribs starts with a look on the velocity field. In Fig. 4.29 the computational mean velocity profiles of test cases W10-1s and W5-1s are presented.

Several differences can be observed, comparing them with the mean velocity profiles of the V-shaped rib geometry. Due to the W-shaped rib geometry, a total of four vortices are formed as documented by the stream traces in Fig. 4.29. Two counter rotating vortices are located in each channel half respectively.

Another important fact to highlight is that the region of maximum velocity has shifted towards the ribbed channel wall compared to the flow field situation of the investigated V-shaped ribs. This certainly increases the velocity gradient close to the ribbed wall, which should lead to a higher level of turbulence and therefore increase the overall heat transfer enhancement. The region of maximum velocity is closest to the ribbed wall in

the vicinity of the rib tip. This indicates a strong acceleration of parts of the main mass flow into the space between two successive ribs. Differences in the mean velocity profiles of test case W10-1s and W5-1s could not be observed.

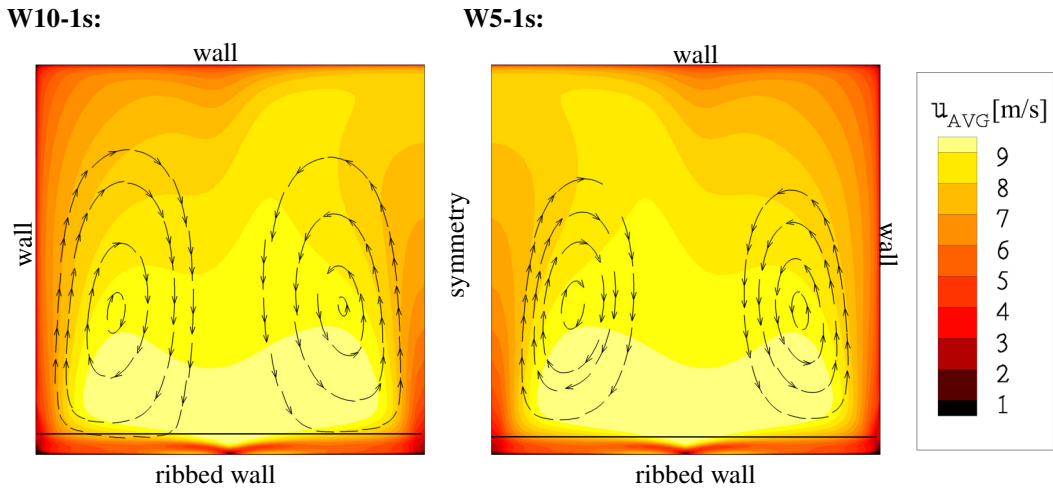


Fig. 4.29: Computational mean velocity profiles of test cases W10-1s and W5-1s at $Re_D \sim 130K$

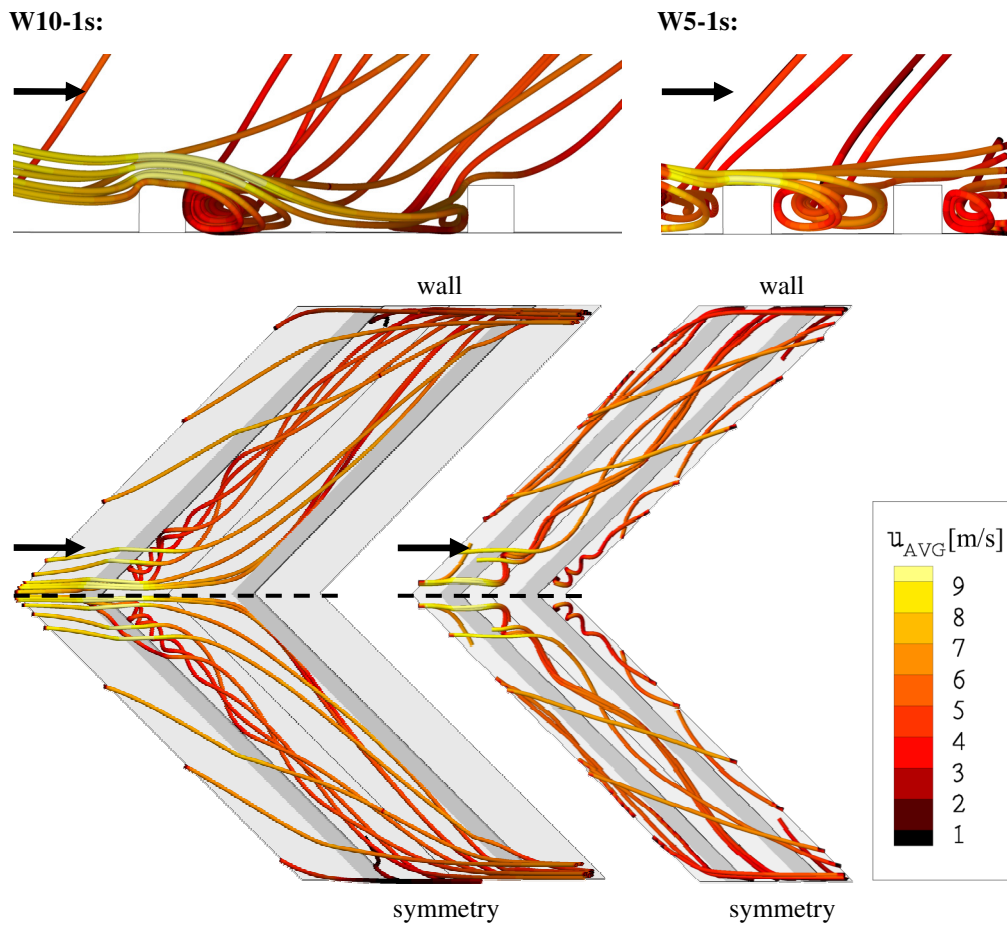


Fig. 4.30: Flow situation of test cases W10-1s and W5-1s close to the ribbed wall at $Re_D \sim 130K$

An examination of the flow field situation of test case W10-1s and W5-1s close to the ribbed wall is presented in Fig. 4.30. The general alignment of the stream traces is similar compared to the flow field of test cases V10-1s and V5-1s. For both test cases the advancing stream traces detach once the rib is passed. Behind every rib leg a vortex is created in the region of the developed recirculation zone. Again, stream traces from above the rib tip area are accelerated into the space between two successive ribs and the mass flow is transported towards the symmetry plane or the smooth channel side wall. Here, the mass flow is ejected into the main air flow. For the higher rib pitch-to-height ratio, a reattachment of the stream traces is observed, whereas for the closer rib distance the vortex fills out the complete space between two successive ribs.

A main result of changing the rib geometry from V-shaped to W-shaped ribs is that the length of the stream traces, which travel through the area between two successive ribs, is much shorter for the W-shaped rib geometry. For a situation, where a core flow is used to cool a surface, which is typically the case for a backside cooled combustor wall, this can be superior in terms of heat transfer augmentation. The driving local temperature difference between air flow and the wall between two successive ribs is reduced for V-shaped ribs compared to W-shaped ribs. Therefore, the overall heat transfer augmentation should increase, assuming that the mass flow is comparable between the investigated V-shaped and W-shaped rib geometries.

Friction factor

After discussing the influence of changing the rib geometry from V-shaped ribs to W-shaped ribs on the flow field, the effect on the friction factor ratios is investigated and the numerically and experimentally obtained data is presented in Fig. 4.31.

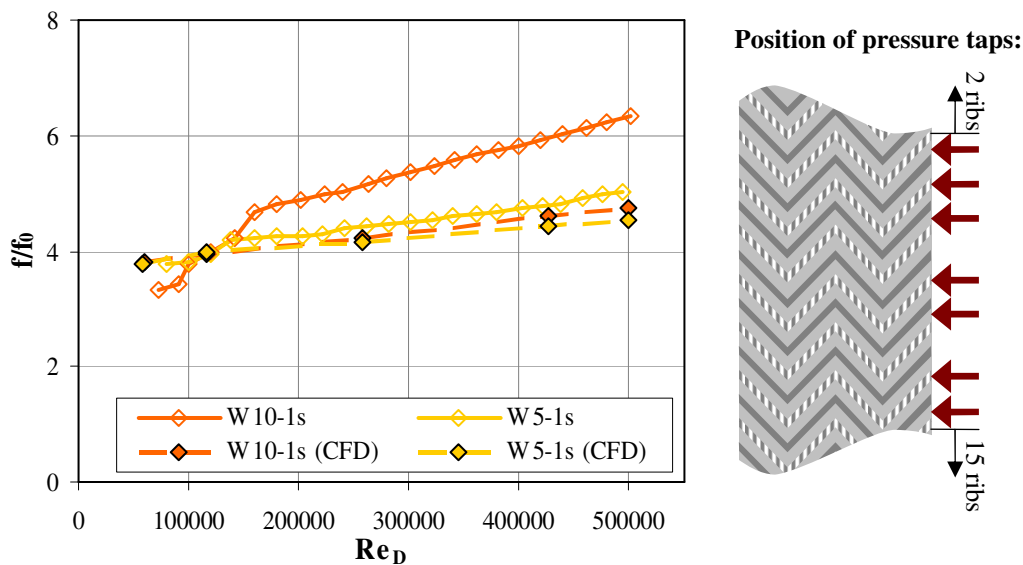


Fig. 4.31: Friction factor ratios f/f_0 of test cases W10-1s and W5-1s

For the experimental data it is noticeable, that changing the rib geometry from V-shaped ribs to W-shaped ribs is increasing the friction factor ratio. Comparing the friction factor ratios presented in Fig. 4.18 and Fig. 4.31, the friction factor ratios between the test cases V10-1s and W10-1s rises by approximately 35 % in the case of higher Reynolds numbers. Similar findings are made, comparing test case V5-1s and W5-1s.

As before, the numerical computations are not able to make precise estimations of the experimental data, excluding test case W5-1s, for which a satisfying agreement is observed. However, the general trend of a higher friction factor ratio in the case of an increased rib pitch-to-height ratio is captured. Also the computational results of test cases with W-shaped ribs show a higher friction factor ratio compared to the results of V-shaped ribbed channels. The computed results predict a friction factor increase of around 65 % for higher Reynolds numbers. This is higher than the above mentioned friction factor increase of around 35 % for the experimental data.

Heat transfer enhancement

The experimental local heat transfer ratios of test cases W10-1s and W5-1s are presented in Fig. 4.32.

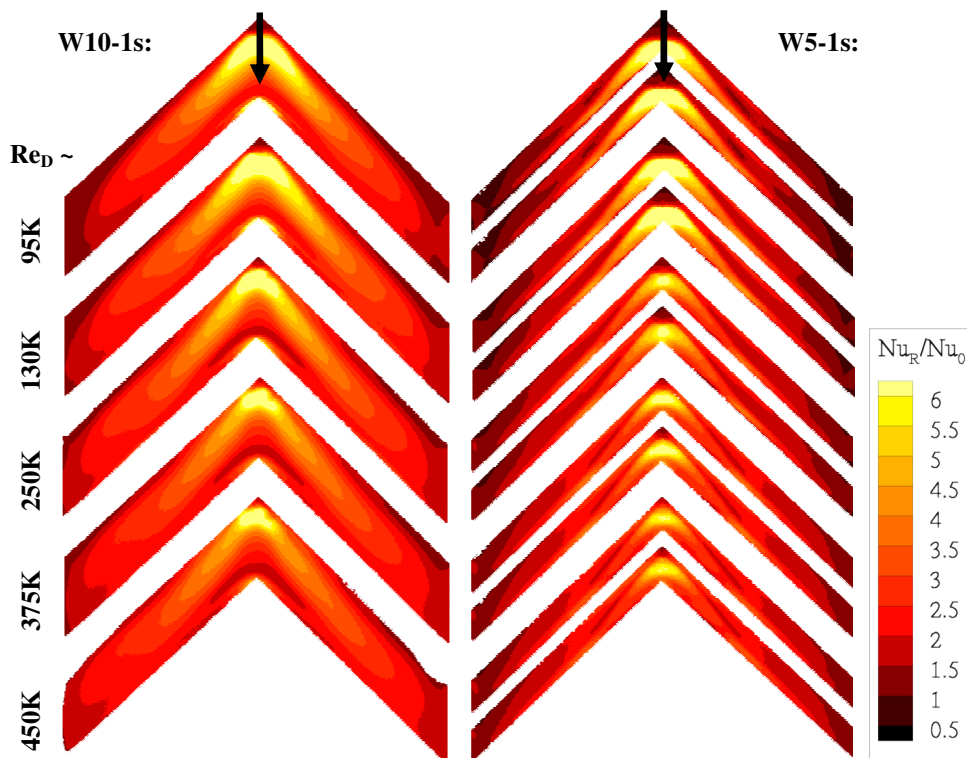


Fig. 4.32: Experimental local heat transfer ratios of test cases W10-1s and W5-1s

As can be seen, the heat transfer augmentation close to the smooth channel wall is higher compared to the corresponding test cases with V-shaped ribs. The heat transfer augmentation of test case W10-1s shows sufficient cooling close to the smooth channel

walls, whereas for test case W5-1s the level of heat transfer enhancement still reveals a potential for improvement. The local heat transfer distribution around the rib tip is very similar compared to the V-shaped rib geometry. This observation is in line with earlier remarks, which have been described during the discussion of the velocity field. Reducing the length of the stream traces between two successive ribs improves the local heat transfer situation. In the case of a W-shaped ribbed channel, the residence time of coolant mass flow between two successive ribs is lower compared to test cases with V-shaped ribs.

The maximum heat transfer augmentation peak is again located right behind the rib tip. Its level is reduced with an increasing Reynolds number.

For the global assessment of the heat transfer enhancement, the area-averaged Nusselt number ratios are presented in Fig. 4.33. Looking at the experimentally obtained data, it is apparent, that test case W10-1s shows the highest level of heat transfer augmentation. Compared to the corresponding test case V10-1s the level of heat transfer is increased by approximately 28 %.

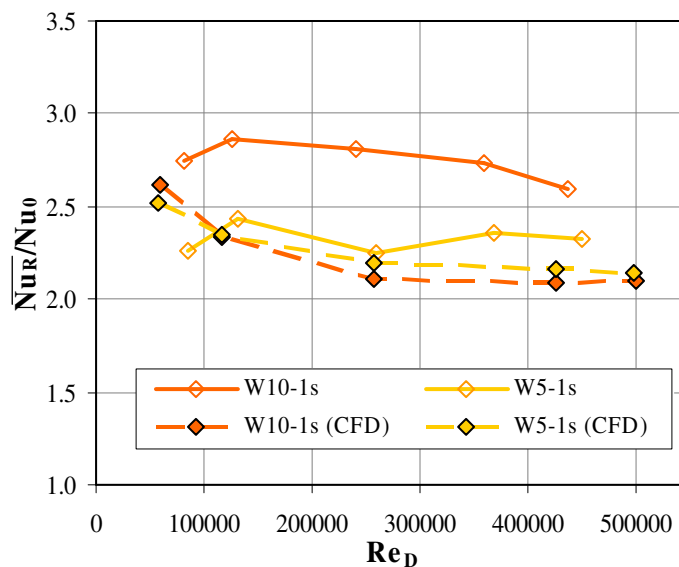


Fig. 4.33: Area-averaged Nusselt number ratio of test cases W10-1s and W5-1s

The numerically obtained data reveals an adequate agreement for test case W5-1s, whereas the experimental heat transfer data of test case W10-1s are underpredicted.

The computed increase of heat transfer augmentation between W-shaped and V-shaped ribbed channels is between 30 % for test cases W10-1s and V10-1s and 43 % for test cases W5-1s and V5-1s. Even though the precise values of the area-averaged Nusselt number ratios could not be computed, the level of heat transfer increase between W-shaped and V-shaped ribs is captured in the numerical computations.

4.5 W-shaped ribs (lumped heat-capacitance technique)

As reported in the previous chapter, test case W10-1s provides the highest level of heat transfer enhancement on the surface between two successive ribs. Reducing the dimensionless rib-to-pitch ratio P/e as done for test case W5-1s lowers the level of heat transfer enhancement compared with test case W10-1s. Additionally, the friction factor ratio is reduced. On the other hand, the additional surface area, due to the surface of the rib itself, is much higher in test case W5-1s.

The surface area increases due to the additional rib surface and the average heat transfer coefficient for the rib segments have to be considered for a comprehensive assessment of the overall cooling ability. Therefore, the average heat transfer coefficient is experimentally and numerically determined for these two test case configurations. For the experimental investigation the so-called lumped heat-capacitance technique (description is given in section 2.7) is applied. Images of the two test cases are presented in Fig. 4.34.

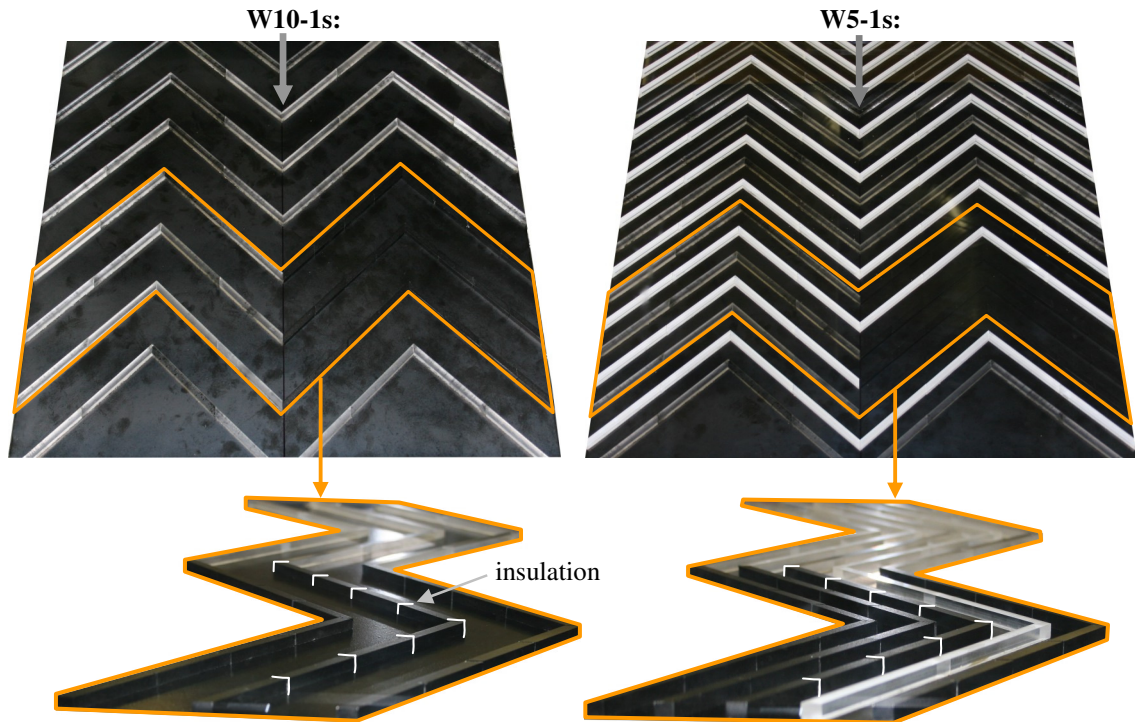


Fig. 4.34: Images of test cases W10-1s and W5-1s for the lumped heat-capacitance technique

As seen from these pictures, three successive ribs, which are normally made of Plexiglas, are substituted by ribs made of aluminum. The aluminum ribs are then coated with black paint and TLCs. To obtain a segment wise distribution of the average heat transfer coefficients on the rib surfaces, the rib is made of a total of eight pieces. The locations of the insulation between the several aluminum rib pieces are exemplarily marked for the center rib at the side view of the two test cases.

Heat transfer enhancement

The segment wise distribution of the experimentally obtained heat transfer enhancement data for test case W10-1s is presented in Fig. 4.35. A total of four different Reynolds numbers are investigated to capture possible Reynolds number effects on the heat transfer enhancement data. The Reynolds numbers are also selected to match the Reynolds numbers of the corresponding experiments, where the heat transfer enhancement on the area between two successive ribs was obtained using the transient liquid crystal method.

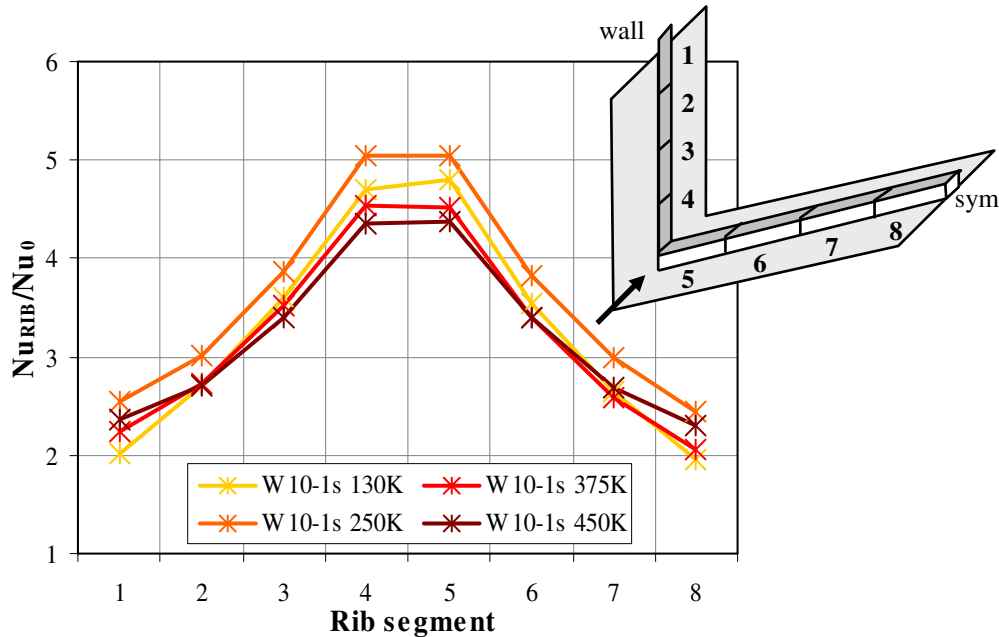


Fig. 4.35: Heat transfer enhancement on rib segments of test case W10-1s for $Re_D \sim 130K, 250K, 375K$ and $450K$

As can be seen, the highest heat transfer augmentation is observed for rib segments four and five, which are located at the rib tip. From this position, the heat transfer enhancement decreases towards the symmetry plane and towards the smooth channel side wall. Overall, the segment wise heat transfer enhancement shows a symmetric distribution. The level of heat transfer enhancement close to the symmetry plane is similar to the results found for the rib segment close to the smooth channel side wall.

Looking at the variation of the Reynolds number, no general trend can be observed. The highest heat transfer enhancement levels are detected for a Reynolds number of $Re_D \sim 250K$. For higher Reynolds numbers, the heat transfer enhancement seems to be slightly lower. Overall, the differences of the heat transfer enhancement due to a variation of the Reynolds number are small and within the experimental uncertainty (see Appendix B).

For test case W5-1s, the segment wise heat transfer enhancement is presented in Fig. 4.36. As before, the highest heat transfer enhancement is reported for rib segments four and five close to the rib tip. Again, the segment wise distribution reveals a symmetric

behavior. Compared to test case W10-1s, the respective rib segments show similar levels of heat transfer enhancement, besides rib segment one and eight, for which a lower heat transfer enhancement is obtained. For different Reynolds numbers, the heat transfer enhancement level is similar, except for a Reynolds number of $Re_D \sim 450K$. In this case, the heat transfer enhancement is lower. This is also observed for test case W10-1s, where the heat transfer enhancement is reported to be lower for the highest Reynolds number.

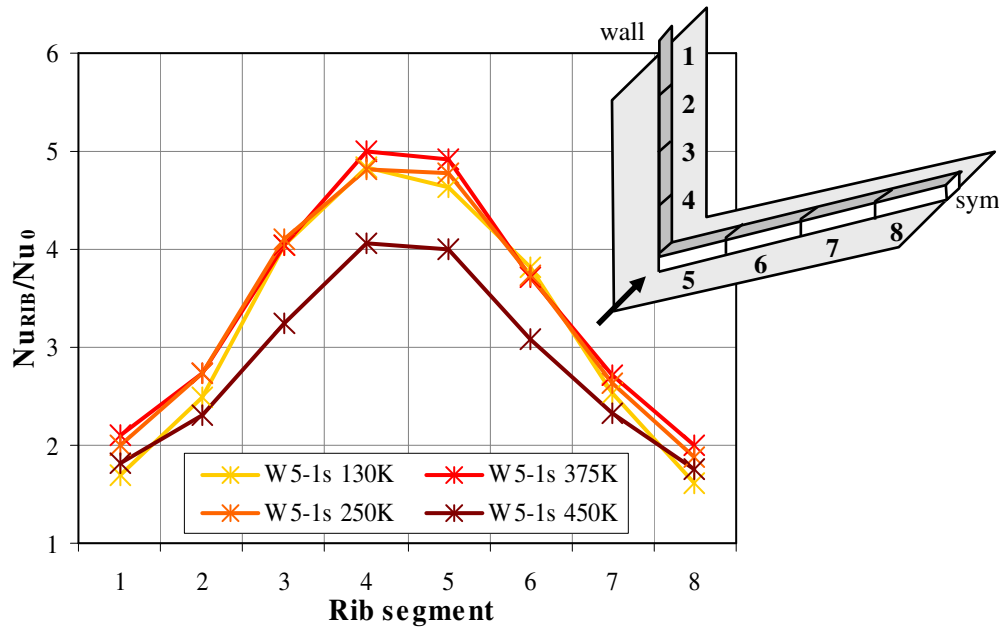


Fig. 4.36: Heat transfer enhancement on rib segments of test case W5-1s for $Re_D \sim 130K, 250K, 375K$ and $450K$

The area-averaged Nusselt number ratios of the combined eight rib segments are presented in Fig. 4.37 for test cases W10-1s and W5-1s. Looking at the experimentally obtained results, it is noticeable that for both test cases and nearly all investigated Reynolds numbers the area-averaged heat transfer enhancement on the rib itself is reported to be around 3.3 times higher than for a smooth channel wall. Due to the lower heat transfer enhancement levels for rib segments one and eight for a Reynolds number of $Re_D \sim 450K$, the area-averaged Nusselt number ratios for this Reynolds number is reduced compared to the data obtained for lower Reynolds numbers. For this reason, the lowest heat transfer enhancement of around 2.8 is reported for test case W5-1s and a Reynolds number of $Re_D \sim 450K$.

The numerically obtained data shows a decreasing trend of the heat transfer enhancement for an increasing Reynolds number, whereas in the experiment the level of heat transfer enhancement is more or less similar for Reynolds numbers below $Re_D \sim 400K$. Beyond this Reynolds number the experimentally obtained level of heat transfer enhancement seems also to decrease. The overall values are in good agreement for a Reynolds number of $Re_D \sim 130K$, but for higher Reynolds number the heat transfer enhancement is underpredicted.

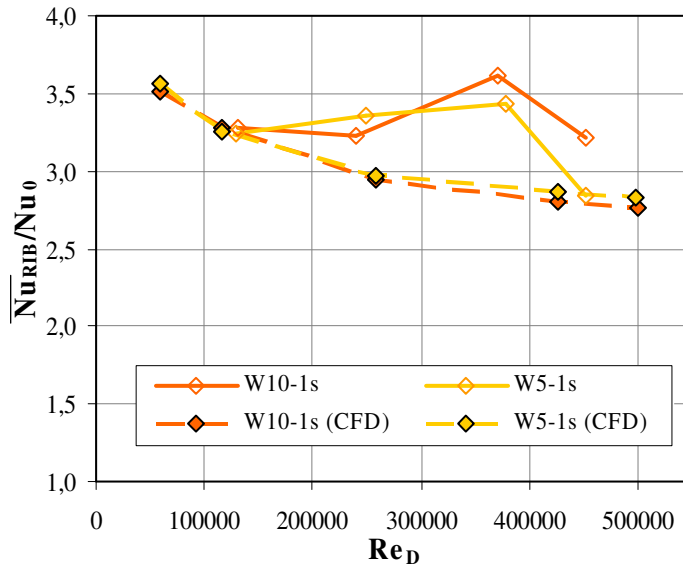


Fig. 4.37: Area-averaged Nusselt number ratio on rib segments for test cases W10-1s and W5-1s

Compared to the level of heat transfer enhancement on the smooth surface between two successive ribs, the respective area-averaged Nusselt number ratio on the rib shows higher values. The combined heat transfer enhancement of the rib segments (see equation (2.7) in chapter 2.7) and the surface between two successive ribs is presented in Fig. 4.38.

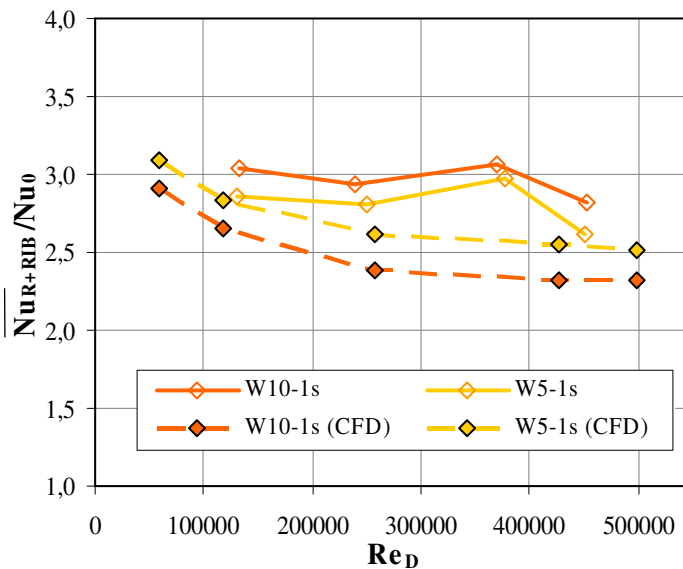


Fig. 4.38: Combined area-averaged Nusselt number ratio of rib segments and surface between two successive ribs of test cases W10-1s and W5-1s

The higher heat transfer enhancement on the rib itself and the additional surface area leads to higher overall heat transfer enhancement levels. For test case W10-1s, the experimentally obtained area-averaged Nusselt number ratio is reported to be around 3

times higher than for a smooth channel wall, compared to a heat transfer enhancement of 2.8 for the surface between two successive ribs only. In the case of denser rib spacing, as realized by test case W5-1s, the amount of additional surface area is higher than for test case W10-1s. Therefore the higher heat transfer enhancement on the rib has more impact on the combined area-averaged Nusselt number ratio. Here, the reported heat transfer enhancement level is around 2.8, if the heat transfer on the rib is included, which is higher compared to a value of 2.4, if only the surface area between to successive ribs is considered.

For the numerical computation the combined area-averaged Nusselt number ratios of test case W5-1s are reported to provide higher heat transfer enhancement levels compared to the results of test case W10-1s. This trend is not observed in the experiments. Here, test case W10-1s results in higher levels of heat transfer enhancement. Overall, the numerical computation tends to underpredict the experiment.

4.6 WW-shaped ribs (transient measurement technique)

For a further improvement of the area-averaged heat transfer augmentation the rib geometry is changed once more. Proceeding from W-shaped geometries, two additional rib tips are included, forming a so-called WW-shaped rib geometry. With this geometry an increased heat transfer augmentation is expected, due to the fact, that, up to this point, all test cases showed a high level of heat transfer enhancement close to the region behind the rib tip. The overall fraction of surface area, which shows a higher level of heat transfer enhancement, and hence the area-averaged heat transfer augmentation should therefore increase. In addition to this, the WW-shaped rib geometry should provide a reduced residence time of coolant mass flow in between two successive ribs compared to W-shaped ribbed channels. As stated before, a reduced residence time improves the overall heat transfer situation.

This rib geometry is investigated in combination with two different rib pitch-to-height ratios. The parameters of the two test cases are presented in Table 4.5.

Table 4.5: Test case configuration WW-shaped ribs

Test Case	Rib Type	P/e	e/D _h	Rib angle of attack	No. of Ribbed Walls
WW10-1s	WW-shaped	10	0.02	45°	1
WW5-1s	WW-shaped	5	0.02	45°	1

Images of test cases WW10-1s and WW5-1s are presented in Fig. 4.39. The ribbed channel length-to-hydraulic diameter (l/D_h) is 1.8 for test cases WW10-1s and WW5-1s. A minimum of seven ribs are placed in front of the measurement region, to provide nearly periodic flow conditions.

The grids used for the numerical investigations of test case WW10-1s and WW5-1s are presented in Fig. 4.40. As for the grids of the W-shaped rib geometry, the total number of nodes is comparable with the number of nodes used for the corresponding V-shaped geometry. The dimensionless wall distance is around $y^+ \approx 1$ and the isothermal boundary condition is applied for the thermal boundary condition.



Fig. 4.39: Images of test cases WW10-1s and WW5-1s

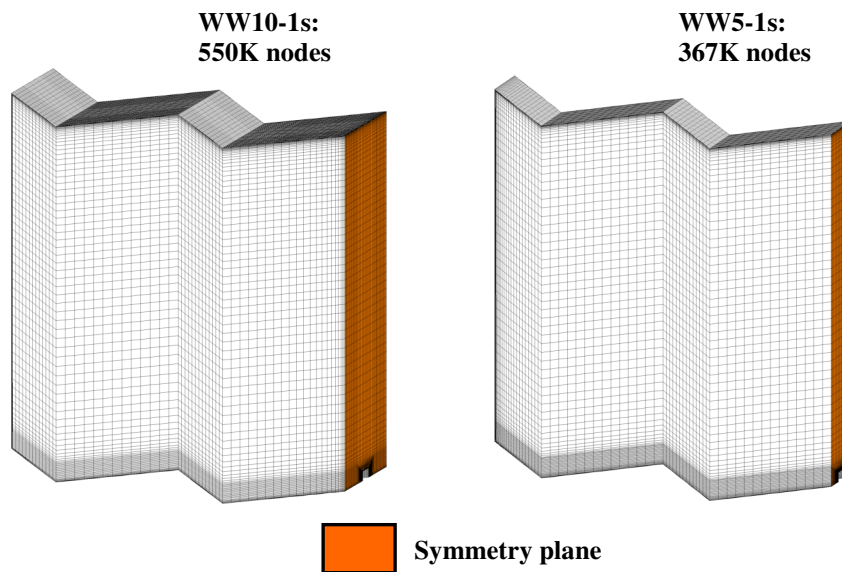


Fig. 4.40: Grids and number of nodes for test cases WW10-1s and WW5-1s

Velocity field

The computationally obtained mean velocity profile of test cases WW10-1s and WW5-1s are presented in Fig. 4.41.

In comparison to the test cases described above, the mean velocity profiles of the WW-shaped rib geometry have changed significantly. In the case of a V-shaped ribbed channel, only one vortex is located in each half of the channel cross section. The

maximum mean velocity is found in the mid-plane between ribbed wall and smooth wall. For the W-shaped geometry a total of two counter rotating vortices replace the single vortex as reported for the V-shaped geometry. The region of maximum mean velocity is shifted towards the ribbed wall, which was combined with a high acceleration of parts of the air flow into the region of two successive ribs.

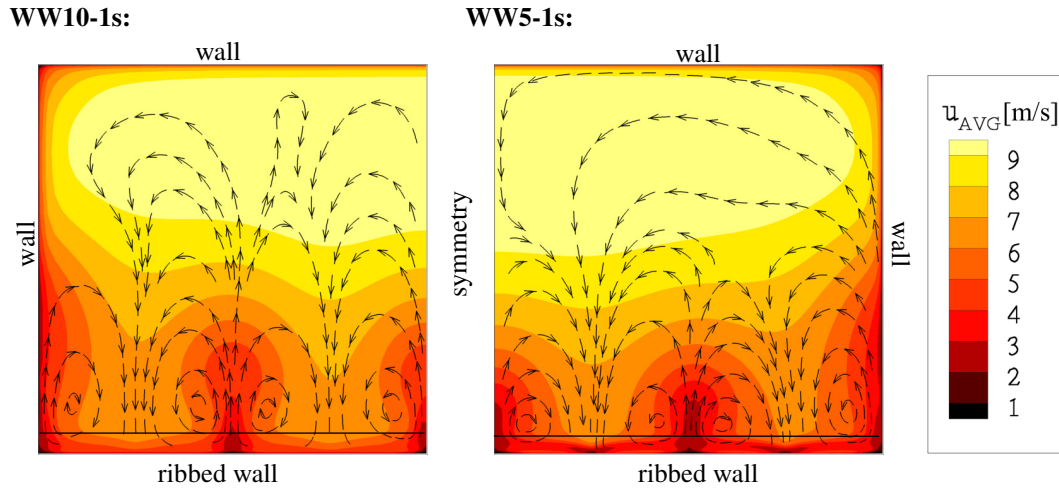


Fig. 4.41: Computational mean velocity profiles of test cases WW10-1s and WW5-1s at $Re_D \sim 130K$

Due to the additional rib tips of the WW-shaped geometry, a total of four counter rotating vortices are in each half of the channel cross section. While for the W-shaped geometry the center of the vortices is located close to the mid-plane between ribbed channel wall and smooth channel wall, in this case the center of the vortices have moved close the ribbed channel wall. This has the effect that the flow motion initiated by the secondary flow features do not manage to penetrate the main flow completely, resulting in a rather moderate velocity level close to the rib tip, where the air flow is sucked into the region between two successive ribs. As a direct consequence, the ejected air flow from the region between two successive ribs also has a low level of mean velocity.

Compared to the V-shaped and W-shaped ribs, the cells of the counter rotating vortices do not fill out the complete space between ribbed and smooth channel wall. The initiated secondary flow is not strong enough to form stable cells of counter rotating vortices. For test case WW10-1s the four cells can barely be observed, while for test case WW5-1s the ordered structure of the secondary flow field has vanished in the region close to the opposing smooth side wall.

For the two test cases the region of maximum mean velocity is now located close the smooth channel wall opposite of the ribbed channel wall, which agrees well with a mean velocity profile that could be typically observed in a channel with one roughened channel wall as presented earlier in Fig. 4.5.

To support the numerical computation, 2D-PIV measurements were conducted for test cases W10-1s and WW10-1s. The comparison between experimental and numerical

data provides confidence in the capability of the numerical procedure. The data is presented in Appendix A.

The effect of the altered mean velocity profile on the flow situation close to the ribbed channel wall is presented in Fig. 4.42. In general, the typical flow features as described for test cases with V-shaped and W-shaped are still observable. In the case of a higher rib pitch-to-height ratio a vortex directly behind the rib and a vortex before the rib do exist, whereas in the case of a reduced rib pitch-to-height ratio these two vortices collapse and only one vortex can be observed. The stream traces are diverted from the rib tip towards the trailing edge of the rib, where the fluid is ejected into the main flow. As a noticeable difference to the situation of the earlier test cases, the overall level of mean velocity is reduced. The swirling intensity of the vortices and the total amount of cooling air flow, which is diverted into the region between two successive ribs, is lowered.

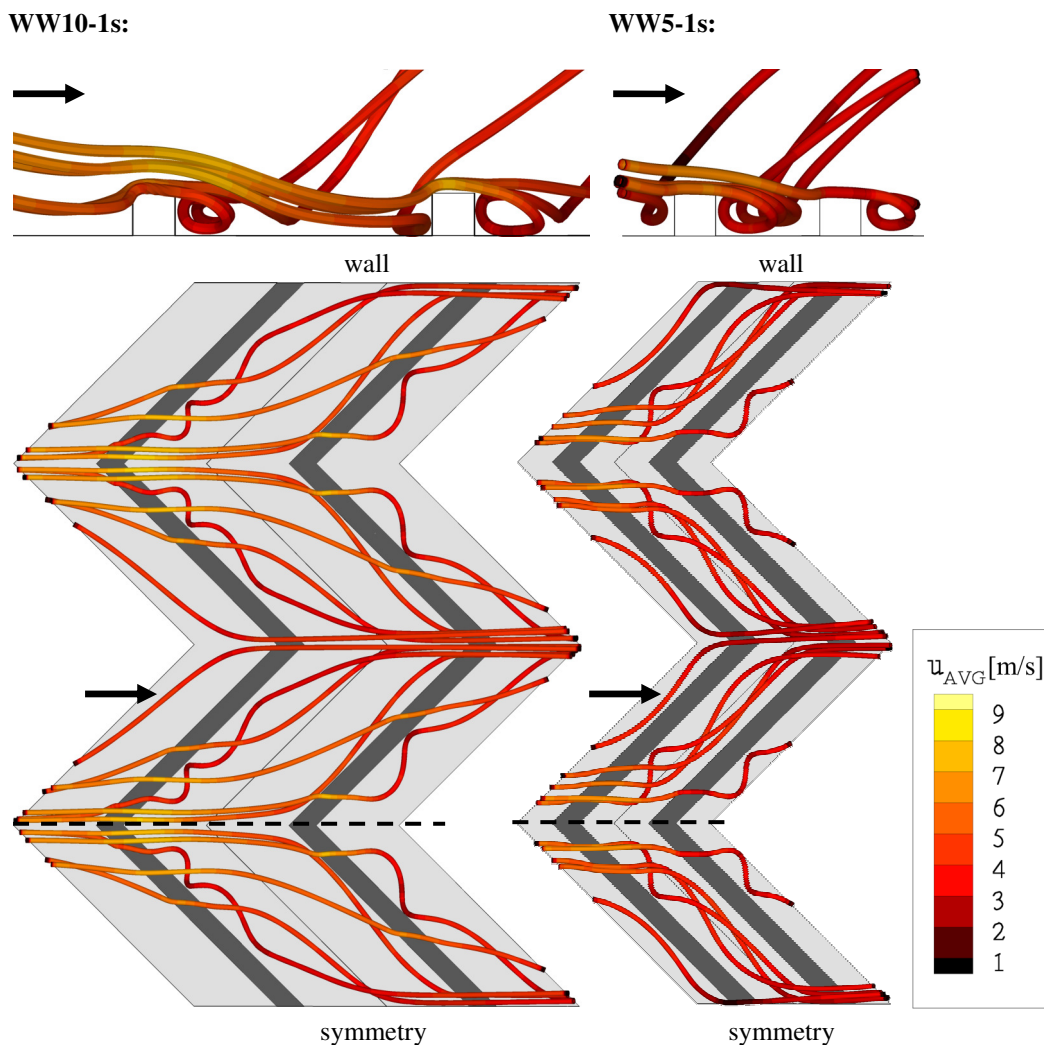


Fig. 4.42: Flow situation of test cases WW10-1s and WW5-1s close to the ribbed wall at $Re_D \sim 130K$

Friction factor

The significant change in the mean velocity profile is expected to be reflected in the results of the friction factor ratios. The friction factor ratios of test cases WW10-1s and WW5-1s are shown in Fig. 4.43. As seen from the data, the measured friction factor ratios are higher than for all other investigated test cases with a dimensionless rib height of $e/D_h = 0.02$.

Another interesting fact is that the previous trend of having a lower friction factor ratio with a reduced rib pitch-to-height is reversed. Now, the test case with the denser rib spacing provides the higher friction factor ratio. A possible explanation for this trend is found, if the WW-shaped rib geometry is treated as a homogeneously roughened channel wall. In this case, reducing the rib spacing leads to a higher number of flow turbulators and should, therefore, result in an increased pressure loss. Similar findings were reported by Nikuradse [49], who conducted experiments on channels equipped with homogeneously roughened channel walls.

The numerically computed data for test case WW5-1s shows at least for higher Reynolds numbers higher friction factor ratios compared to test case WW10-1s. Compared to the corresponding experimental data, the numerical computations predicts an approximately 40 % lower friction factor ratio for higher Reynolds numbers. Apart from this, the numerical computations manage to estimate in the mentioned Reynolds number region the offset of the friction factor ratios between the two test cases.

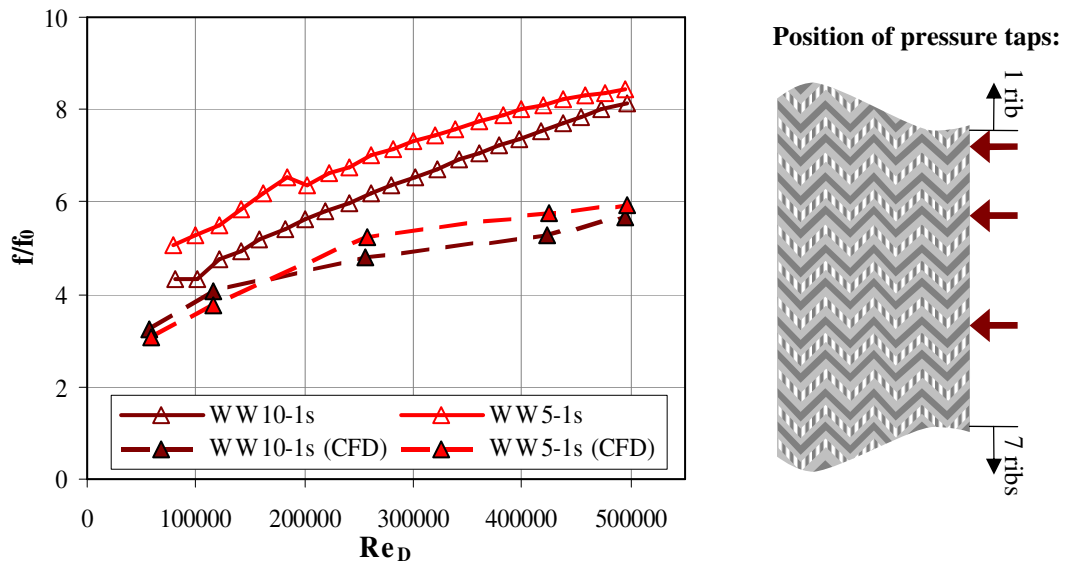


Fig. 4.43: Friction factor ratios f/f_0 of test cases WW10-1s and WW5-1s

Heat transfer enhancement

The experimental data of the local heat transfer ratios of test cases WW10-1s and WW5-1s is presented in Fig. 4.44. As proposed in the beginning of this section, behind

every rib tip a region of higher heat transfer enhancement is located. Like in the case of a W-shaped rib geometry with a rib-to-pitch ratio of $P/e = 10$, the local heat transfer distribution of the WW-shaped configuration is more uniform and also enhanced in the region close to the smooth side wall. This is in contrast to the local distribution of test cases build up on the V-shaped rib geometry. Whereas a region of lower heat transfer enhancement is noticeable for test case W5-1s, the situation for test case WW5-1s is improved. Here, the area, which reveals a lower heat transfer augmentation, is minimized.

As has been reported for all other test cases, the maximum peak of heat transfer augmentation is reduced in strength as the Reynolds number is increased. Compared to W-shaped ribbed channels the spatial expansion of the region with highest heat transfer enhancement is reduced. This is mainly due to the lower mean velocity close to the ribbed wall. Also the resulting lower swirling strength of the vortex behind the rib affects the level of the heat transfer enhancement peak.

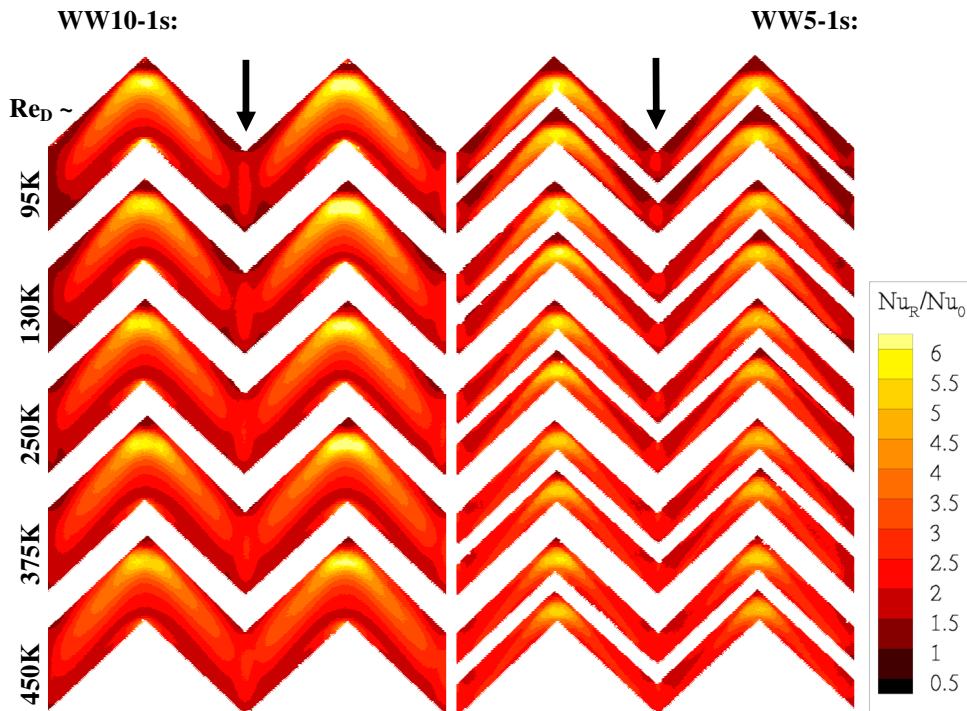


Fig. 4.44: Experimental local heat transfer ratios of test cases WW10-1s and WW5-1s

Looking at the area-averaged Nusselt number ratios of test cases WW10-1s and WW5-1s, as presented in Fig. 4.45, another trend reversal is noticeable. The ribbed channel with the lower rib pitch-to-height ratio provides the higher area-averaged Nusselt number ratio. As can be observed in the distribution of the local heat transfer ratios, there are fewer regions with lower heat transfer enhancement in the case of test case WW5-1s compared to test case WW10-1s.

As for all previous test cases the Nusselt number ratio remains nearly constant with increasing Reynolds numbers. The level of heat transfer augmentation is comparable to

the experimental results of test case WW10-1s. In contrast to test case WW5-1s, where an increase of the Nusselt number ratio is evident comparing the W-shaped and the WW-shaped geometry, WW10-1s shows no further improvement of the area-averaged heat transfer ratio.

The CFD results again predict lower values of the heat transfer augmentation, but the trend of having a higher area-averaged Nusselt number ratio in test case WW5-1s is captured above a Reynolds number of 200,000. In this Reynolds number range the quantitative offset between test cases WW10-1s and WW5-1s is reflected appropriately.

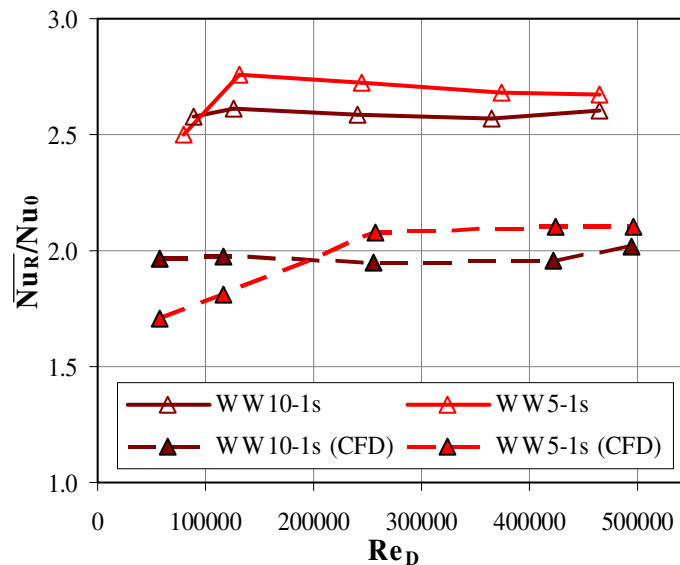


Fig. 4.45: Area-averaged Nusselt number ratio of test cases WW10-1s and WW5-1s

4.7 Conclusions on ribbed cooling channels

Experimental and numerical investigations are conducted on V-shaped, W-shaped and WW-shaped rib geometries. For the V-shaped geometry, two different rib heights and two different rib pitch-to-height ratios are studied. Furthermore the influence of having a one-sided or a two-sided ribbed channel is shown. The effect of casting imperfections is simulated with an additional test case. In the case of W-shaped and WW-shaped rib geometries, merely the impact of two different rib pitch-to-height ratios is investigated.

The results of the V-shaped geometries indicate that there is an amplification of the pressure penalty, if the number of ribbed walls is increased. In addition, the pressure penalty is enlarged, if the dimensionless rib height is raised. Looking at the heat transfer measurements, it is noticeable, that the introduction of a second ribbed wall is increasing the global and local heat transfer augmentation. Also the heat transfer enhancement peak is intensified in the case of a two-sided ribbed channel. These remarks reveal that investigations on convective cooling devices obtained in two-sided ribbed channels cannot be used directly in applications with one-sided ribbed channels.

This means that knowledge from the technical field of gas turbine blade cooling has to be used carefully in the design process of backside cooled combustor walls.

If the Reynolds number is increased, the heat transfer enhancement peak is reduced in intensity. For the area-averaged heat transfer enhancement, the level of heat transfer augmentation remains at a nearly constant level above a Reynolds number of 200,000 for all test cases.

Looking at the numerical computations, it could be demonstrated that typically industrial design approach is able to show the same trends as found in the experiments. For most test cases, the accuracy of the computational results is insufficient and the computations tend to underpredict the experimental data. The velocity fields seem reasonable and the expected flow features could be identified. Therefore it is appropriate to apply the numerical procedure for flow field visualization and preliminary parameter studies within the parameter range typically found at backside cooled combustor walls.

The reduction of the rib pitch-to-height from $P/e = 10$ to $P/e = 5$ has different effects on V-shaped, W-shaped and WW-shaped ribbed channels. In the case of V-shaped and W-shaped convective cooling features, a reduction of the rib pitch-to-height from $P/e = 10$ to 5 lowers pressure losses. For an increasing Reynolds number, there is a smaller rise of the friction factor ratio for test cases with smaller rib spacing. Together with a reduction of the friction factor ratio, the area-averaged heat transfer augmentation is lessened for test cases with a rib pitch-to-height of $P/e = 5$. Among the V-shaped and W-shaped configurations, test case W10-1s provides the highest level of heat transfer augmentation.

If the additional surface and the heat transfer on the rib is considered, the numerical computations indicate, that test case W5-1s reveals even higher levels of overall heat transfer enhancement compared to test case W10-1s. An experimental approach, using the so-called lumped-heat capacitance method, provides heat transfer data on the rib itself. The experimental data revealed that the heat transfer enhancement on the rib is approximately 3.3 times higher than for smooth channel. Including the heat transfer data and the additional surface area of the rib, a combined area-averaged Nusselt number ratio is obtained. In contrast to the numerically obtained data, test case W10-1s provides the highest level of heat transfer enhancement of around 3.0 and test case W5-1s offers a heat transfer enhancement of around 2.8.

For WW-shaped configurations, the overall situation is different. A significant change of the mean and secondary velocity fields has been observed. The region of maximum velocity is pushed towards the smooth channel wall opposite the ribbed wall. In the case of V-shaped and W-shaped ribbed channels the area of maximum velocity is located around the mid-plane between ribbed wall and smooth channel wall and close to the ribbed channel wall respectively. In contrast to the other test cases, the WW-shaped configuration provides a mean velocity profile as would be expected for a channel with one roughened channel wall.

Along with these observations, the secondary flow features of the WW-shaped configurations are more unstructured compared to the other rib geometries. This is observable most of all for test case WW5-1s, where the cells of counter rotating vortices do not fill the whole channel cross section. The mentioned changes of the mean velocity profile lead to an overall lower level of mean velocity close to the ribbed wall. Therefore, the amount of air flow, which is lead into the region between two successive ribs, is reduced compared to the other rib configurations. Test case WW5-1s provides the highest pressure losses of all test cases with a dimensionless rib height of $e/D_h = 0.02$. In contrast to the above described effect of reducing the rib pitch-to-height, reducing the rib spacing increases the friction factor ratios. The heat transfer augmentation is on a similar level as found for the W-shaped ribbed channels.

The investigations revealed no major differences between an idealized rib cross section and a configuration with modeled casting effects. It is concluded that the dimensionless rib height is the main parameter for small ribs.

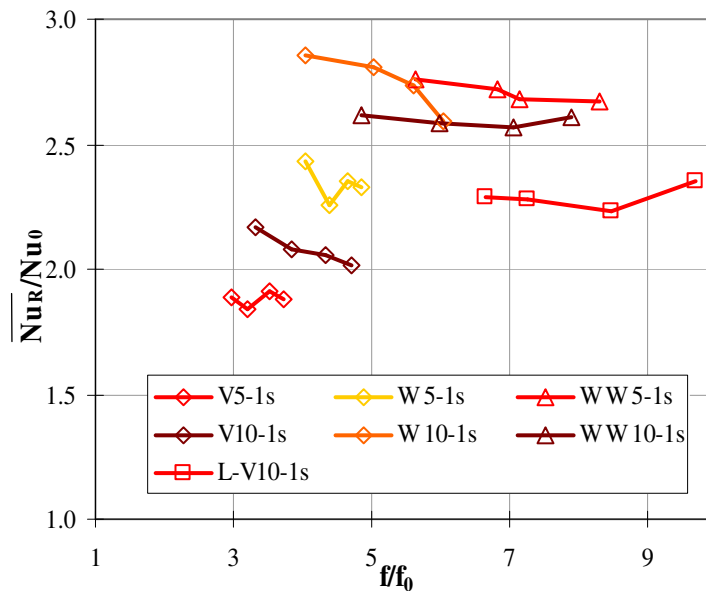


Fig. 4.46: Experimentally obtained heat transfer augmentation plotted over friction factor ratio for the presented ribbed test configurations

To summarize the conclusions for all test cases with ribs placed on one channel wall in one chart and to make the cooling ability of the different convective cooling approaches visible, the heat transfer enhancement as a function of the friction factor ratio is shown in Fig. 4.46.

It can be observed, that the highest levels of heat transfer augmentation are reached by two test cases, test case W10-1s and test case WW5-1s. With those configurations, it is possible to establish a heat transfer enhancement of around 2.75 compared to a smooth channel. The range of pressure penalty varies from $f/f_0 = 3$, as found for test case V5-1s, to $f/f_0 = 10$, which is observed for test case L-V10-1s.

Another common way to assess the cooling ability of the different test cases is the evaluation of the thermal performance parameter η as given in equation (4.1). The obtained results are presented in Fig. 4.47.

$$\eta = \left(\frac{\overline{Nu}_R}{Nu_0} \right) / \left(\frac{f}{f_0} \right)^{1/3} \quad (4.1)$$

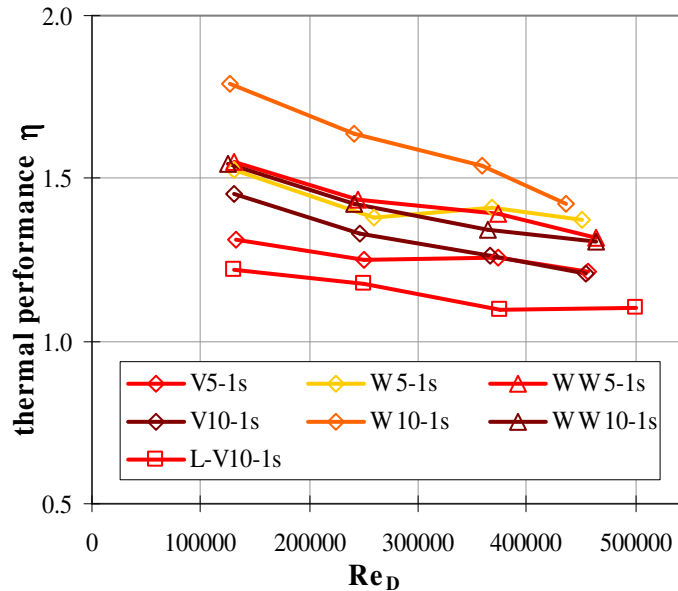


Fig. 4.47: Thermal performance η of experimentally investigated ribbed test cases

The best thermal performance is found for test case W10-1s. However, it has to be pointed out, that the offset to next best configuration is reduced for an increasing Reynolds number. However, all test cases with a dimensionless rib height of $e/D_h = 0.02$ perform better compared to a one-sided ribbed channel with higher ribs like test case L-V10-1s. For test cases W10-1s and W5-1s, the heat transfer data on the rib itself is also available. Therefore, the additional surface area and the heat transfer on the rib can be included into the assessment of the cooling performance. The thermal performance of the test cases with and without considering the heat transfer data on the rib itself is presented in Fig. 4.48. For both test cases, including the heat transfer data on the rib leads to an increased thermal performance. Due to the higher amount of additional surface area of test case W5-1s, where the rib spacing is denser, the increase in thermal performance is more intense. Overall, the thermal performance of the investigated W-shaped rib configurations is very similar, if the heat transfer data on the rib is considered. It depends on the demands of the combustor design, whether a somewhat lower pressure penalty or a higher heat transfer enhancement is preferred.

As mentioned in the introduction, the design of a backside cooled combustor wall has special demands. In some cases the overall pressure loss of the combustor component is the limiting parameter in other cases a minimum level of heat transfer enhancement must be achieved to realize a stable and proper convective cooling concept. Due to this,

it is not always possible to choose the rib configuration with the best thermal performance.

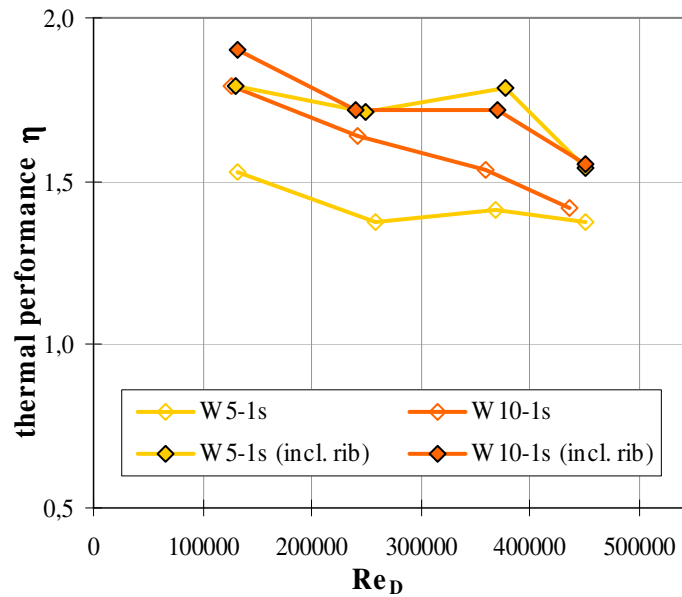


Fig. 4.48: Thermal performance η of experimentally investigated test cases for W-shaped ribs with and without considering the heat transfer data on the rib itself

To find possible candidates for further studies on ribbed channels, the pressure penalty increase based on test case V10-1s is presented in Fig. 4.49. With this figure the potential of changing the rib configuration from a kind of baseline rib configuration, which is test case V10-1s, to other test case configurations is revealed.

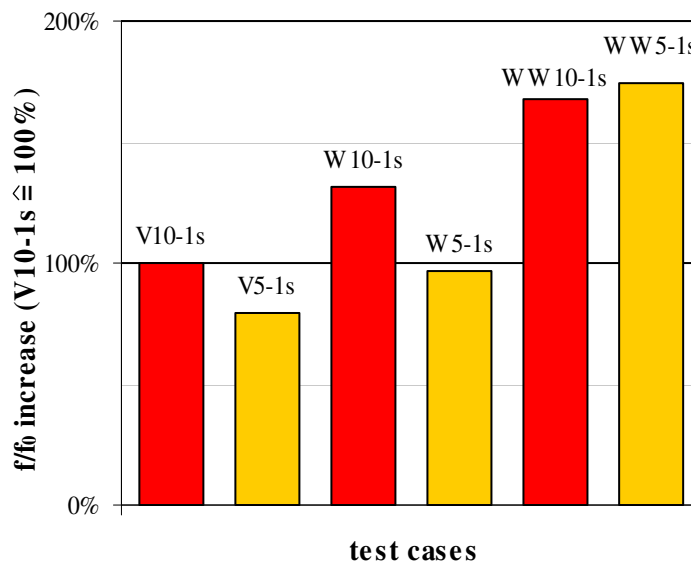


Fig. 4.49: f/f_0 increase based on test case V10-1s at $Re_D \sim 450K$

As seen from the figure, there is a nearly linear increase of the pressure penalty for test cases with a rib pitch-to-height ratio of $P/e = 10$. In the case of reduced rib spacing, the pressure penalty increase is disproportionately high proceeding from test case W5-1s to WW5-1s. Due to this trend, it is not recommended to conduct further investigations on e.g. WWW-shaped ribs for a channel with an aspect ratio of $AR = 2:1$. Compared to test case V10-1s, the friction factor ratio can be reduced by changing the rib configurations to the presented rib configurations of test cases V5-1s or W5-1s.

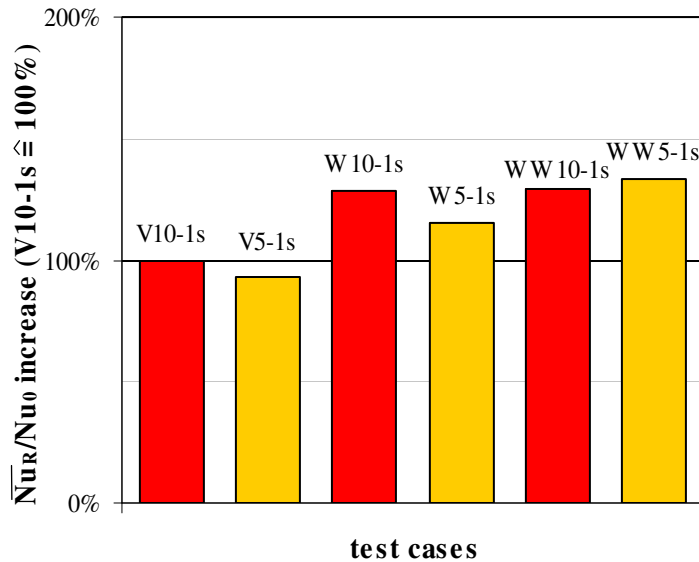


Fig. 4.50: Area-averaged Nusselt number ratio increase based on test case V10-1s at $Re_D \sim 450K$

In Fig. 4.50, the heat transfer augmentation increase is presented based on test case V10-1s. With all test cases, except for test case V5-1s, the level of heat transfer enhancement can be elevated. It is interesting to note, that there is a linear increase for test cases with smaller rib spacing, whereas the heat transfer augmentation could not be increased proceeding from test case W10-1s to test case WW10-1s.

From all discussed trends and results, test case W10-1s and test case W5-1s seem to provide an efficient cooling geometry for backside cooled combustor walls with an aspect ratio of 2:1 at high Reynolds numbers.

5 Dimples

As mentioned in the introduction, there have been various investigations on channels with dimpled surfaces. To date, the author is aware of only one study [33], which considers the typical conditions found in backside cooled combustor walls.

For the design aspect of backside cooled combustor walls, it is of interest to know, if a dimpled surface has superior or inferior cooling abilities compared to channels with ribbed surfaces.

The purpose of this chapter is to provide pressure loss and heat transfer data of a channel equipped with one dimpled surface. As a candidate, a configuration, which was investigated by Burgess et al. [9], is chosen and the Reynolds number range typical for combustor liner cooling is considered. In addition, the effect of reducing the channel height on the pressure losses and heat transfer augmentation is investigated.

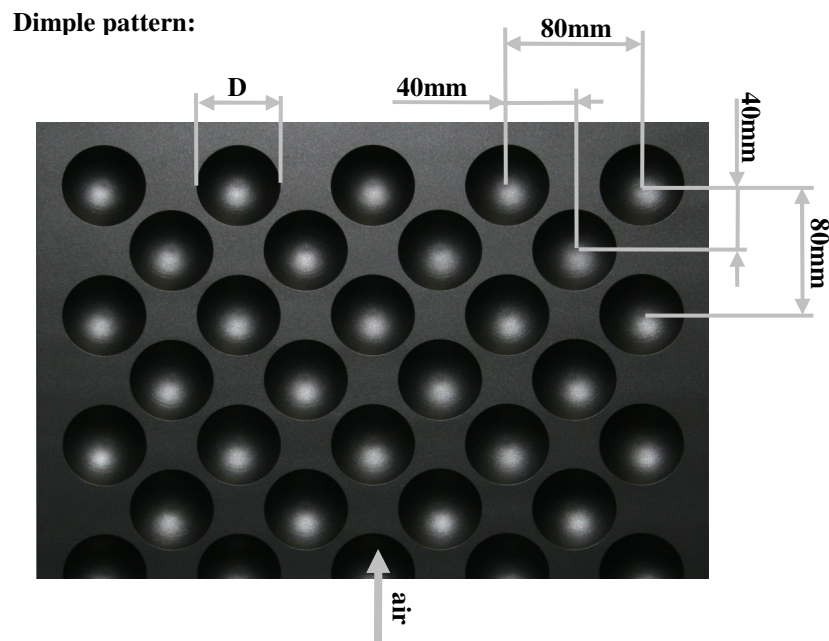


Fig. 5.1: Dimple pattern

5.1 Dimples with $H/D = 4$

In the first set of numerical and experimental studies of dimpled surfaces, the channel cross section was set to $400 \times 200 \text{ mm}^2$. With this configuration the mean velocity level within the investigated Reynolds number range and the dimensions of the channel cross section is similar to the test cases with ribs. The dimpled surface simply replaces the ribbed channel wall. The arrangement of the dimples and the dimensions of the dimple pattern are presented in Fig. 5.1. The parameters of test case Dimple HD4 are available

in Table 5.1. The dimpled channel length-to-hydraulic diameter (l/D_h) is 3 for test case Dimple HD4. A minimum of five periodic segments are located in front of the measurement region, to provide nearly periodic flow conditions.

Table 5.1: Test case configuration of test case Dimple HD4

Test Case	Aspect Ratio	H/D	δ/D	No. of Dimpled Walls
Dimple HD4	2:1	4	0.2	1

Numerical computations have been conducted together with experiments using the transient measurement technique. A periodic segment of the dimpled test section is isolated and a block-structured grid is created. The grid and the total number of nodes are presented in Fig. 5.2.

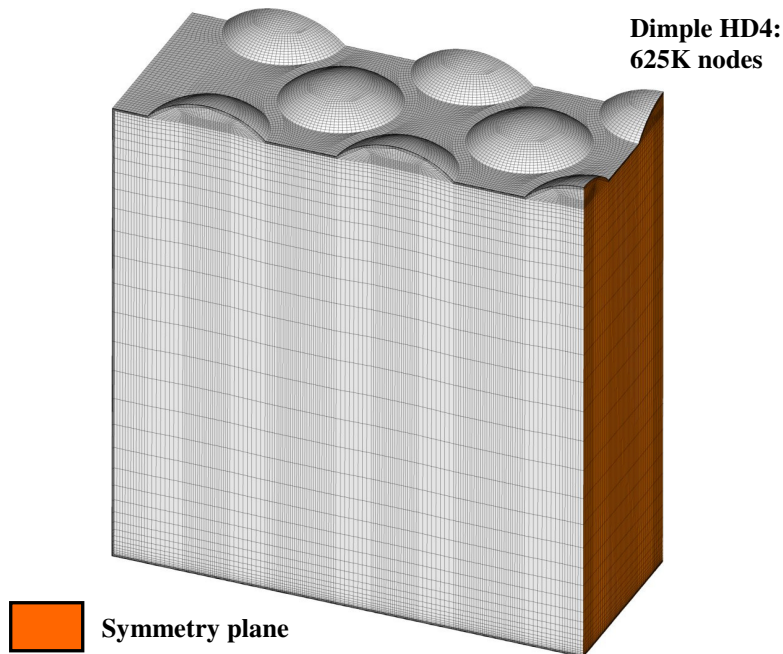


Fig. 5.2: Grid and number of nodes for test case Dimple HD4

A literature research indicated, the numerical prediction of the velocity field close to the dimpled channel wall is assumed to be more sensitive compared to the cases with ribs placed on one channel wall only. In addition, the anticipated vortices, which are one reason for heat transfer augmentation, are expected to be more complex and smaller in size. Therefore, the chosen turbulence model should be able to calculate these vortices accurately to allow a prediction of the velocity field and the resulting heat transfer enhancement. It is doubtful, whether the standard $k-\epsilon$ turbulence model is capable of dealing with such a flow type, due to the assumption of isotropic turbulence. Therefore, the numerical computations are also conducted using the Reynolds Stress Model (RSM) to account for the effects of anisotropy.

Velocity field

Within this section, the general flow structures of a channel with one dimpled channel wall at high Reynolds numbers are described. The flow characterization is commenced with the computational mean velocity profile of test case Dimple HD4 as presented in Fig. 5.3. Here, the general velocity distribution from the numerical computations of the standard k- ϵ and the RSM model are shown.

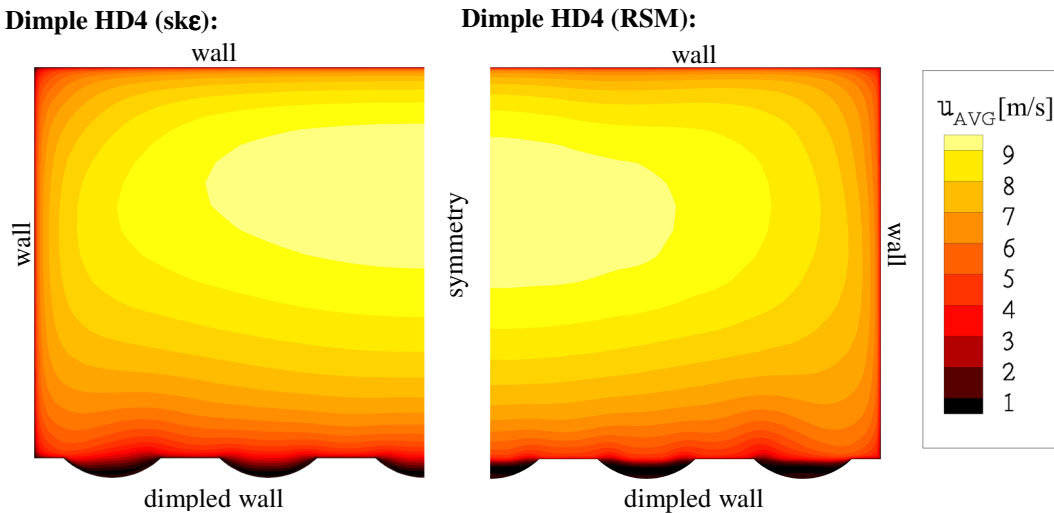


Fig. 5.3: Computational mean velocity profiles of test case Dimple HD4 at $Re_D \sim 130K$

As with the WW-shaped rib test cases, the maximum mean velocity is shifted towards the smooth channel wall opposite to the dimpled bottom wall. The mean velocity profile reminds the observer of a typical distribution found for a channel with one roughened channel wall. In this illustration, no significant differences between the two turbulence models can be identified. Both turbulence models predict a similar mean velocity profile.

Contour plots of the X-Vorticity slightly above and within the dimple are presented in Fig. 5.4. As stated in [19], this variable is a measure of rotation of a fluid element as it moves in the x-direction of the flow field. High positive values are a sign of clockwise fluid element rotation and high negative values indicate a counterclockwise rotation. Around the location of a X-Vorticity peak a vortex center can be assumed. Therefore, the contour plots of the X-Vorticity should provide a reasonable indication, whether the turbulence models are capable to predict small sized vortices.

Following the sequence of figures from top to bottom, the contour plots are moved through a dimple along the main flow direction. For both models, it can be observed that once the beginning of the dimple is reached higher levels of X-Vorticity are created. This is mainly due to the inflow into the dimple from regions next to the surface indentation.

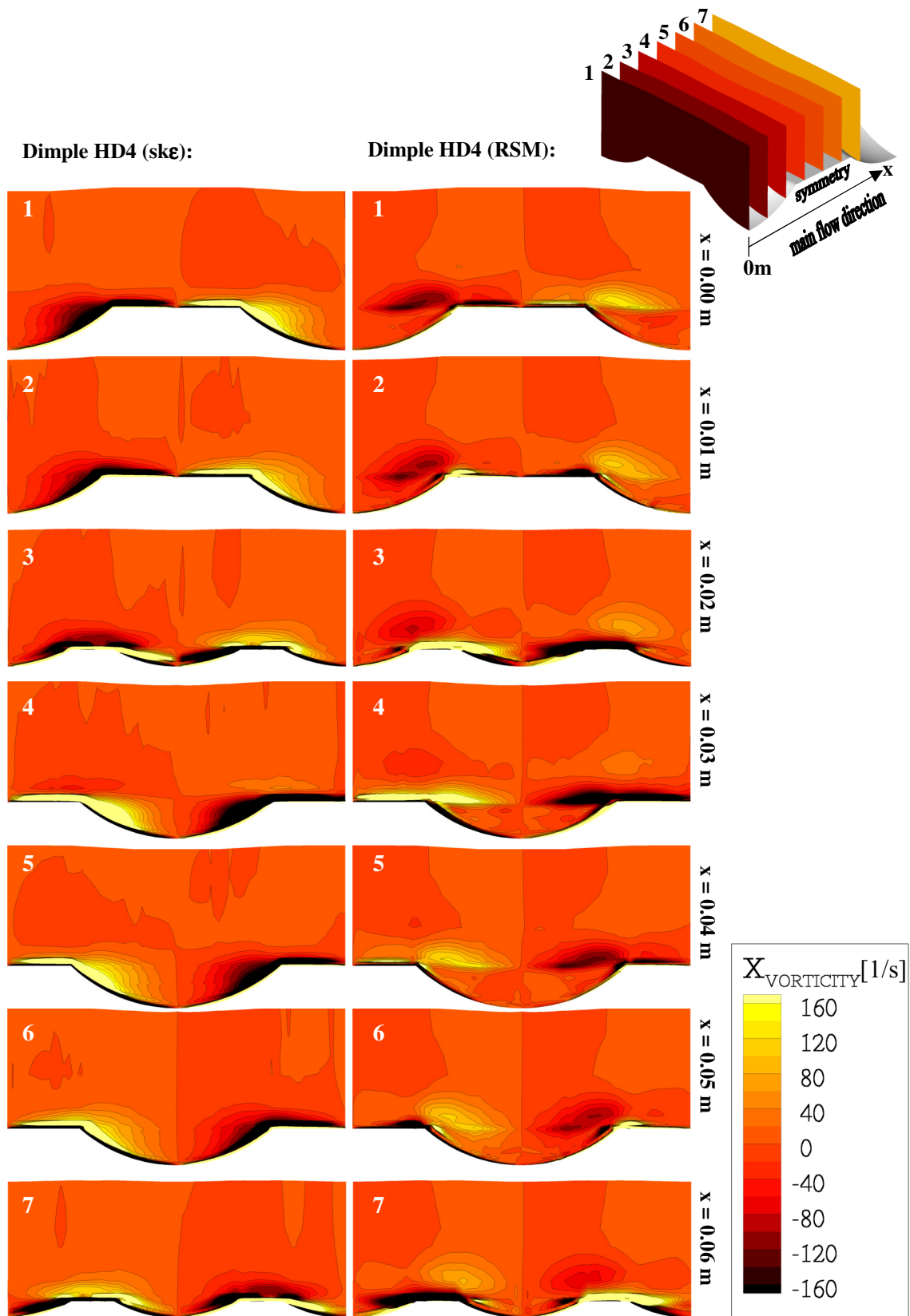


Fig. 5.4: X-Vorticity contour plots of test case Dimple HD4 at $Re_D \sim 130K$

In the case of using the standard k - ϵ turbulence model, the two separate regions of higher X-Vorticity remain attached to the surface. Once the dimple is passed, the region of higher X-Vorticity disappears. For all figures, no regions of higher X-Vorticity could be detected away from the dimpled surface. And as a consequence the discharge of vortices into the main air flow is not predicted by the $k\epsilon$ turbulence model.

Using the RSM turbulence model, a different situation is observed. The regions of higher X-Vorticity are separated from the dimple surface. Also, the rotation does not disappear completely as the rear part of the dimple is reached, even though the overall strength is significantly reduced. For a limited distance, the rotating cells are ejected out of the dimple and manage to enter the main air flow. Due to these observations, it is advantageous to use the RSM turbulence model for further discussions, because the prediction of vortex motion close to the dimpled surface seems to be similar to the situation described in literature [41].

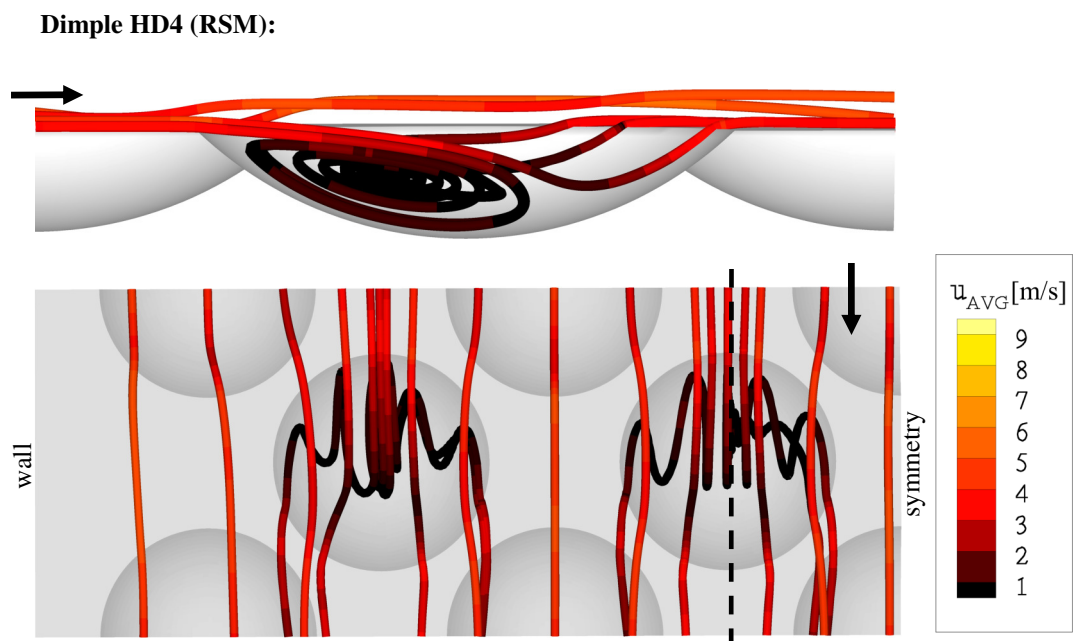


Fig. 5.5: Flow situation of test case Dimple HD4 close to the dimpled wall at $Re_D \sim 130K$

To obtain a more detailed view on the flow field close to the dimpled wall, stream traces of test case Dimple HD4 are presented in Fig. 5.5. Looking at the upper plot, where a cross section through a dimple is shown, the typical flow features can be identified. Once the air flow close to the surface reaches the beginning of the dimple, the flow detaches. It takes approximately two-thirds of the dimple diameter until the stream traces are diverted and a recirculation zone is established. This is accompanied by a significant reduction of the mean velocity. From a heat transfer point of view, the formation of a recirculation zone, where a cooling flow is temporarily trapped and where the local velocity levels are low, leads to lower levels of heat transfer augmentation. Stream traces, which are located slightly above the surface at the beginning of the dimple, are not trapped in the recirculation zone. This portion of

cooling mass flow is diverted into the rear part of the dimple, where the fluid flow reattaches. Therefore, higher levels of heat transfer enhancement should be observed in the rear part of the dimple. Additionally, the acceleration of the fluid flow around the trailing edge of the dimple improves the heat transfer rate.

Looking from above on the dimpled surface, the influence of vortex rotation on the course of the stream traces is observable. Stream traces, which touch these regions of higher rotation, are affected. Close to the leading edge of the dimple, stream traces located slightly above the dimpled surface are shifted towards the dimple center. Close to the trailing edge this trend is inverted. The stream traces are diverted away from the dimple center. It is noticeable that stream traces, which enter the recirculation zone inside the dimple close to the center, are ejected away from the dimple center.

As a result of the numerical computation it can be stated that regions of higher X-Vorticity affect the stream traces, but the effect is too low to create vortices. Once the next dimple row is reached, the influence of the previous dimple row is nearly undetectable. Further, the mean flow is influenced to a smaller extent.

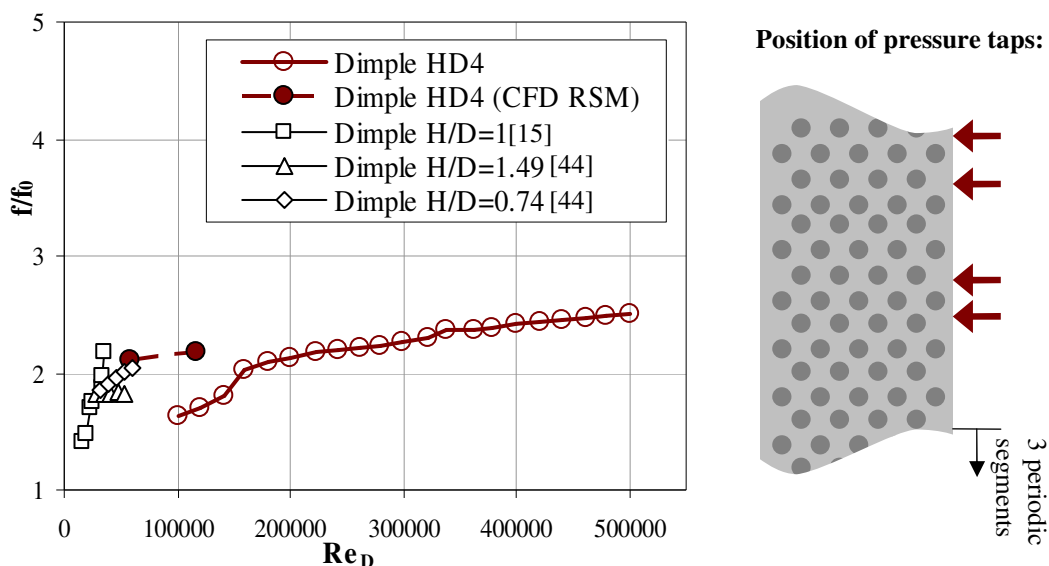


Fig. 5.6: Friction factor ratios f/f_0 of test case Dimple HD4 and data from literature

Friction factor

The friction factor ratios of test case Dimple HD4 are presented in Fig. 5.6. Literature data is added for comparison with the present data. It has to be mentioned that the geometrical parameters of the published configurations do not match entirely with the current test case.

Compared to the friction factor ratios of all ribbed configurations, the friction factor ratio level of test case Dimple HD4 is lower. For test case V10-1s friction factor ratios

started at $f/f_0 \approx 3$. This level is not reached by the dimpled surface, even for the highest Reynolds numbers.

Due to convergence problems of the numerical computations at higher Reynolds numbers, numerically obtained data could only be obtained for the smaller Reynolds number range. Compared to the ribbed test configurations, where the computational results were found to underestimate the experimental data, an extrapolation of the numerically obtained data shows sufficient agreement.

To compare the numerically and experimentally obtained values, data provided in literature is consulted. The three test cases with a varying dimensionless channel height, which is normalized by the dimple diameter and is lower than for test case Dimple HD4, appear to result in a similar level of friction factor ratios. From the literature data it can not be clarified, if the reduction of the dimensionless channel height leads to a general trend to the overall pressure loss level. This issue is discussed in a later section.

Heat transfer enhancement

The flow features observed in the simulations close to the dimpled wall and inside the dimples determine the distribution of the local heat transfer enhancement. A slice, showing the heat transfer enhancement values along the channel mid-plane, is presented in Fig. 5.7.

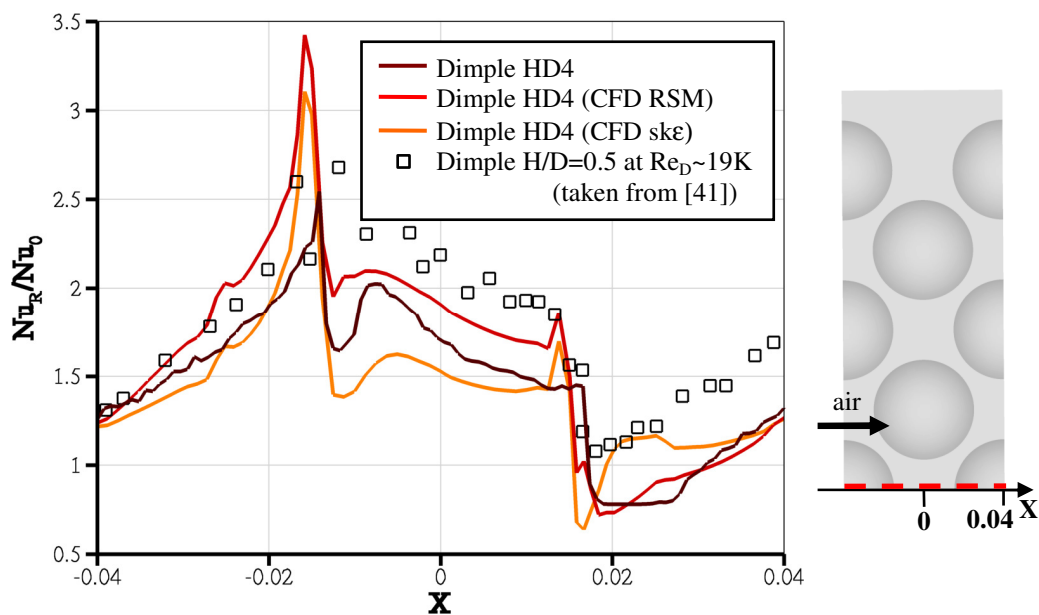


Fig. 5.7: Distribution of Nusselt number ratio of test case Dimple HD4 at $Re_D \sim 130K$ for mid-plane

In this figure, experimental data is presented together with the data from the simulation. They are obtained by applying the standard $k-\epsilon$ and the RSM turbulence model. Additionally, the local heat transfer enhancement, as experimentally determined by Mahmood et al. [41], is shown. As with the discussion of the friction factor, the parameters of the published configurations do not match entirely with the current test

case, but due to the lack of adequate literary sources the data provided by Mahmood et al. [41] is consulted.

Due to the reattachment of the flow close to the trailing edge of the dimple and due to the accelerating flow over the dimple's trailing edge, the heat transfer enhancement increases. Outside of the dimple, a decline of the heat transfer augmentation can be observed. This is related to the increase of the thermal boundary layer thickness. The decline remains unchanged until the next dimple is reached. As a result of the recirculation zone, the heat transfer enhancement level is reduced significantly. The lowest levels of heat transfer augmentation are found close to the leading edge inside the dimple.

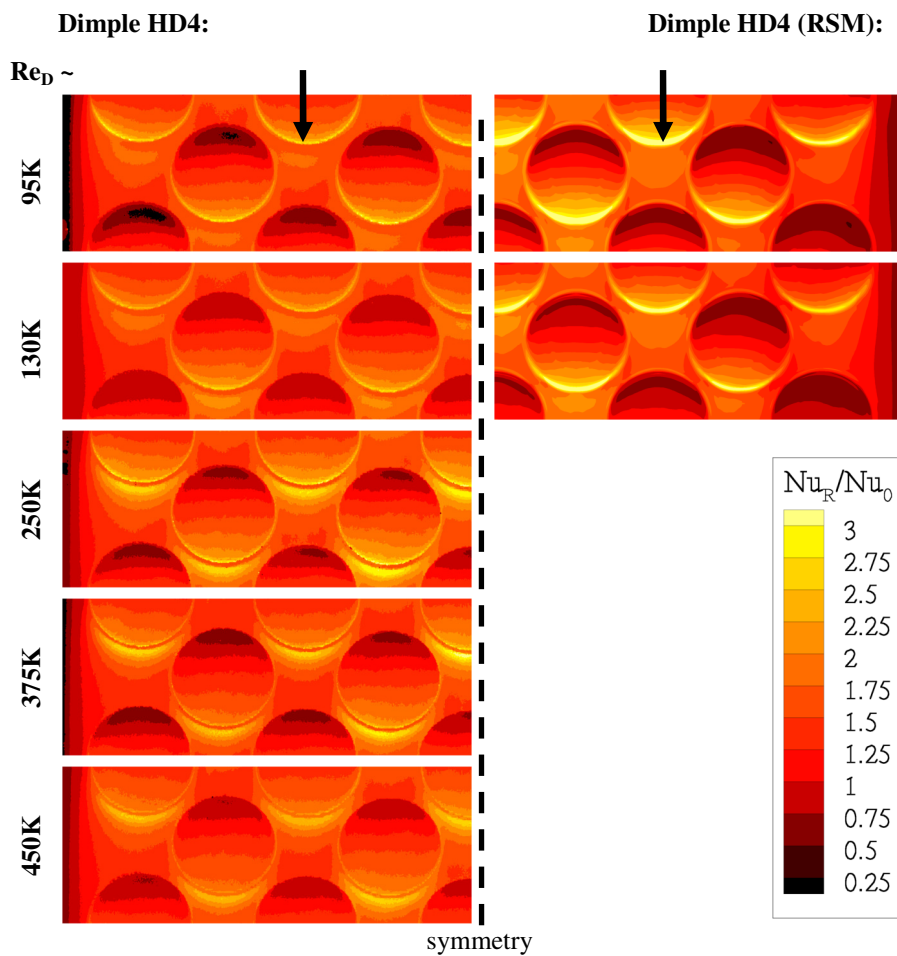


Fig. 5.8: Experimental and numerical local heat transfer ratios of test case Dimple HD4

Comparing the numerically and experimentally obtained distributions, the application of the RSM turbulence model seems to provide the closest prediction of the experimental trends. The heat transfer enhancement distribution, which is determined by the recirculation zone, is predicted appropriately according to the findings of the experiment. The standard k- ϵ turbulence model was not able to achieve a similar

distribution in the same location. Again, the RSM turbulence model provides superior results and therefore should be used for this type of channel flow.

Looking at the data set, which was published by Mahmood et al. [41], it is noted that the qualitative local heat transfer enhancement distribution is similar to the experimental data. A similar level of heat transfer augmentation is reported for the area in front of the trailing edge. Even the reported peak value matches the experimental data. For all other regions, the values provided by Mahmood et al. [41] for a Reynolds number of 19,000 are found to be above the measured data of the present study.

The experimental and numerical local heat transfer ratios of test case Dimple HD4 are presented in Fig. 5.8. In contrast to the ribbed configurations, where an increase of the Reynolds number leads to a decreasing heat transfer enhancement peak, this is not observed in the case of a dimpled channel wall. Furthermore, the variation of the Reynolds number seems to have nearly no influence on the heat transfer enhancement for the high Reynolds numbers investigated. Altogether, the overall heat transfer enhancement level is lower compared to the situation found for ribbed channel walls. For the dimpled surface, the maximum local Nusselt number ratios are reported to be around three times higher as for the heat transfer of a smooth channel wall.

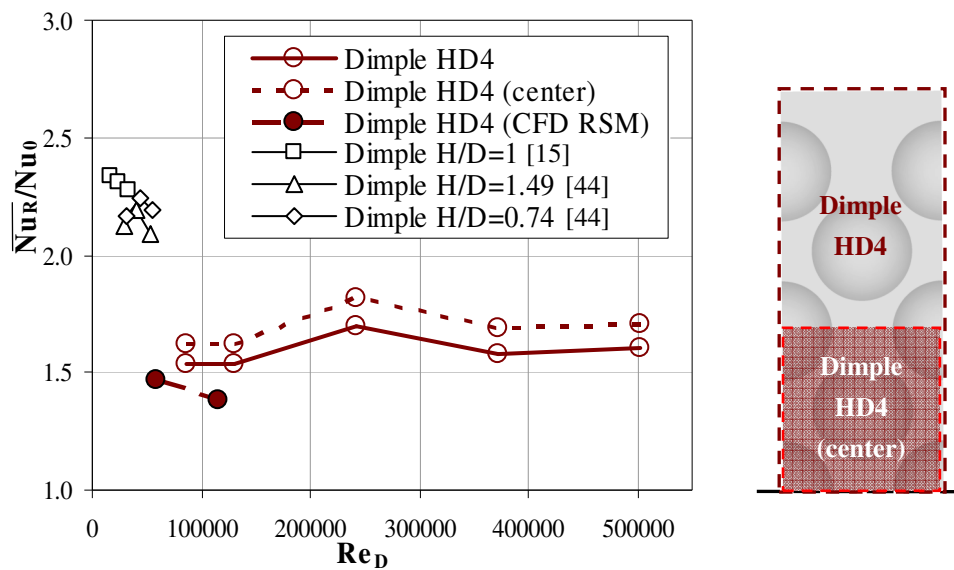


Fig. 5.9: Area-averaged Nusselt number ratios of test case Dimple HD4 and data from literature

To show the global heat transfer augmentation of test case Dimple HD4 and to compare it with data found in literature, the area-averaged Nusselt number ratios are presented in Fig. 5.9. The numerical computations using the RSM model are included and shown to underpredict the experimental data somewhat.

To compare the experimental and numerical results with previous studies, data found in literature is provided in Fig. 5.9. Within this chart, the presented data has been obtained using a similar experimental method, which is the transient liquid crystal measurement

technique. Moon et al. [44] conducted a study on dimpled surfaces. The dimensionless dimple-depth was $\delta/D = 0.19$, which is similar to the configuration of the present study and the Reynolds number varied between 30,000 and 54,000. A heat transfer enhancement of around 2.2 was reported. In the present study, the heat transfer enhancement level is around 1.6.

Chyu et al. [15] investigated dimpled channels with a dimensionless dimple-depth of $\delta/D = 0.25$ and for a Reynolds number range from 15,000 up to 35,000. Burgess et al. [8], who varied the dimensionless dimple-depth between $\delta/D = 0.1$ and $\delta/D = 0.3$, reported that the effect of having a deeper dimple is an increased heat transfer enhancement. As a consequence, it can be assumed, that with a reduced dimple-depth within the study of Chyu et al. [15] the heat transfer enhancement would be lower. But still, the heat transfer level would be around two times higher than for a smooth channel. Burgess et al. [8] reported a heat transfer enhancement of around two for a dimensionless dimple-depth of $\delta/D = 0.2$. In their study, the area-averaged heat transfer enhancement was averaged over the channel center only, which neglects the lower heat transfer enhancement levels close to the smooth channel side wall. Therefore, the area-averaged Nusselt number ratios of the center part only are also presented in Fig. 5.9. For the present study, this increases the area-averaged Nusselt number ratios by approximately 15 %.

In general, the data found in literature shows higher levels of heat transfer augmentation as presented in Table 5.2. The heat transfer enhancement for dimpled surfaces with a dimensionless dimple depth of $\delta/D = 0.2$ is reported to be at minimum 1.8 times higher than for a smooth channel wall. However, the investigated Reynolds number range in studies found in literature is too low to appropriately compare results. In the present study, this level of heat transfer augmentation could not be observed. If only the centre part of the dimpled surface is considered, the resulting heat transfer enhancement remains around 1.75.

Table 5.2: Reported Nusselt number ratios for dimpled surfaces

Reference	Aspect Ratio	H/D	δ/D	Re_D	Measurement technique	$\overline{Nu_R}/Nu_0$	
Dimple HD4	2:1	4	0.2	95K - 500K	transient technique with TLCs	1.5 - 1.7	
[44]	16:1	0.35	0.19	12K - 60K	transient technique with TLCs	2.1 - 2.3	
	7.4:1	0.76					
	5.1:1	1.11					
	3.8:1	1.46					
[8]	4:1	1	0.3	21K - 124K	steady technique with infrared camera	2.5 - 2.6	
			0.2				1.8 - 2.0
			0.1				
[22]	4:1	2	0.3	5K - 40K	steady technique with copper plates	1.6 - 2.2	

Reference	Aspect Ratio	H/D	δ/D	Re_D	Measurement technique	$\overline{Nu_R}/Nu_0$
[41]	8:1	0.5	0.2	19K - 115K	steady technique with infrared camera	1.8 - 2.4
[15]	12:1	0.33	0.25	15K - 35K	transient technique with TLCs	2.2 - 2.3
	4:1	1				
	2:1	2				

5.2 Dimples with H/D = 0.5, 1, 2

Within this section, the effect of a reduced dimensionless channel height is investigated. As a possible reason for the significant difference of the heat transfer enhancement data between literature (H/D in the range of H/D = 1.46 and H/D = 0.35) and the present study, the dimensionless channel height is successively reduced. To do so, spacers, which have been described in chapter 2.2, are used in the test section. A picture of the implemented spacers is given in Fig. 5.10 for test case Dimple HD1.

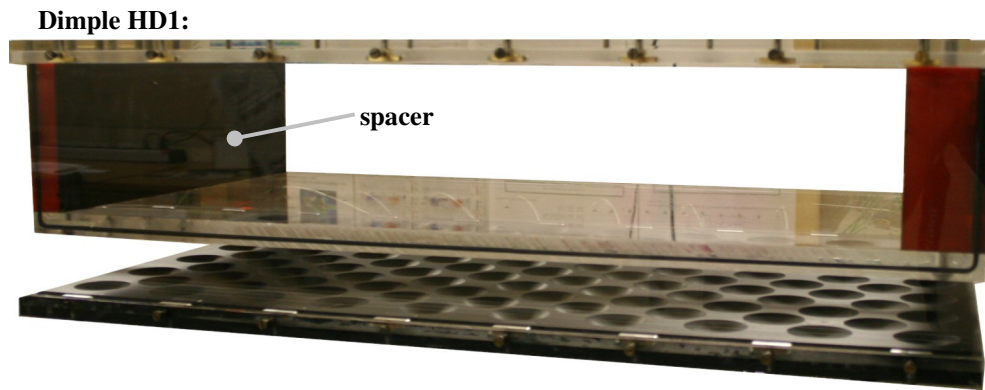


Fig. 5.10: Picture of test case Dimple HD1 with implemented spacers

The parameters of the investigated test cases are presented in Table 5.3. Due to the channel height variation, the minimum dimpled channel length-to-hydraulic diameter (l/D_h) with a constant channel cross section is 5 for test case Dimple HD2. Again, a minimum of five periodic segments are located in front of the measurement region, to provide nearly periodic flow conditions.

Table 5.3: Test case configurations of dimpled test cases

Test Case	Aspect Ratio	H/D	δ/D	No. of Dimpled Walls
Dimple HD2	4:1	2	0.2	1
Dimple HD1	8:1	1	0.2	1
Dimple HD0.5	16:1	0.5	0.2	1

Friction factor

To evaluate the influence of reducing the dimensionless channel height on the overall pressure loss, the friction factor ratios of test cases with a dimpled surface are presented in Fig. 5.11. From this figure, it is noticed, that reducing the dimensionless channel height H/D leads to an increased friction factor ratio for a given Reynolds number.

Looking at the data found in literature, an extrapolation of the measured friction factor ratios of the present study would meet the data points found in literature. Burgess et al. [8] reported that the friction factor ratio is relatively independent of the Reynolds number and the channel height. In contrast to this study, where no dimensionless channel height effect is reported, the influence of the channel height on the friction factor ratios can obviously not be neglected for the investigated Reynolds number range of the present study.

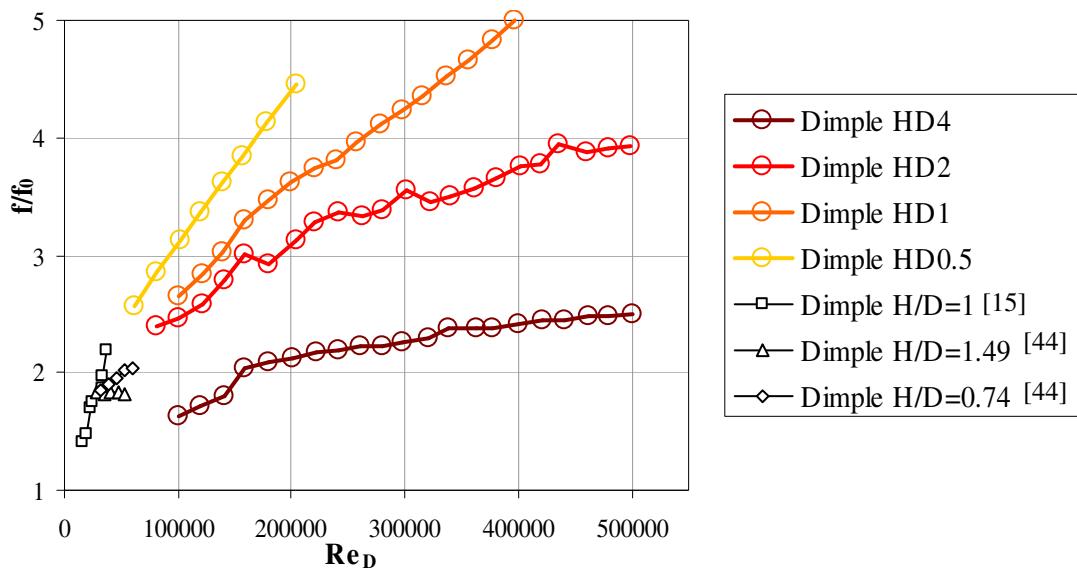


Fig. 5.11: Friction factor ratios f/f_0 of test cases with dimpled surface and data from literature

Heat transfer enhancement

In this section, the effect of a reduced dimensionless channel height on the heat transfer augmentation is described. Therefore, the area-averaged Nusselt number ratios are presented in Fig. 5.12.

The present data reveals that all investigated test configurations with dimples on one channel wall provide a similar level of heat transfer enhancement on the dimpled wall. The heat transfer augmentation level could not be enhanced significantly by reducing the dimensionless channel height. Similar findings were reported by Moon et al. [44], who varied the dimensionless channel height between $H/D = 1.46$ and $H/D = 0.35$. In their study, it was concluded to observe an effect of the channel height on the heat transfer enhancement, the channel height has to be of the order of the dimple depth.

From this observation, it can be stated, that for the present study a variation of channel height has no effect on the heat transfer enhancement in the investigated Reynolds number range.

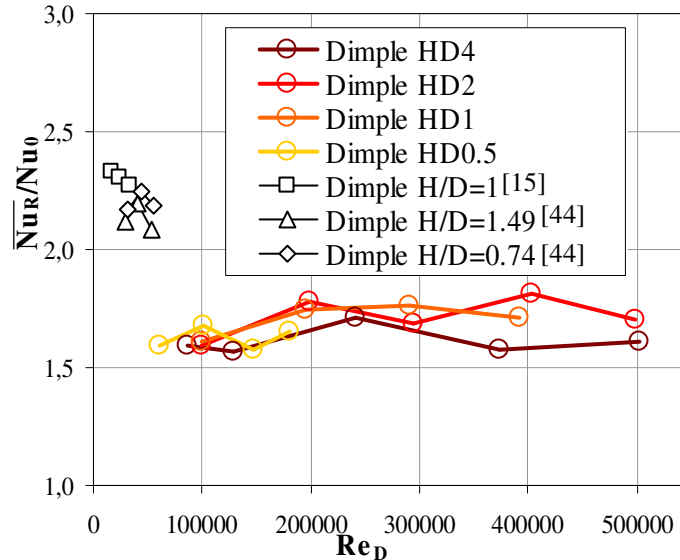


Fig. 5.12: Area-averaged Nusselt number ratios of test cases with dimple surfaces and data from literature

5.3 Conclusions on Dimples

Experiments and numerical computations on dimpled surfaces are presented in this study. In a first set of investigations, the test channel cross section is kept constant compared to the ribbed test configurations.

The numerically obtained mean velocity profiles revealed that the overall distribution is similar to the mean velocity profile found for a channel with one roughened wall. Similar findings have been reported for WW-shaped ribbed channels. Compared to the ribbed test channel, no large-scale secondary flow features could be detected for channels with a dimpled surface.

The influence of the chosen turbulence model on the numerical computations has been investigated. A plot of the X-Vorticity close to the dimpled surface reveals that only the RSM turbulence model is able to realize vortex cells, which are capable of detaching from the dimpled surface and penetrate the air flow above the dimpled surface. To initiate secondary flow structures, the energy level of those cells is thought to be too low. Therefore, the stream traces above the dimpled surface are shifted only slightly. For Reynolds numbers above $Re_D \sim 130K$, the numerical computations had convergence problems.

Test case Dimple HD4 reveals the lowest pressure losses measured within the present study. Here, the results of the numerical computations using the RSM turbulence model

agree well with data measured in experiments and with data found in literature. For the investigations on heat transfer, a different situation is found. Again, numerical prediction and experimental measurements show a similar level of heat transfer enhancement. Compared to data found in literature, the reported level of heat transfer augmentation is lower. It must be mentioned, that the available data base is too limited to allow a final assessment of the results applicable to the conditions typically found in backside cooled combustor walls. A slice of the local heat transfer enhancement data along the mid plane on the dimpled surface shows that, compared with data found in literature, the qualitative characteristics are captured well by the numerical and experimental study.

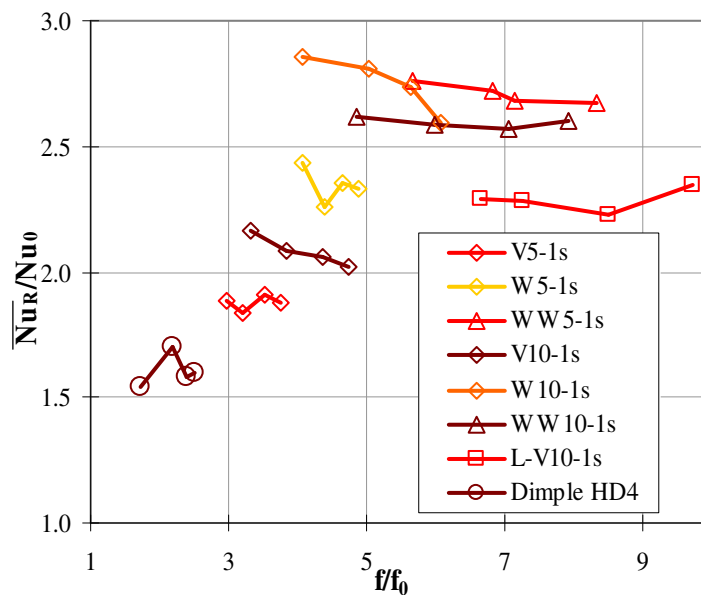


Fig. 5.13: Experimentally obtained heat transfer augmentation plotted over friction factor ratio for the presented ribbed test configurations and test case Dimple HD4

Further investigations revealed that the dimensionless channel height has no effect on the level of heat transfer enhancement within the investigated parameter range. A reduction of the dimensionless channel height is to increase the pressure losses.

As for the ribbed test cases, the experimentally obtained heat transfer augmentation of test case Dimple HD4 is plotted over the friction factor ratio and presented in Fig. 5.13.

For a combustor design, where a high heat transfer enhancement is needed, the dimpled channel wall is not able to compete with ribbed geometries. But due to the lower friction factor ratios, the dimpled channel is still an interesting alternative to ribbed channels in situations, where lower levels of heat transfer enhancement are sufficient to provide the desired cooling and the design is directed towards low pressure losses.

6 Hemispheres

An alternative approach to enhance the heat transfer level using small hemispheres added onto the channel wall is described in this section. Due to their small spatial dimension this convective cooling technique is not considered to initiate large-scaled secondary flow features. Therefore, this cooling technique belongs in the category of heat transfer enhancement due to roughness elements.

6.1 Hemispheres with $L/d_0 = 2, 3, 4, 5$

Within this study, the elements have a diameter of $d_0 = 10$ mm. To characterize the distribution of the hemispheres a dimensionless parameter is used. This parameter is defined by dividing the distance between two hemispheres L with the diameter of one hemisphere d_0 . For the investigated test cases, this dimensionless parameter is gradually reduced from $L/d_0 = 5$ to $L/d_0 = 2$. A reduction of L/d_0 means that the roughness density is increased. The dimensionless roughness height-to-hydraulic diameter is kept constant at $k/D_h = 0.019$. The test case configurations of the investigated channels with hemispheres are presented in Table 6.1. The definition of the hemisphere parameters and the hemisphere pattern is shown in Fig. 6.1.

Table 6.1: Test case configuration of channel with hemispheres

Test Case	Aspect Ratio	L/d_0	k/d_0	No. of Walls With Hemispheres
Hemi 50	2:1	5	0.019	1
Hemi 40	2:1	4	0.019	1
Hemi 30	2:1	3	0.019	1
Hemi 20	2:1	2	0.019	1

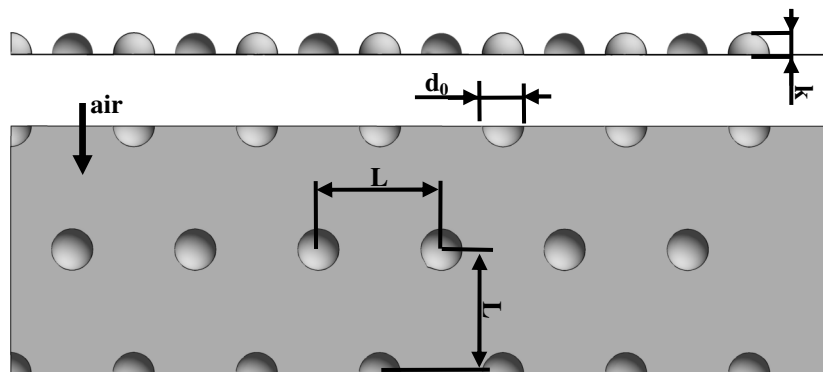


Fig. 6.1: Hemisphere pattern

To obtain additional insight on the actual hemisphere distribution, a picture of each test case is presented in Fig. 6.2. The total channel length, where the channel is covered with hemispheres, is based on the hydraulic diameter and expressed in a dimensionless channel length-to-hydraulic diameter ratio (l/D_h). This factor is 1.5 for test case Hemi 20 and 3 for all other test cases with hemispheres. Due to this, it is ensured that a minimum of five periodic segments are located in front of the measurement region.

As can be noticed by looking at the pictures of the different hemisphere test cases, the total number of hemispheres is gradually increased, if the dimensionless roughness parameter is reduced. The total surface area between the different test cases is not similar. For test case Hemi 20, the highest amount of additional surface area is found.

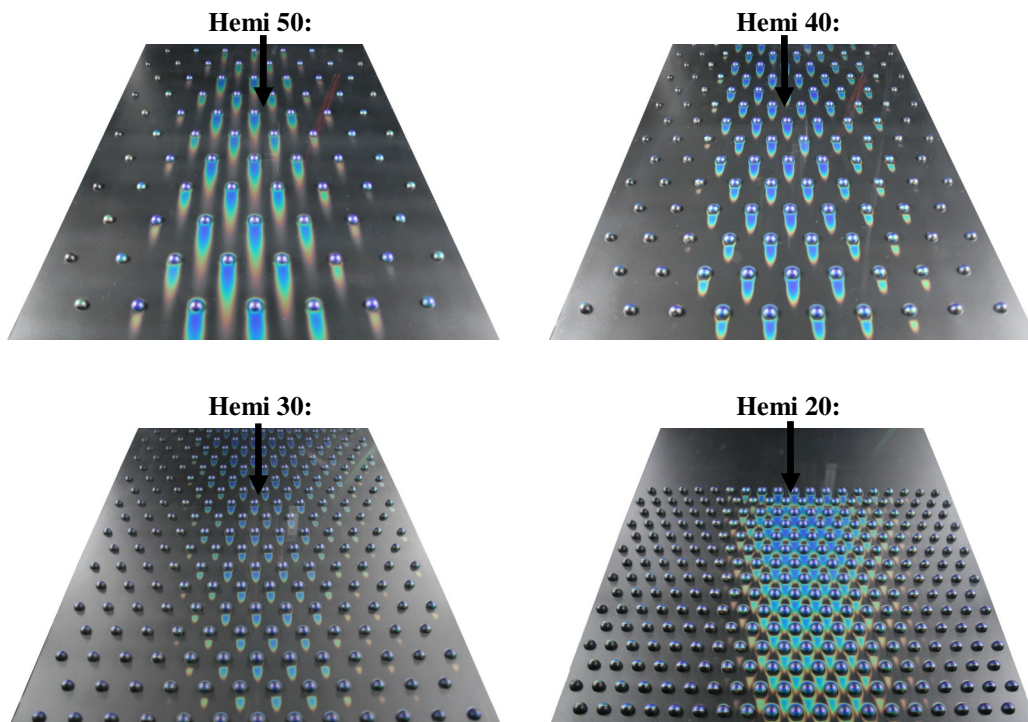


Fig. 6.2: Hemisphere test cases

In addition to the transient liquid crystal measurement method, with which spatially resolved heat transfer coefficients are resolved, numerical computations are conducted to provide details of the velocity field. A periodic segment of the test channel, which is roughened with hemispheres on one channel side wall, is meshed as presented in Fig. 6.3 together with the total number of nodes.

From the experience derived from the numerical computations of the dimpled channel, only the Reynolds Stress Model (RSM) is used. Compared to the dimples as described in the previous chapter, the roughness elements in the present investigations are smaller in size. Therefore, the expected vortex structure, which is generated by the hemispheres, is assumed to be smaller in size and strength. For this reason, the standard $k-\epsilon$ turbulence model is considered to be inappropriate for numerical computations.

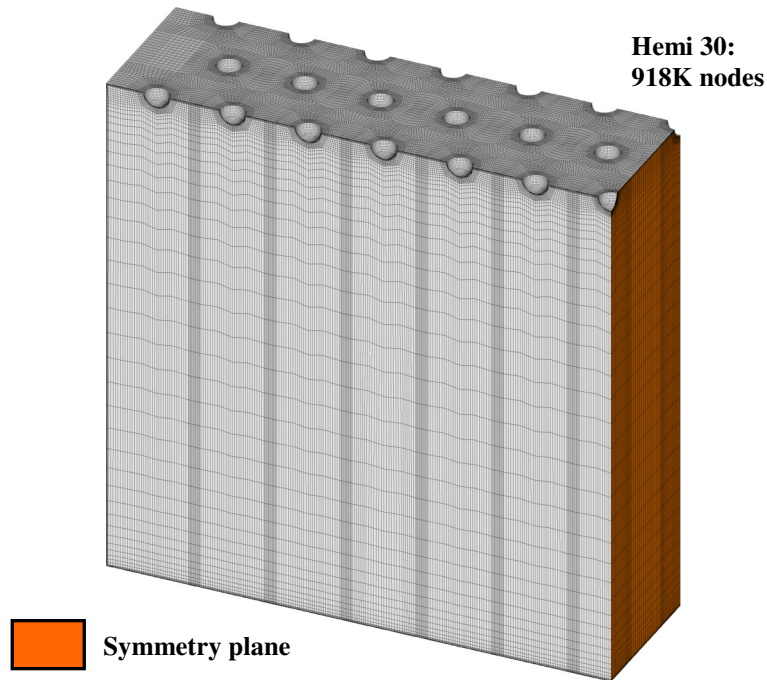


Fig. 6.3: Grid and number of nodes for test case Hemi 30

Velocity Field

As a result of the numerical computation, details on the flow field situation of channels with hemispheres on one channel wall are obtained. The computational mean velocity profile of test case Hemi 30 is presented in Fig. 6.4.

Hemi 30 (RSM):

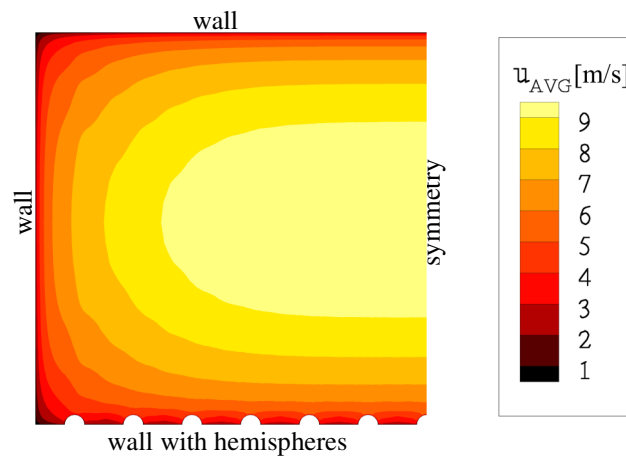


Fig. 6.4: Computational mean velocity profiles of test case Hemi 30 at $Re_D \sim 130K$

Looking at the computed mean velocity profile of the channel cross section, no major secondary flow features can be detected. The velocity distribution is comparable with a mean velocity profile of a channel with smooth channel walls only. As for a smooth channel, the position of the maximum mean velocity is located in the center of the

channel cross section. Due to relatively low blockage of the hemispheres, the velocity profile close to the hemispheres is shifted only slightly. Therefore, the comparatively small hemispheres have no major influence on the velocity profile of the core flow.

For the flow field situation close to the channel wall with hemispheres, a more detailed view is given in Fig. 6.5.

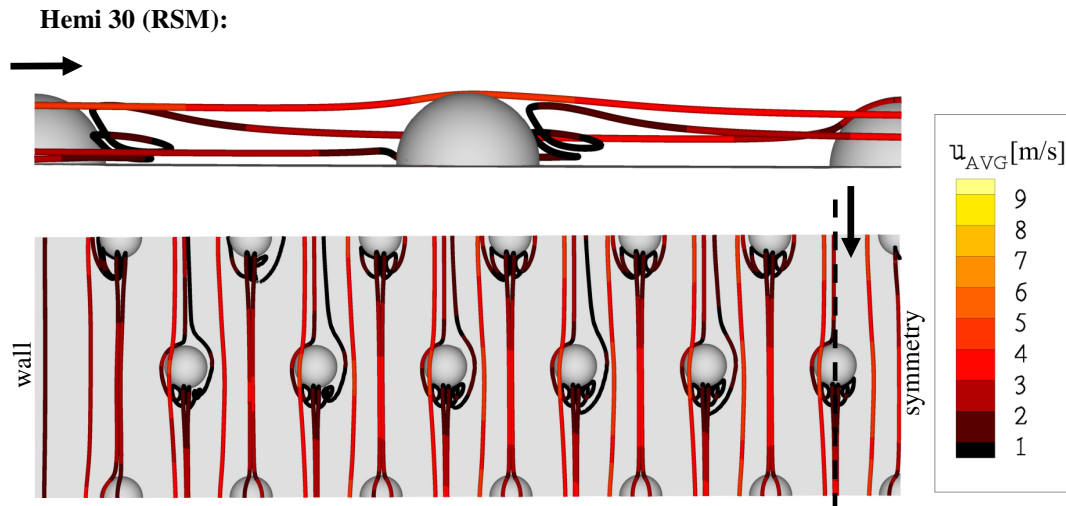


Fig. 6.5: Flow situation of test case Hemi 30 close to the channel wall with hemispheres at $Re_D \sim 130K$

As can be noticed by looking from the top onto the channel wall with hemispheres, the flow in front of a hemisphere decelerates. As the flow approaches a hemisphere, the flow field is diverted around the hemisphere. Close to the position, where the maximum blockage of the hemisphere is reached, the flow field detaches forming a recirculation zone directly behind the hemisphere. This recirculation zone is predicted to have a spatial dimension of less than one hemisphere diameter. About two diameters downstream of the hemisphere, the streamtraces are again well aligned with the main flow direction of the core flow.

Looking at the streamtraces slightly above the hemispheres, it is observed that the streamtraces are only slightly diverted by the hemispheres. Therefore, the interaction between core flow and flow close to the hemispheres is considered to be low.

Friction Factor

The friction factor ratios f/f_0 of the investigated test cases with hemispheres on one channel wall are presented in Fig. 6.6. As can be seen, the friction factor ratios of all test cases rise with increasing Reynolds number. Among the present test cases, test case Hemi 50 results in the lowest pressure losses. Here, the friction factor ratio varies between $f/f_0 \approx 1.7$ and $f/f_0 \approx 2.2$. As a consequence, the friction factor ratio of test case Hemi 50 stays below the given results of test case Dimple HD4, a channel with a dimpled surface. Those results have been reported in chapter 5.

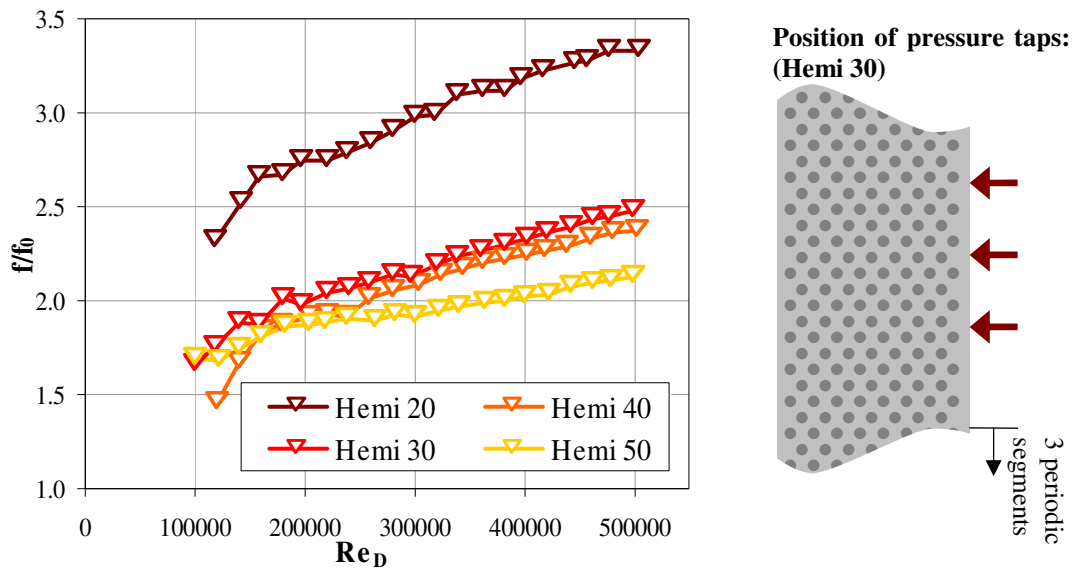


Fig. 6.6: Friction factor ratios f/f_0 of test cases with hemispheres

Compared to test case Hemi 50, the roughness densities of test case Hemi 40 is increased. This leads, for a given Reynolds number, to a slightly higher friction factor ratio. Increasing the roughness densities even further, as done for test case Hemi 30, the friction factor ratio is again higher for a given Reynolds number compared to test cases Hemi 40 and Hemi 50. Still, the highest friction factor ratio of test case Hemi 30 is around $f/f_0 \approx 2.5$. The numerical computation of test case Hemi 30 at a Reynolds number of $Re_D \approx 130K$ resulted in a friction factor ratio of 1.4, which underpredicts the experimental data. It proved to be difficult to obtain converged numerical computations for higher Reynolds numbers or closer roughness spacings.

The reported friction factor ratio for a given Reynolds number of test case Hemi 20, which has the highest roughness density within this study, is higher than for all other test cases with hemispheres. The friction factor ratio varies between $f/f_0 \approx 2.4$ and $f/f_0 \approx 3.4$. Looking at the four test cases with hemispheres, the offset between the friction factor ratios of test case Hemi 20 and Hemi 30 is much higher than between the other test cases. The friction factor ratio seems to be more similar for a roughness densities below $L/d_0 = 3$, whereas a further reduction of L/d_0 leads to a stronger increase of the friction factor ratio.

Heat transfer enhancement

After the velocity field and the friction factor ratios have been discussed, the local distribution of the experimentally obtained heat transfer enhancement for two different Reynolds number is presented in Fig. 6.7.

Looking at each test case separately, the local heat transfer distribution for the two different Reynolds numbers is similar, expect for the surfaces close to the smooth

channel sidewall. Here, the heat transfer enhancement is slightly higher for a Reynolds number of $Re_D \sim 450K$.

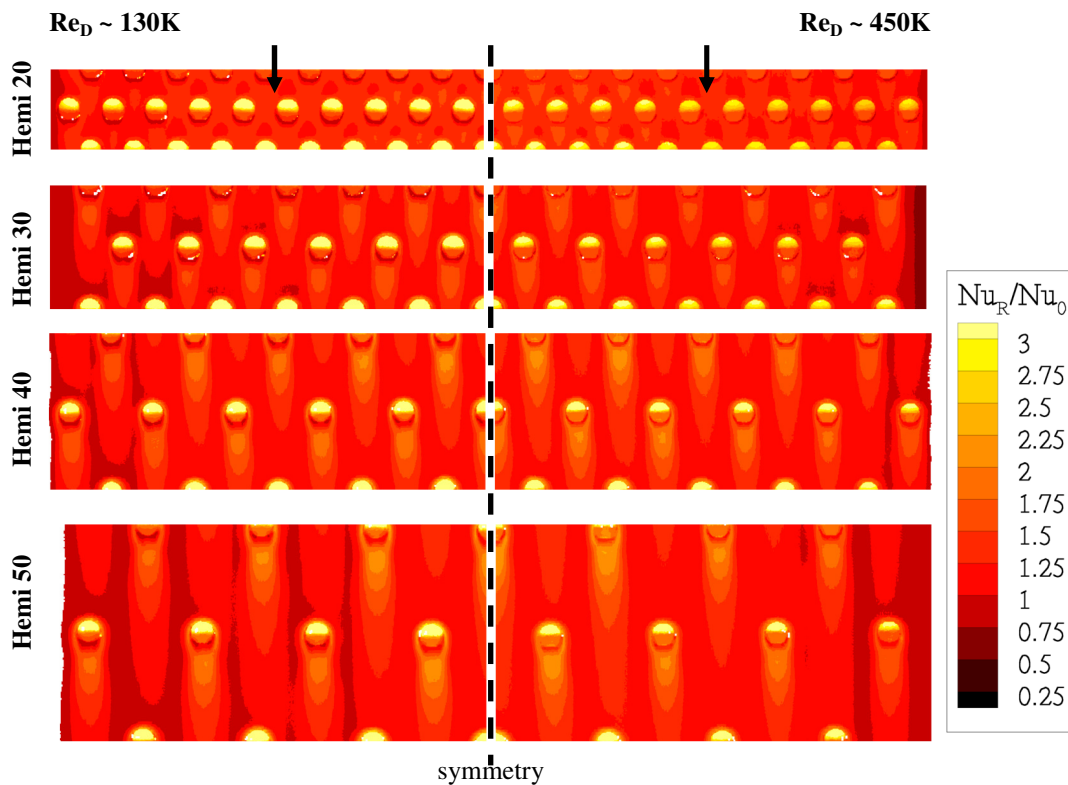


Fig. 6.7: Experimental local heat transfer ratios of test cases with hemispheres

It is noticeable, that the local heat transfer enhancement patterns on the hemispheres themselves are similar for all test cases and Reynolds numbers. Clear differences between the test cases are only observable for a variation of the roughness density. For test case Hemi 50, the presence of a hemisphere enhances the heat transfer slightly before and behind the hemisphere. This region behind the hemisphere is of the size of two times the hemispheric diameter, in which heat transfer enhancement levels of around two times the heat transfer enhancement of a completely smooth channel are reached. Further downstream, the heat transfer enhancement drops to levels of heat transfer enhancement of $Nu_R/Nu_0 \approx 1$. Similar findings have been reported by Chyu and Natarajan [14], who investigated the local heat transfer distribution of single roughness elements including a hemisphere.

The main idea of increasing the roughness density is to condense those areas on the roughened channel wall, on which the hemispheres augment the heat transfer. Additionally, the overall surface area is increased as the total number of hemispheres is raised. For test case Hemi 50, the overall surface area is raised by only 3 % compared to a smooth channel wall. In the case of test case Hemi 40 and Hemi 30, the overall area is increased by 5 % and 8 %, respectively. The largest area increase within this study is found for test case Hemi 20. Here, the surface area is increased by 19 %.

In Fig. 6.8 the distribution of the Nusselt number ratio for the test cases with hemispheres for the channel mid-plane is presented. It is interesting to note, that reducing the distance between two successive hemispheres leads to a decline of the heat transfer augmentation. The maximum level of heat transfer enhancement downstream of the hemisphere is lower as the roughness density is increased.

On one side, the overall surface area is increased, which has a positive impact on the heat transfer situation. On the other hand, the level of maximum heat transfer enhancement behind the hemisphere is lowered as the distance between the hemispheres is reduced. It is assumed, that this is mainly caused by the growing interaction due to the denser roughness element spacing.

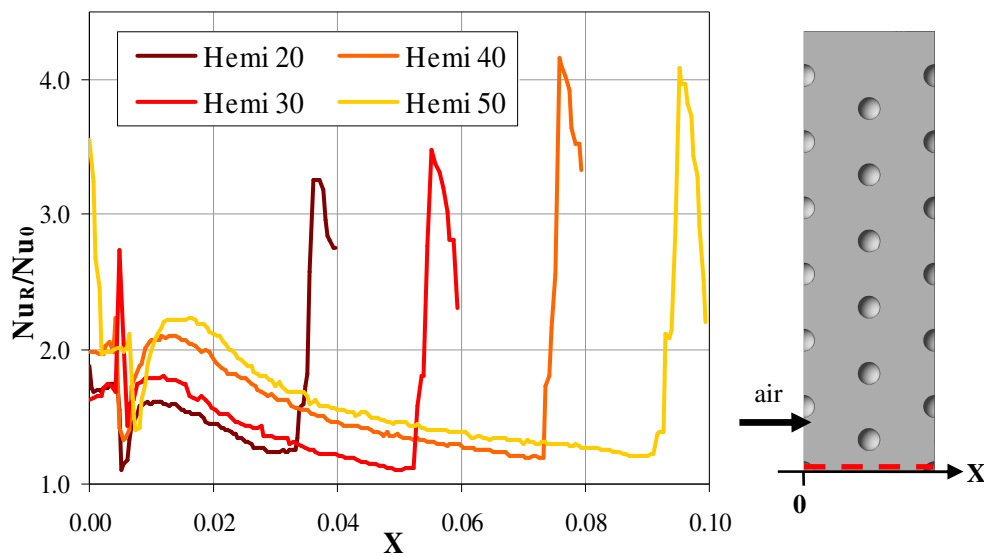


Fig. 6.8: Distribution of Nusselt number ratio of test cases with hemispheres at $Re_D \sim 450K$ for mid-plane

To reveal the impact of the overall area increase and the different heat transfer situations between the hemispheres on the cooling performance, the area-averaged heat transfer enhancement is presented in Fig. 6.9.

As for ribbed and dimpled channels, which have been discussed in previous chapters, the heat transfer enhancement shows a constant behaviour for an increasing Reynolds number at these high Reynolds number conditions.

It is noticeable, that test case Hemi 50 provides the lowest level of overall heat transfer enhancement. Here, the heat transfer enhancement is only around 1.3 times higher than for a smooth channel. Looking at test case Hemi 40 and Hemi 30, the area-averaged heat transfer enhancement is slightly higher. Also in these cases, the heat transfer enhancement stays below 1.5 times the heat transfer enhancement of a smooth channel. The numerical computation of test case Hemi 30 at a Reynolds number of $Re_D \sim 130K$

resulted in an area-averaged heat transfer enhancement of 1.2 and, therefore, underpredicts the experimentally obtained data.

Test case Hemi 20 provides the highest overall heat transfer enhancement. A major reason for the offset to the heat transfer enhancement values of test case Hemi 30 is that test case Hemi 20 occupies the highest overall surface increase. Additionally, the total number of hemispheres is significantly increased compared to the other test cases. This has a positive impact on the heat transfer enhancement, because the local distribution of the heat transfer enhancement on the hemispheres revealed high levels of heat transfer enhancement on the surface parts, which are facing upstream.

In another study, Hosni et al. [29] provided experimentally obtained data on the heat transfer enhancement of uniformly distributed roughness elements in a developing turbulent boundary layer. In their study, the Reynolds number range varied between $Re_D \sim 67K$ and $Re_D \sim 740K$. They reported that the level of heat transfer enhancement for a dimensionless parameter of $L/d_0 = 4$ augments the heat transfer enhancement by +25 % compared to a smooth channel. For a dimensionless parameter of $L/d_0 = 2$, the level of heat transfer enhancement was found to be 1.75 times higher than for a smooth channel. These findings are in good agreement with the reported data of this study.

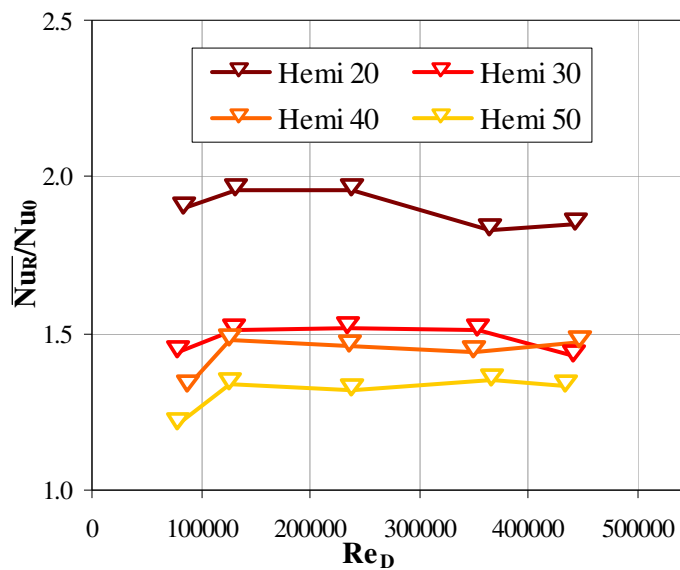


Fig. 6.9: Area-averaged Nusselt number ratios of test cases with hemispheres

6.2 Conclusions on channels with hemispheres

Experimental studies and numerical computations of channels with hemispheres on one channel wall are presented in this study. The influence of a varying roughness density on the friction factor ratio and the heat transfer enhancement is investigated.

From the detailed flow field obtained with the numerical computation, it is assumed, that no major secondary flow features are introduced by the hemispheric roughness elements. The impact on the main channel flow is considered to be low.

For the four different test cases, it could be demonstrated that the friction factor ratio and the heat transfer enhancement increase with a closer spacing of the roughness elements. As a result of the higher roughness density, the total number of roughness elements increases. For the thermal transport, this has a positive impact on the area-averaged heat transfer. On those parts of the hemispheres, where the approaching flow field stagnates, the local heat transfer enhancement is a maximum. Additionally, higher numbers of roughness elements add additional surface area to the channel wall. Otherwise, the local heat transfer enhancement between the hemispheres is reduced as the spatial distribution of the hemispheres becomes denser.

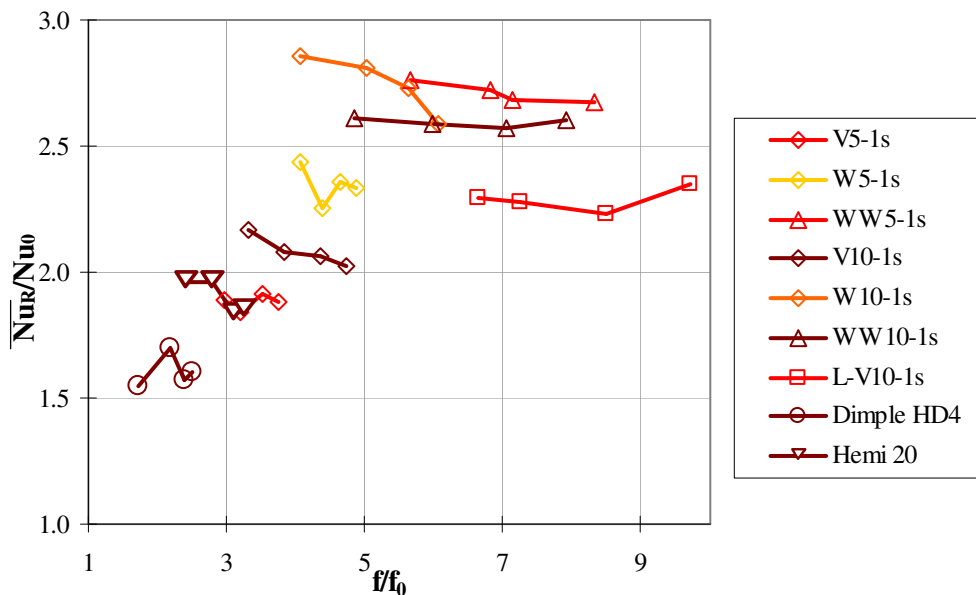


Fig. 6.10: Experimentally obtained heat transfer augmentation plotted over friction factor ratio for the presented ribbed and dimpled test configurations and test case Hemi 20

In Fig. 6.10, the experimentally obtained heat transfer augmentation of test case Hemi 20 is plotted over the friction factor ratio together with data from ribbed and dimpled channels to assess the cooling performance of channels with hemispheres on one channel wall.

As can be noticed from this chart, test case Hemi 20 provides higher levels of heat transfer as the test case Dimple HD4. Simultaneously, the pressure losses are slightly higher. Due to the lower pressure losses of test case Dimple HD4, this configuration performs just as well as test case Hemi 20 in convectively cooled combustor walls. Again, it has to be pointed out, that configurations such as test case Dimple HD4 are preferred only in situations, where a lower demand of heat transfer enhancement is sufficient in the design process of a backside cooled combustion chamber wall and the focus is rather on small overall pressure losses. Here, it should be taken into account,

that a wall with dimples will reduce the local combustor liner wall thickness, which is not the case with hemispheres.

7 Conclusions

Within this study, experimental and numerical investigations of convective cooling configurations for gas turbine combustors are conducted. The main goals of these investigations were to provide data on pressure loss and heat transfer enhancement for the different convective cooling configurations at conditions typically found on backside cooled combustion chamber walls.

There are several ways to enhance the convective heat transfer on a channel wall at high Reynolds numbers. First, the widely-used rib turbulators should be considered for an appropriate cooling design. Also, the possibility of dimpled surfaces or uniformly distributed roughness elements is considered.

For each group of convective cooling configurations, detailed conclusions are presented at the end of the respective chapter. Therefore, only the main conclusions of this study are summarized in this chapter.

For ribbed channels, it could be demonstrated that a reduction of the dimensionless rib height based on the hydraulic diameter e/D_h leads to lower pressure penalties. For practicable reasons originating with the casting process of a combustor wall, there is a lower limit of the dimensionless rib height. Ribbed channels with a dimensionless rib height of $e/D_h = 0.02$ as used for most ribbed test cases within this study are feasible. At the same time, the design requirement to produce moderate pressure losses is satisfied.

Comparing data of one-sided ribbed and two-sided ribbed channels, it could be revealed, that there is an influence on the pressure loss and heat transfer enhancement. It is recommended, not to directly use investigations and correlations of two-sided ribbed channels for the design of one-sided ribbed channels.

The numerical computations on channels with V-shaped, W-shaped and WW-shaped ribs, underpredicted the experimental data, but the general trends are captured. In this study, the commercial tool FLUENTTM is used, which solves the Reynolds-averaged Navier Stokes equations together with a standard k- ϵ turbulence model. This approach is considered to be appropriate during the preliminary industrial design process.



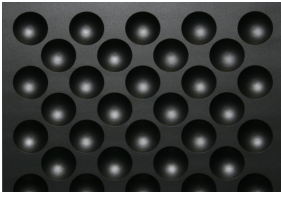
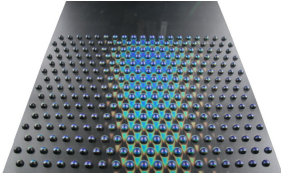
In general it can be noted that for similar rib height and rib spacing the friction factor ratio tends to increase as the rib geometry becomes more complex. V-shaped ribs show lower pressure loss compared to W-shaped or WW-shaped ribs. If the rib spacing is reduced from a rib pitch-to-height of $P/e = 10$ to $P/e = 5$, the friction factor ratio is lowered for V-shaped and W-shaped ribs. For WW-shaped ribs this trend is inverted.

For the W-shaped ribs, the heat transfer enhancement on the rib itself is reported. A reduction of the rib pitch seems to have no impact on the level of heat transfer enhancement on the rib itself. In combination with the heat transfer enhancement between two successive ribs, the heat transfer enhancement of W-shaped ribbed channel

walls is reported to produce three times higher levels of heat transfer enhancement than for a smooth channel wall.

In contrast to the test cases with V-shaped, W-shaped and WW-shaped ribs, no distinct main secondary flow features could be identified for dimpled channel walls and walls with uniformly distributed roughness elements. The vortices, which are generated by such elements, are smaller than and not as dominant as the secondary flow features found with V-shaped ribs. It could be demonstrated that for the numerical computation of such configurations, the turbulence model needs to be able capture the small scaled flow structures. It is recommended, to use a Reynolds Stress Model instead of the standard k- ϵ type turbulence model.

Table 7.1: Pros and Cons of selected test cases

Test Case	Pros and Cons
<p>W10-1s:</p> 	<ul style="list-style-type: none"> + The highest heat transfer enhancements of around $Nu_R/Nu_0=2.8$ are obtained for this configuration. + If the heat transfer on the rib is considered, the heat transfer enhancement is enlarged to around $Nu_R/Nu_0=3.0$. + The best thermal performance is achieved. - The friction factor ratio varies from $f/f_0=3.2$ to $f/f_0=6.3$.
<p>W5-1s:</p> 	<ul style="list-style-type: none"> + High heat transfer enhancements of around $Nu_R/Nu_0=2.4$ are realized for this configuration. + If the heat transfer on the rib is considered, the heat transfer enhancement is enlarged to around $Nu_R/Nu_0=2.8$. + The friction factor ratio varies from $f/f_0=3.8$ to $f/f_0=5.0$ and is lower compared to test case W10-1s. - The thermal performance is slightly lower compared to test case W10-1s.
<p>Dimple HD4:</p> 	<ul style="list-style-type: none"> + Low friction factor ratios of below $f/f_0=2.5$ are realized. - The heat transfer enhancement of around $Nu_R/Nu_0=1.6$ is comparatively low. - The wall thickness of the combustion chamber is reduced.
<p>Hemi 20:</p> 	<ul style="list-style-type: none"> + Low friction factor ratios of below $f/f_0=3.4$ are realized. - The heat transfer enhancement of around $Nu_R/Nu_0=1.9$ is comparatively low.

Compared to ribbed channels, low levels of pressure loss can be achieved with dimpled surfaces and surfaces with hemispheres. At the same time, the level of heat transfer

enhancement of the investigated configurations stays below the results of the ribbed test cases except for test case V5-1s.

For the dimpled test cases, a variation of the channel height had no influence on the heat transfer enhancement in the investigated parameter range. Only the pressure loss increases as the channel height is reduced.

In the case of channel walls, which are equipped with uniformly distributed hemispheres, the pressure loss and the heat transfer enhancement increases as the spacing between the roughness elements is reduced.

For the design process of backside cooled combustion chamber walls, the range of the investigated test cases offers the possibility to find adequate convective cooling configurations for different design demands. In situations where the friction factor is the limiting parameter, dimpled walls prove to be an interesting alternative to ribbed channels. If thermal performance is the desired design parameter, W-shaped ribs is the better choice in channels with an aspect ratio of $AR = 2:1$ and at high Reynolds numbers.

The conclusions are completed with a breakdown of the pros and cons of selected test cases, which are considered to be promising candidates for a convectively cooled combustion chamber wall. This overview is presented in Table 7.1.

Literature

- [1] AFANASYEV, V., N.; CHUDNOVSKY, YA., P.; LEONTIEV, A. I.; ROGANOV, P., S.: *Turbulent Flow Friction and Heat Transfer Characteristics for Spherical Cavities on a Flat Plate*. Experimental Thermal and Fluid Science, vol. 7, pp. 1-8, 1993.
- [2] AL-HADHRAMI, L.; GRIFFITH, T.; HAN, J. C.: *Heat Transfer in Two-pass Rotating Rectangular Channels (AR=2) with Five Different Orientations of 45 deg V-shaped Rib Turbulators*. ASME Journal of Heat Transfer, vol. 125, pp. 232-242, 2003.
- [3] AMRO, M.: *Untersuchung des Wärmeübergangs in einem Strömungskanal einer Gasturbinenschaufel (German)*. Signature: Dissertation 2005/1940, Universität Stuttgart, Germany, 2004.
- [4] ANDERSON, D., A.; TANNEHILL, J., C.; PLETCHER, R. H.: *Computational Fluid Mechanics and Heat Transfer*. Published by Mc Graw-Hill, 1984.
- [5] BAEHR, H., D.; STEPHAN, K.: *Wärme- und Stoffübertragung (German)*. Published by Springer-Verlag, ISBN 3-540-64458-X, 1998.
- [6] BAILEY, J., C.; FRIC, J., I.; FRIC, T., F.; TOPALDI, A., K.; NIRMALAN, N., V.; BUNKER, R., S.: *Experimental and Numerical Study of Heat Transfer in a Gas Turbine Combustor Liner*. In Proceedings of ASME TURBO EXPO 2002, GT-2002-30183, 2002.
- [7] BUNKER, R., S.; OSGOOD, S., J.: *The Effect of Turbulator Lean on Heat Transfer and Friction Factor in a Square Channel*. In Proceedings of ASME TURBO EXPO 2003, GT-2003-38137, 2003.
- [8] BURGESS, N., K.; LIGRANI, P., M.: *Effects of Dimple Depth on Channel Nusselt Numbers and Friction Factors*. Journal of Heat Transfer, vol. 127, pp. 839-847, 2005.
- [9] BURGESS, N., K.; OLIVEIRA, M., M.; LIGRANI, P., M.: *Nusselt Number Behavior on Deep Dimpled Surfaces Within a Channel*. Journal of Heat Transfer, vol. 125, pp. 11-18, 2003.
- [10] BUTTSWORTH, D., R.; JONES, T., V.: *Radial Conduction Effects in Transient Heat Transfer Experiments*. Aeronaut. J., vol. 101, pp. 209-212, 1997.
- [11] ÇAKAN, M.: *Aero-Thermal Investigation of Fixed Rib-Roughened Cooling Passages (Part I+II)*. Published by von Karmann Institute for Fluid Dynamics, Lecture Series 2000-03, 2000.

- [12] CHEN, S., P.; LI, P., W.; CHYU, M., K.; CUNHA, F., J.; ABDEL-MESSA, W.: *Heat Transfer in an Airfoil Trailing Edge Configuration with Shaped Pedestals Mounted Internal Cooling Channel and Pressure Side Cutback*. In Proceedings of ASME Turbo Expo 2006, GT2006-90019, 2006.
- [13] CHO, H. H.; RHEE, D. H.; LEE, D. H.: *Effects of Duct Aspect Ratio on Heat/Mass Transfer with Discrete V-shaped Ribs*. In Proceedings of ASME Turbo Expo 2002, GT2002-38622, 2002.
- [14] CHYU, M., K.; NATARAJAN, V.: *Heat Transfer on the Base Surface of Three-Dimensional Protruding Elements*. International Journal of Heat and Mass Transfer, vol. 39, No.14, pp. 2925-2935, 1996.
- [15] CHYU, M., K.; YU, Y.; DING, H.; DOWNS, J., P.; SOECHTING, F., O.: *Concavity Enhanced Heat Transfer in an Internal Cooling Passage*. Presented at the International Gas Turbine & Aeroengine Congress & Exhibition, 97-GT-437, 1997.
- [16] CORREA, S., M.: *Power Generation and Aero Propulsion Gas Turbines: From Combustion Science to Combustion Technology*. 27th Symposium on Combustion, The Combustion Institute, pp. 1793-1807, 1998.
- [17] DIPPREY, D., F.; SABERSKY, R., H.: *Heat and Momentum Transfer in Smooth and Rough Tubes at Various Prandtl Numbers*. International Journal of Mass and Heat Transfer, vol. 6, pp. 329-353, 1963.
- [18] EKKAD, S., V.; HAN, J., C.: *A Transient Liquid Crystal Thermography Technique for Gas Turbine Heat Transfer Measurements*. Meas. Sci. Technol., vol. 11, pp. 957-968, 2000.
- [19] FLUENT 6.2: *User's Guide*. Fluent Inc., January 2005.
- [20] GAO, X.; SUNDÉN, B.: *Heat Transfer Distribution in Rectangular Ducts with V-shaped Ribs*. Heat and Mass Transfer, vol. 37, pp. 315-320, 2001.
- [21] GRAHAM, A.; SEWALL, E.; THOLE, K. A.: *Flowfield Measurement in a Ribbed Channel Relevant to Internal Turbine Blade Cooling*. International Gas Turbine and Aeroengine Congress and Exposition, Vienna, Austria, ASME, GT2004-53361, 2004.
- [22] GRIFFITH, T., S.; AL-HADHRAMI, L.; HAN, J., C.: *Heat Transfer in Rotating Rectangular Cooling Channels (AR=4) With Dimples*. Journal of Turbomachinery, vol. 125, pp. 555-564, 2003.
- [23] HAN, J., C.; DUTTA, S.: *Internal Convection Heat Transfer and Cooling – An Experimental Approach (Part I+II)*. Published by von Karman Institute for Fluid Dynamics, Lecture Series 1995-05, 1995.

- [24] HAN, J., C.; PARK, J., S.: *Developing Heat Transfer in Rectangular Channels with Rib Turbulators*. International Journal of Heat and Mass Transfer, vol. 31, pp. 183-195, 1988.
- [25] HAN, J. C.; ZHANG, Y. M.; LEE, C. P.: *Augmented Heat Transfer in Square Channels with Parallel, Crossed, and V-shaped Angled Ribs*. ASME Journal of Heat Transfer, vol. 113, pp. 590-596, 1991.
- [26] HANJALIC, K.; LAUNDER, B., M.: *Fully Developed Asymmetric Flow in a Plane Channel*. Journal of Fluid Mechanics, vol. 51, part 2, pp. 301-355, 1972.
- [27] HINZE, J., O.: *Turbulence*. McGraw-Hill Publishing Co., New York, 1975.
- [28] HORLOCK, J., H.: *Advanced Gas Turbine Cycles*. Published by Elsevier Science Ltd, ISBN 0-08-044273-0, 2003.
- [29] HOSNI, M., H.; COLEMAN, H., W.; GARNER, J., W.; TAYLOR, R., P.: *Roughness Element Shape Effects on Heat Transfer and Skin Friction in Rough-wall Turbulent Boundary Layers*. International Journal of Heat and Mass Transfer, vol. 36, pp. 147-153, 1993.
- [30] IRELAND, P., T.; JONES, T., V.: *Liquid Crystal Measurements of Heat Transfer and Surface Shear Stress*. Meas. Sci. Technol., vol. 11, pp. 969-986, 2000.
- [31] KAYS, W., M.; CRAWFORD, M., E.; WEIGAND, B.: *Convective Heat and Mass Transfer*. 4th ed., McGraw-Hill, 2005, ISBN 0-07-246876-9.
- [32] KHALATOV, A., A.: *Heat Transfer and Fluid Mechanics over Surface Indentations (Dimpels)*. Published by the National Academy of Sciences of Ukraine, Institute of Engineering Thermophysics, Kiev, 2005.
- [33] KIM, Y., W.; ARELLANO, L.; VARDAKAS, M.; MOON, H., K.; SMITH, K., O.: *Comparison of Trip-strip/ Impingement/ Dimple Cooling Concepts At High Reynolds Numbers*. In Proceedings of ASME TURBO EXPO, GT2003-38935, 2003.
- [34] KOTULLA, M.; WAGNER, G.; OTT, P.; WEIGAND, B.; VON WOLFERSDORF, J.: *The Transient Liquid Crystal Technique: Influence of Surface Curvature and Finite Wall Thickness*. Journal of Turbomachinery, vol. 127, pp. 175-182, 2005.
- [35] LAU, S. C.; KUKREJA, R. T.; MCMILLAN, R. D.: *Effects of V-shaped Rib Arrays on Turbulent Heat Transfer and Friction of Fully Developed Flow in a Square Channel*. Int. Journal of Heat and Mass Transfer, vol. 34, pp. 1605-1616 1991.
- [36] LAVISION: *PIV System Manual*. Published by LaVision GmbH, Goettingen, Germany, 2002.

- [37] LECHNER, C.; SEUME, J.: *Stationäre Gasturbinen (German)*. Published by Springer-Verlag, ISBN 3-540-42831-3, 2003.
- [38] LEE, E.; WRIGHT, L. M.; HAN, J. C.: *Heat Transfer in Rotating Rectangular Channels (AR=4:1) with V-shaped and Angled Rib Turbulators with and without Gaps*. In Proceedings of ASME Turbo Expo 2003, GT2003-38900, 2003.
- [39] LIN, Y., L.; SHIH, T.; CHYU, M., K.: *Computations of Flow and Heat Transfer in a Channel with Rows of Hemispherical Cavities*. Presented at the International Gas Turbine & Aeroengine Congress & Exhibition, 99-GT-263, 1999.
- [40] LIU, Y., H.; WRIGHT, L. M.; FU, W., L.; HAN, J. C.: *Rib Spacing Effect on Heat Transfer and Pressure Loss in Rotating Two Pass Rectangular Channel (AR=1:2) with 45° Angled Ribs*. In Proceedings of ASME Turbo Expo 2006, GT2006-90368, 2006.
- [41] MAHMOOD, G., I.; HILL, M. L.; NELSON, D. L., LIGRANI, P., M.; MOON, H., K.; GLEZER, B.: *Local Heat Transfer and Flow Structure on and Above a Dimpled Surface in a Channel*. Journal of Turbomachinery, vol. 123, pp. 115-123, 2001.
- [42] MAURER., M.; VON WOLFERSDORF, J.; GRITSCH, M.: *An Experimental and Numerical Study of Heat Transfer and Pressure Loss in a Rectangular Channel with V-Shaped Ribs*. In Proceedings of ASME Turbo Expo 2006, GT2006-90006, 2006.
- [43] MOMIN, A. E.; SAINE, J. S.; SOLANKI, S. C.: *Heat Transfer and Friction in Solar Air Heater Duct with V-shaped Rib Roughness on Absorber Plate*. Int. Journal of Heat and Mass Transfer, vol. 45, pp. 3383-3396, 2002.
- [44] MOON, H., K.; O'CONNELL, T.; GLEZER, B.: *Channel Height Effect on Heat Transfer and Friction in a Dimpled Passage*. Journal of Engineering for Gas Turbines and Power, vol. 122, pp. 307-313, 2000.
- [45] MOON, S., W.; LAU, S., C.: *Turbulent Heat Transfer Measurements on a Wall with Concave and Cylindrical Dimples in a Square Channel*. In Proceedings of ASME TURBO EXPO, GT-2002-30208, 2002.
- [46] MOSKVINA, G., V.; MOSTINSKII, I., L.; POLEZHAEV, YU., V.; SELIVERSTOV, E., M.: *Problems of and Prospects for the Investigation of the Thermal Conditions of Blades of High-Temperature Gas Turbines (a Review Based on Presentations to the Third Russian National Conference on Heat Transfer)*. High Temperature, vol. 41, No. 5, pp. 708-723, 2003.

- [47] NAGOVA, G., P.: *Effective Blade Cooling Techniques for High Performance Gas Turbines (Russian)*. Published by the Moscow Aviation Institute, Russia, p. 100, 1996.
- [48] NEALY, D., A.; REIDER, S., B.; MONGIA, H., C.: *Alternate Cooling Configurations for Gas Turbine Combustion Systems*. In proceedings of AGARD conference no. 390, pp. 25.1-25.25, 1985.
- [49] NIKURADSE, J.: *Strömungsgesetze in rauhen Rohren (German)*. Kaiser-Wilhelm-Inst. F. Strömungsforschung, Göttingen, VDI-Verlag, 1933.
- [50] POSER, R.; VON WOLFERSDORF, J.; LUTUM, E.: *Advanced Evaluation of Transient Heat Transfer Experiments Using Thermochromic Liquid Crystals*. In Proceedings of 7th European Turbomachinery Conference ETC, paper no. 63, 2007.
- [51] POSER, R.; VON WOLFERSDORF, J.; SEMMLER, K.: *Transient Heat Transfer Experiments in Complex Passages*. In Proceedings of ASME Summer Heat Transfer Conference, HT2005-72260, 2005.
- [52] RAFFEL, M.; WILLERT, C.; KOMPENHANS, J.: *Particle Image Velocimetry: A Practical Guide*. Published by Springer Verlag, Berlin, Germany, 2001.
- [53] SCHLICHTING, H.: *Experimentelle Untersuchung zum Rauheitsproblem (German)*. Ingenieur-Archiv, Germany, vol. 7, pp. 1-34, 1936.
- [54] SCHULZ, A.: *Combustor Liner Cooling Technology in Scope of Reduced Pollutant Formation and Rising Thermal Efficiencies*. Heat Transfer in Gas Turbine Systems, Annals of the New York Academy of Science, vol. 934, pp. 135-146, 2001.
- [55] SIGAL, A.; DANBERG, J., E.: *New Correlation of Roughness Density Effect on the Turbulent Boundary Layer*. AIAA Journal, vol. 28, pp. 554-556, 1990.
- [56] SU, G.; TENG, S.; CHEN, H. C.; HAN, J. C.: *Computation of Flow and Heat Transfer in Rotating Rectangular Channels (AR=4) with V-shaped Ribs by a Reynolds Stress Turbulence Model*. In Proceedings of ASME Turbo Expo 2003, GT2003-38348, 2003.
- [57] TASLIM, M. E.; LI, T.; KERCHER, D. M.: *Experimental Heat Transfer and Friction in Channels Roughened With Angled, V-Shaped, and Discrete Ribs on Two Opposite Walls*. ASME Journal of Turbomachinery, vol. 118, pp. 20-28, 1996.
- [58] VOGEL, G.: *DIPS - Digital Image Processing System for liquid crystal measurements - Manual*. EPFL, Lausanne, Switzerland, 2000.

-
- [59] WRIGHT, L. M.; FU W. L.; HAN, J. C.: *Thermal Performance of Angled, V-shaped, and W-shaped Rib Turbulators in Rotating Rectangular Cooling Channels (AR=4:1)*. In Proceedings of ASME Turbo Expo 2004, GT2004-54073, 2004.
- [60] ZHOU, F.; ACHARYA, S.: *Mass/Heat Transfer in Dimpled Two-Pass Coolant Passages with Rotation*. Heat Transfer in Gas Turbine Systems, Annals of the New York Academy of Science, vol. 934, pp. 424-431, 2001.

Appendix

A PIV measurement

As described in chapter 4.6, the mean velocity profiles from the numerical computation of test cases WW10-1s and WW5-1s show differences compared to the mean velocity profile of test cases with W-shaped ribs. In the case of WW-shaped ribs, the main part of the core flow is shifted towards the smooth channel wall opposite to the ribbed channel wall. A 2D-PIV measurement is conducted to support the numerically computed results.

Measurement technique

The 2D-PIV measurement technique is a non-invasive measurement method. Due to the nature of this measurement technique, two velocity components can be captured in a single experiment. For obtaining all three velocity components, a 3C-PIV measurement is required, which uses two CCD cameras instead of only one.

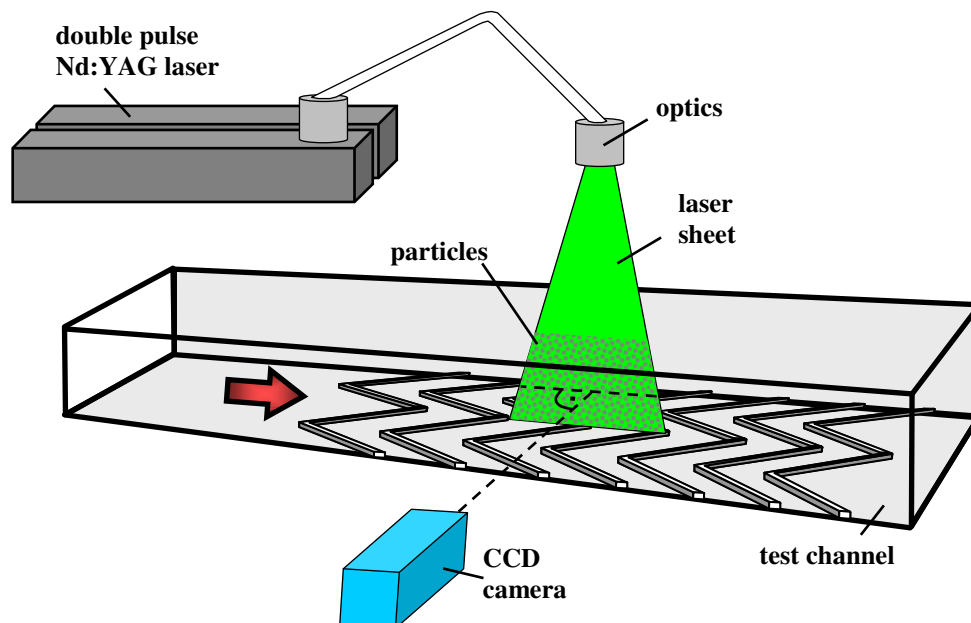


Fig. A .1: Setup of the 2D-PIV measurement method

The basic idea behind this technique is briefly described in this chapter and well documented in literature (e.g. [36], [52]). Particles are inserted into the air flow assuming that their velocity is equal to the velocity of the surrounding flow field. A laser system is used to create a thin sheet of laser light at the measurement location. During an experiment, the CCD camera takes two pictures of the particles, which are illuminated by the pulsed laser light in a relatively short period of time. Knowing the

period of time between the two pictures and the displacement of the single particles, the velocity components can be calculated. The experimental setup is presented in Fig. A.1.

Within this study, two test cases are investigated with the 2D-PIV measurement technique. Those test cases are test case W10-1s and test case WW10-1s. The velocity components in x- and z-direction are obtained at a total of three measurement locations for the two test cases. The velocity component in y-direction could not be captured with the present measurement configuration. As a consequence, the mean velocity is derived by neglecting the velocity component in the y-direction. The differences compared to the true mean velocity are considered to be low. The sketch of the measurement locations is presented in Fig. A.2.

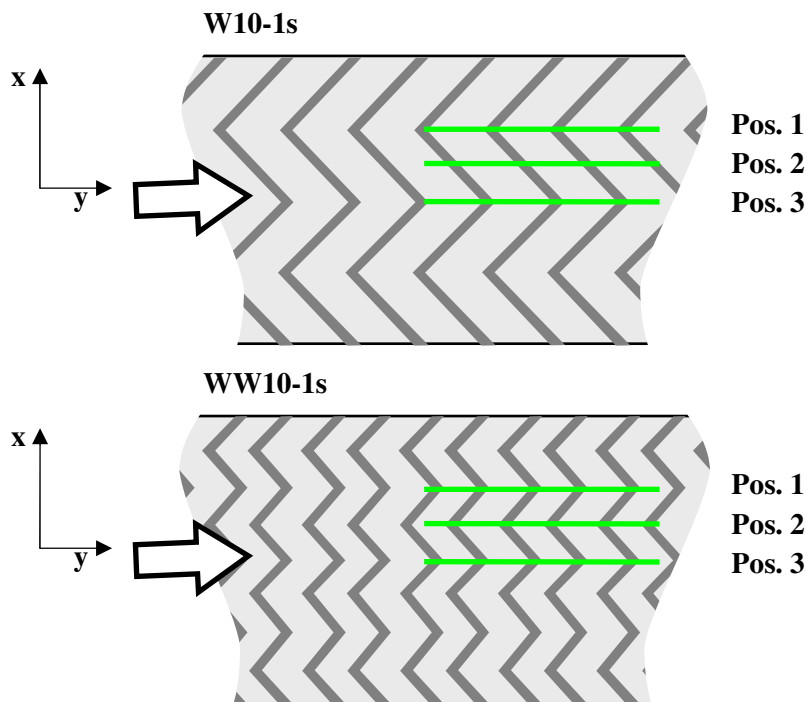


Fig. A.2: Measurement positions 2D-PIV for test cases W10-1s and WW10-1s

Velocity field and profiles

For test case W10-1s, the mean velocity profiles and the resulting streamtraces at the three measurement locations are presented in Fig. A.3. Additionally, numerically obtained data is provided.

At position 1 and 2 the streamtraces of the numerical computation reveal that the air flow is diverted towards the ribbed channel wall. This is in good agreement with the velocity profile provided by the 2D-PIV measurement. Proceeding from position 3 to position 1, the position of the maximum mean velocity is shifted towards the ribbed channel wall. This trend is also predicted correctly by the numerical computation. At position 3 of the experimental data, the streamtraces are diverted away from the ribbed channel wall, which is also predicted correctly by the numerical computation.

On the other hand, the position of the maximum mean velocity is found to be closer to the ribbed channel wall in the case of the numerical computation. Additionally, it has to be mentioned, that the numerical computation is not capable to predict the exact local velocity levels of the experiment.

Looking at the obtained data at the three measurement locations, it can be seen, that close to the rib tip, the air flow above the ribbed channel wall is lead towards the ribbed channel wall. The experiments show clearly, that parts of the core flow are sucked into the region between two successive ribs. Close to the trailing edge of the rib, the air flow is ejected back into the core flow. Similar findings are found for the numerical computation, which has been used to investigate the flow field in chapter 4.4.

W10-1s

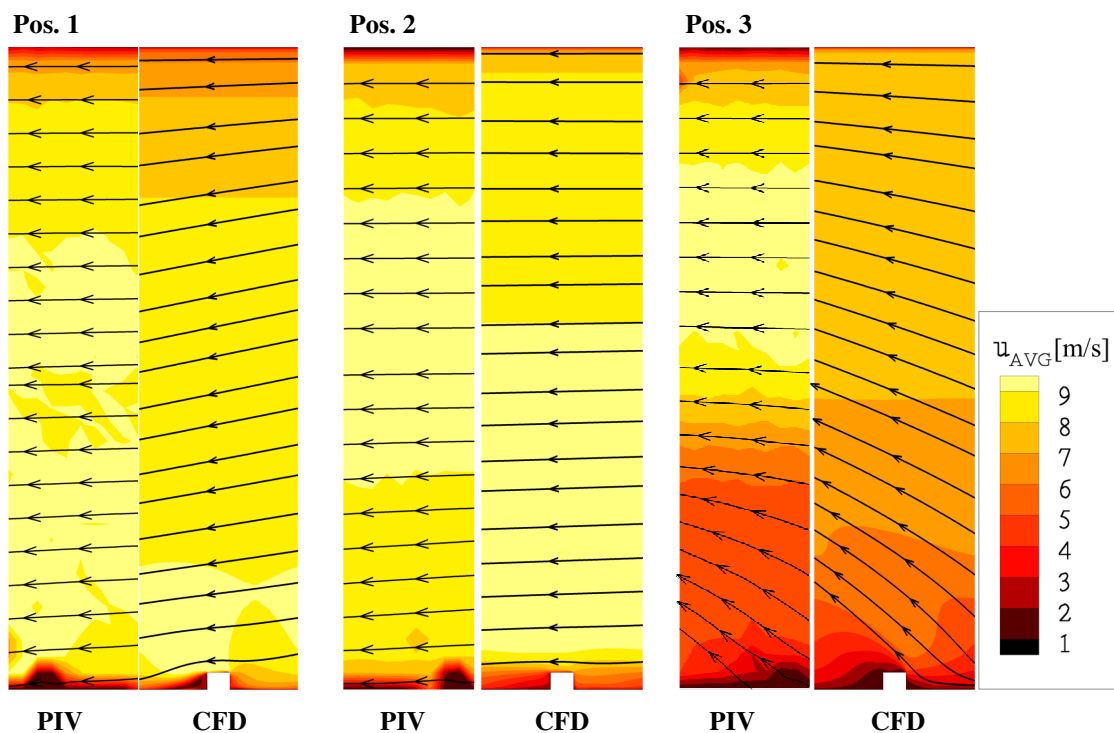


Fig. A.3: Velocity profiles and streamtraces of 2D-PIV measurement and CFD from test case W10-1s at $Re_D \sim 130K$

The corresponding data of test case WW10-1s is presented in Fig. A.4. Compared the presented measurement locations above the rib tip, the position of the maximum mean velocity is closer to the ribbed channel wall in the case of test case W10-1s. It seems that for convective cooling channels with WW-shaped ribs, the main part of the air flow is located around the channel mid-plane or closer to the smooth channel wall opposite to the ribbed channel wall. This is in contrast to the obtained velocity distribution of test case W10-1s, where high levels of mean velocity are also found close to the ribbed channel wall.

As found for test case W10-1s, the numerical computation is able to predict the trends correctly, but fails to give exact values comparing the numerically and experimentally obtained velocity profiles. For the numerical computation the parts of the flow with higher levels of velocity are predicted to be closer to the smooth channel wall opposite to the ribbed channel wall.

With the experimental data of the velocity profiles, it could be demonstrated, that there are differences between the velocity distribution of W-shaped and WW-shaped channels. It is assumed, that due to the rib geometry of the WW-shaped rib, there are more trailing edges, where the air flow between two successive ribs is ejected back into the core flow. As a result, there are more locations across the ribbed channel wall, where this momentum seems to generally shift the core flow away from the ribbed channel wall as concluded in chapter 4.6.

WW10-1s

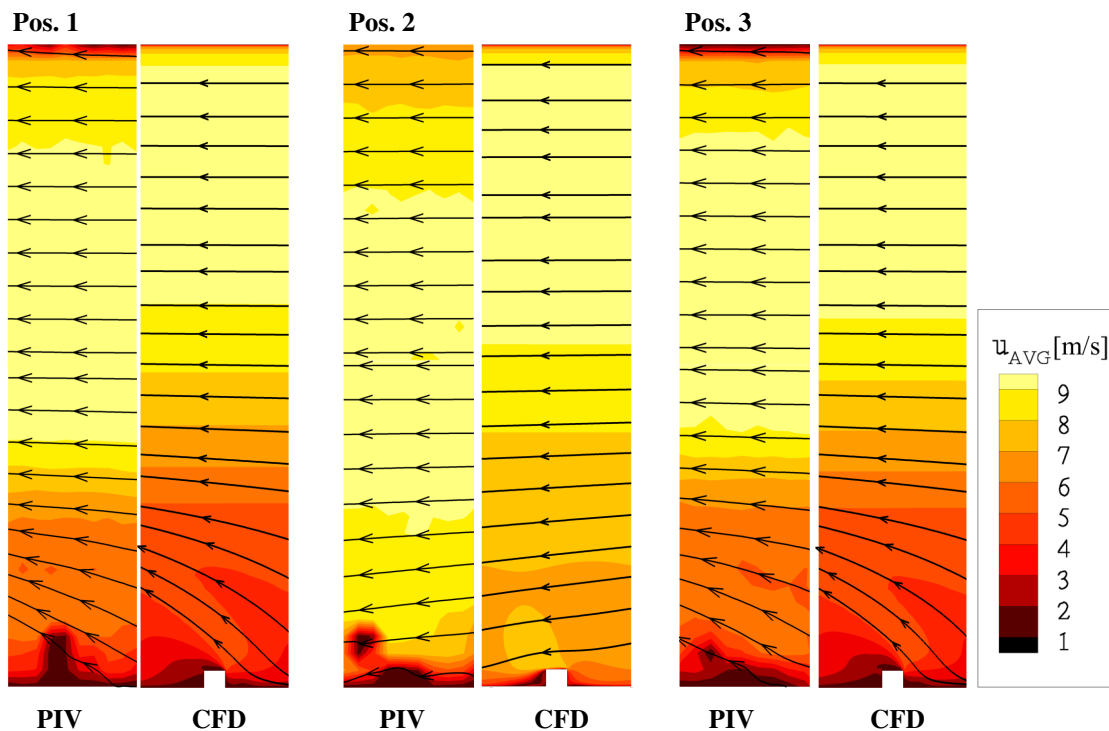


Fig. A.4: Velocity profiles and streamtraces of 2D-PIV measurement and CFD from test case WW10-1s at $Re_D \sim 130K$

B Error analysis

For the present study, a standard uncertainty analysis is applied. The relative uncertainties of the different parameters are derived based on the Gaussian error propagation equation. To give an example, a typical Function F, which depends on

various variables, is presented in (B.1). The corresponding Gaussian error propagation equation is given in (B.2).

$$F = F(x, y, z, \dots) \quad (\text{B.1})$$

$$\Delta F = \sqrt{\left(\frac{\partial F}{\partial x} \Delta x\right)^2 + \left(\frac{\partial F}{\partial z} \Delta z\right)^2 + \left(\frac{\partial F}{\partial z} \Delta z\right)^2 + \dots} \quad (\text{B.2})$$

In this equation, Δx , Δy and Δy represent the confidence interval of the single variable. The confidence intervals of the single parameters are specified and as a result, the confidence interval ΔF of the investigated function is obtained.

Reynolds number

As mentioned in chapter 2.1 and 2.2, the Reynolds number in the test section is measured by calculating the entering mass flow via pressure readings in the inlet nozzle. The complete equation to compute the Reynolds number is given in (B.3).

$$\text{Re}_D = \frac{D_h A_{NOZ} c_f \sqrt{2 \Delta p_{NOZ} \rho_{NOZ}}}{\mu_{MEAS} A_{MEAS}} \quad (\text{B.3})$$

As can be seen from this equation, the Reynolds number depends on various parameters as presented in (B.4).

$$\text{Re}_D = \text{Re}_D(D_h, A_{NOZ}, \Delta p_{NOZ}, \rho_{NOZ}, \mu_{MEAS}, A_{MEAS}) \quad (\text{B.4})$$

The corresponding Gaussian error propagation equation is given as equation (B.5).

$$\begin{aligned} (\Delta \text{Re}_D)^2 &= \left(\frac{\partial \text{Re}_D}{\partial D_h} \Delta D_h\right)^2 + \left(\frac{\partial \text{Re}_D}{\partial A_{NOZ}} \Delta A_{NOZ}\right)^2 \\ &+ \left(\frac{\partial \text{Re}_D}{\partial \Delta p_{NOZ}} \Delta(\Delta p_{NOZ})\right)^2 + \left(\frac{\partial \text{Re}_D}{\partial \rho_{NOZ}} \Delta \rho_{NOZ}\right)^2 \\ &+ \left(\frac{\partial \text{Re}_D}{\partial \mu_{MEAS}} \Delta \mu_{MEAS}\right)^2 + \left(\frac{\partial \text{Re}_D}{\partial A_{MEAS}} \Delta A_{MEAS}\right)^2 \end{aligned} \quad (\text{B.5})$$

The variable values and their confidence intervals of a typical experiment are as follows:

$D_h = 0.2667 \text{ m}$	$\Delta D_h = 3\text{e-}3 \text{ m} (\approx 1 \% \text{ of } D_h)$
$A_{NOZ} = 0.0394 \text{ m}^2$	$\Delta A_{NOZ} = 4\text{e-}4 \text{ m}^2 (\approx 1 \% \text{ of } A_{NOZ})$
$\Delta p_{NOZ} = 2000 \text{ Pa}$	$\Delta(\Delta p_{NOZ}) = 40 \text{ Pa} (\approx 2 \% \text{ of } \Delta p_{NOZ})$
$\rho_{NOZ} = 1.12 \text{ kg/m}^3$	$\Delta \rho_{NOZ} = 1\text{e-}2 \text{ kg/m}^3 (\approx 1 \% \text{ of } \rho_{NOZ})$
$\mu_{MEAS} = 1.8\text{e-}5 \text{ kg/(ms)}$	$\Delta \mu_{MEAS} = 2\text{e-}7 \text{ kg/(ms)} (\approx 1 \% \text{ of } \mu_{MEAS})$
$A_{MEAS} = 0.08 \text{ m}^2$	$\Delta A_{MEAS} = 8\text{e-}4 \text{ m}^2 (\approx 1 \% \text{ of } A_{MEAS})$

For this pressure readings and air properties a Reynolds number of $Re_D \approx 485K$ is calculated. The confidence level is derived as:

$$\Delta Re_D = 11000 (\approx 2.5 \% \text{ of } Re_D)$$

Friction factor

The measurement of the friction factor in the test channel is described in chapter 2.3. Assuming similar air properties in the inlet nozzle and the test channel, the complete equation to obtain the friction factor in the test channel is given in (B.6).

$$f = \frac{(\Delta p / \Delta x) D_h A_{MEAS}^2}{4 A_{NOZ}^2 c_f^2 \Delta p_{NOZ}} \quad (B.6)$$

Looking at the above equation, the friction factor depends on the following variables:

$$f = f((\Delta p / \Delta x), D_h, A_{MEAS}, A_{NOZ}, \Delta p_{NOZ}) \quad (B.7)$$

In equation (B.8), the Gaussian error propagation equation is presented for the friction factor.

$$\begin{aligned} (\Delta f)^2 = & \left(\frac{\partial f}{\partial (\Delta p / \Delta x)} \Delta (\Delta p / \Delta x) \right)^2 \\ & + \left(\frac{\partial f}{\partial D_h} \Delta D_h \right)^2 + \left(\frac{\partial f}{\partial A_{MEAS}} \Delta A_{MEAS} \right)^2 \\ & + \left(\frac{\partial f}{\partial A_{NOZ}} \Delta A_{NOZ} \right)^2 + \left(\frac{\partial f}{\partial \Delta p_{NOZ}} \Delta (\Delta p_{NOZ}) \right)^2 \end{aligned} \quad (B.8)$$

For a typical data set, the variable values and their confidence intervals are given as the following:

$(\Delta p / \Delta x) = 200 \text{ Pa/m}$	$\Delta (\Delta p / \Delta x) = 20 \text{ Pa/m} (\approx 10 \% \text{ of } (\Delta p / \Delta x))$
$D_h = 0.2667 \text{ m}$	$\Delta D_h = 3e-3 \text{ m} (\approx 1 \% \text{ of } D_h)$
$A_{MEAS} = 0.08 \text{ m}^2$	$\Delta A_{MEAS} = 8e-4 \text{ m}^2 (\approx 1 \% \text{ of } A_{MEAS})$
$A_{NOZ} = 0.0394 \text{ m}^2$	$\Delta A_{NOZ} = 4e-4 \text{ m}^2 (\approx 1 \% \text{ of } A_{NOZ})$
$\Delta p_{NOZ} = 2000 \text{ Pa}$	$\Delta (\Delta p_{NOZ}) = 40 \text{ Pa} (\approx 2 \% \text{ of } \Delta p_{NOZ})$

For the above data set, the measurement of the friction factor ratio is conducted for a Reynolds number of $Re_D \approx 485K$. The confidence interval of the friction factor is computed as:

$$\Delta f = 0.0024 (\approx 10.5 \% \text{ of } f)$$

It proved to be difficult to fit the regression line to the experimentally obtained pressure distribution. This explains the relatively large confidence interval of the regression line gradient $\Delta p / \Delta x$ of around 10 %. Finally, it has to be noticed, that for lower Reynolds

numbers or lower pressure losses in the test channel the measurement uncertainties tend to increase.

Heat transfer coefficient (steady measurement technique)

For the steady measurement technique, the heat transfer coefficient is obtained as described in chapter 2.5. The governing equation to compute the heat transfer equation is presented in (B.9).

$$h = \frac{(U_{EL}^2 / R_{EL}) - \dot{q}_{RLOSS} - \dot{q}_{CLOSS}}{A_{FOIL} (T_{TLC} - T_B)} \quad (B.9)$$

Hence, the heat transfer coefficient for the steady measurement technique is defined by the following variables:

$$h = h(U_{EL}, R_{EL}, \dot{q}_{RLOSS}, \dot{q}_{CLOSS}, A_{FOIL}, T_{TLC}, T_B) \quad (B.10)$$

The Gaussian error propagation equation of the heat transfer coefficient for the steady measurement technique is given in (B.11).

$$\begin{aligned} (\Delta h)^2 = & \left(\frac{\partial h}{\partial U_{EL}} \Delta U_{EL} \right)^2 + \left(\frac{\partial h}{\partial R_{EL}} \Delta R_{EL} \right)^2 \\ & + \left(\frac{\partial h}{\partial \dot{q}_{RLOSS}} \Delta \dot{q}_{RLOSS} \right)^2 + \left(\frac{\partial h}{\partial \dot{q}_{CLOSS}} \Delta \dot{q}_{CLOSS} \right)^2 \\ & + \left(\frac{\partial h}{\partial A_{FOIL}} \Delta A_{FOIL} \right)^2 + \left(\frac{\partial h}{\partial T_{TLC}} \Delta T_{TLC} \right)^2 + \left(\frac{\partial h}{\partial T_B} \Delta T_B \right)^2 \end{aligned} \quad (B.11)$$

A characteristic data set taken from a steady measurement technique experiment and the corresponding confidence intervals of the variables are given as the following:

$U_{EL} = 11 \text{ V}$	$\Delta U_{EL} = 0.2 \text{ V} (\approx 2 \% \text{ of } U_{EL})$
$R_{EL} = 0.415 \ \Omega$	$\Delta R_{EL} = 4.15\text{e-}3 (\approx 1 \% \text{ of } R_{EL})$
$\dot{q}_{RLOSS} = 51 \text{ W/m}^2$	$\Delta \dot{q}_{RLOSS} = 2.5 \text{ W/m}^2 (\approx 5 \% \text{ of } \dot{q}_{RLOSS})$
$\dot{q}_{CLOSS} = 20 \text{ W/m}^2$	$\Delta \dot{q}_{CLOSS} = 1 \text{ W/m}^2 (\approx 5 \% \text{ of } \dot{q}_{CLOSS})$
$A_{FOIL} = 0.226 \text{ m}^2$	$\Delta A_{FOIL} = 1\text{e-}2 \text{ m}^2 (\approx 5 \% \text{ of } A_{FOIL})$
$T_{TLC} = 311 \text{ K}$	$\Delta T_{TLC} = 0.4 \text{ K} (\approx 0.13 \% \text{ of } T_{TLC})$
$T_B = 295 \text{ K}$	$\Delta T_B = 0.2 \text{ K} (\approx 0.13 \% \text{ of } T_B)$

For the above data set, a heat transfer coefficient of $h = 62.1 \text{ W}/(\text{m}^2\text{K})$ is calculated. For the confidence interval from the Gaussian error propagation equation, the following value is obtained:

$$\Delta h = 4.7 \text{ W}/(\text{m}^2\text{K}) (\approx 8 \% \text{ of } h)$$

For lower voltage levels of around $U_{EL} = 4$ V, which results in heat transfer coefficients of $h = 6$ W/(m²K), higher uncertainties are obtained. Here, the confidence level of the heat transfer coefficient increases to $\Delta h \approx 11$ % of h .

Heat transfer coefficient (transient measurement technique)

As described in chapter 2.6, the evaluation of the heat transfer coefficient for the transient measurement technique is more complex compared to the steady measurement technique. Here, the heat transfer coefficient can not be calculated directly, because the governing equation is an implicit equation.

To keep the uncertainty analysis manageable, the transient experiment is considered to possess an ideal temperature step. Therefore, the uncertainty analysis is conducted for equation (2.10). Introducing a dimensionless temperature gradient Θ_w , this equation is transferred to:

$$\Theta_w = 1 - e^{-\beta^2} \operatorname{erfc}(\beta)$$

$$\text{with } \beta = h \sqrt{\frac{t}{\rho_w c_{p,w} k_w}} \quad (\text{B.12})$$

A similar approach has been reported by Poser et al. [51]. In their study, the authors considered that the uncertainty of the heat transfer coefficient depends mainly on the temperature and time measurement. For the Gaussian error propagation equation of the implicit problem, they proposed equation (B.13).

$$(\Delta h)^2 = \left(\frac{\partial h}{\partial \Theta_w} \Delta \Theta_w \right)^2 + \left(\frac{\partial h}{\partial t} \Delta t \right)^2 \quad (\text{B.13})$$

To be able to compute the confidence interval of the heat transfer coefficient, equation (B.13) is transferred to:

$$(\Delta h)^2 = \frac{1}{\left(\frac{\partial \Theta_w}{\partial h} \right)^2} (\Delta \Theta_w)^2 + \frac{\left(\frac{\partial \Delta \Theta_w}{\partial t} \right)^2}{\left(\frac{\partial \Delta \Theta_w}{\partial h} \right)^2} (\Delta t)^2 \quad (\text{B.14})$$

For the uncertainty analysis, the confidence levels of the dimensionless temperature and the time measurement are set to $\Delta \Theta_w = 0.01$ and $\Delta t = 0.2$ s. The resulting confidence level of the heat transfer coefficient has been computed numerically by Poser et al. [51] and is presented in Fig. B.1.

As can be seen from this figure, the uncertainty level of the heat transfer coefficient tends to increase for dimensionless temperature gradients close to $\Theta_w = 1$ and close to $\Theta_w = 0$. Also the level of the heat transfer coefficient is important. For heat transfer coefficients above $h = 500$ W/(m²K), the TLC indication time is relatively small and therefore the relative time uncertainty large, leading to higher uncertainties for lower

dimensionless temperature gradients. Therefore, the dimensionless temperature gradient should stay above $\Theta_w = 0.4$ to conserve moderate uncertainty levels for high heat transfer coefficients.

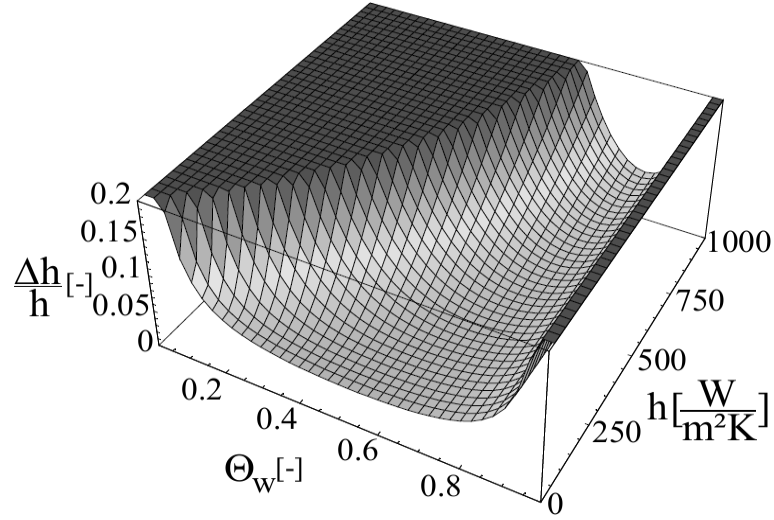


Fig. B.1: Confidence interval of heat transfer coefficient (taken from [51])

In the current study, the measured heat transfer coefficients are in the range of $h = 10 \text{ W/m}^2\text{K}$ and $h = 400 \text{ W/m}^2\text{K}$, Θ_w was set to values between $\Theta_w = 0.25$ and $\Theta_w = 0.6$. In this range the analysis from Poser et al. [51] delivers relative uncertainties for the heat transfer coefficient between 5 % and 20 %.

Heat transfer coefficient (lumped heat-capacitance method)

As described in chapter 2.7, it is possible to obtain an area-averaged heat transfer coefficient on the rib itself with the lumped heat-capacitance method. The area-averaged heat transfer coefficient on the rib is computed with the following equation.

$$h_{RIB} = -\frac{m_{RIB} c_{RIB}}{A_{RIB} t} [\ln(1 - \Theta_{RIB})] \quad (\text{B.15})$$

As seen from equation (B.15), the heat transfer coefficient is defined by the following variables:

$$h = h(m_{RIB}, c_{RIB}, A_{RIB}, t, \Theta_{RIB}) \quad (\text{B.16})$$

The Gaussian error propagation equation of the heat transfer coefficient derived with the lumped heat-capacitance method is presented in equation (B.17).

$$\begin{aligned} (\Delta h_{RIB})^2 = & \left(\frac{\partial h_{RIB}}{\partial m_{RIB}} \Delta m_{RIB} \right)^2 + \left(\frac{\partial h_{RIB}}{\partial c_{RIB}} \Delta c_{RIB} \right)^2 \\ & + \left(\frac{\partial h_{RIB}}{\partial A_{RIB}} \Delta A_{RIB} \right)^2 + \left(\frac{\partial h_{RIB}}{\partial t} \Delta t \right)^2 + \left(\frac{\partial h_{RIB}}{\partial \Theta_{RIB}} \Delta \Theta_{RIB} \right)^2 \end{aligned} \quad (\text{B.17})$$

For this measurement method, a characteristic data set taken from an experiment and the corresponding confidence intervals of the variables are given as the following:

$$\begin{array}{ll}
 m_{\text{RIB}} = 4.35\text{e-}2 \text{ kg} & \Delta m_{\text{RIB}} = 1.3\text{e-}3 \text{ kg } (\approx 3 \% \text{ of } m_{\text{RIB}}) \\
 c_{\text{RIB}} = 860 \text{ J/(kgK)} & \Delta c_{\text{RIB}} = 25 \text{ J/(kgK)} (\approx 3 \% \text{ of } c_{\text{RIB}}) \\
 A_{\text{RIB}} = 9\text{e-}3 \text{ m}^2 & \Delta A_{\text{RIB}} = 2.7\text{e-}4 \text{ m}^2 (\approx 3 \% \text{ of } A_{\text{RIB}}) \\
 t = 10 \text{ s} & \Delta t = 0.2 \text{ s } (\approx 2 \% \text{ of } t) \\
 \Theta_{\text{RIB}} = 0.2 & \Delta \Theta_{\text{RIB}} = 1\text{e-}2 (\approx 5 \% \Theta_{\text{RIB}})
 \end{array}$$

For the given data set, an area-averaged heat transfer coefficient of $h_{\text{RIB}} = 92.3 \text{ W/(m}^2\text{K)}$ is computed. The corresponding confidence interval of the Gaussian error propagation equation is reported as:

$$\Delta h_{\text{RIB}} = 7.3 \text{ W/(m}^2\text{K)} (\approx 8 \% \text{ of } h_{\text{RIB}})$$

For the present study, the dimensionless temperature gradients Θ_{RIB} varies between $\Theta_{\text{RIB}} = 0.15$ and $\Theta_{\text{RIB}} = 0.4$. The area-averaged heat transfer coefficient is computed to be between $h_{\text{RIB}} = 20 \text{ W/(m}^2\text{K)}$ and $h_{\text{RIB}} = 320 \text{ W/(m}^2\text{K)}$. Within this range, the confidence interval remains within 10 % of the area-averaged heat transfer coefficient.

Resume

Name: Michael Maurer
Address: Hauptstr. 47
79365 Rheinhausen
Germany
Date of birth: 16.05.1978
Nationality: German



Work Experience

- 07/2007-today Employed as a combustor design engineer for ALSTOM Power in Baden, Switzerland
- 01/2004-06/2007 Worked as a research associate at the Institute of Aerospace Thermodynamics at the Universität Stuttgart, Germany
- Managed the research subproject: "Efficient convective cooling techniques for gas turbine combustors" within the KW21 research project sponsored by ALSTOM Power and the Ministry of Baden-Württemberg
- 10/2000-04/2001 Internship at the Precision Casting Facility of ROLLS-ROYCE in Derby, England
- 02/1999-03/1999 Internship at the company BRAUN FORMENBAU in Bahlingen, Germany
- 07/1998-08/1998 Internship at the company METALLBAU GROESCH, Kappel, Germany

Education

- 10/1998-12/2003 Received degree in aerospace engineering from the Universität Stuttgart, Germany
- Developed expertise in thermodynamics and aerodynamics
- 09/1989-06/1997 Received diploma from German secondary school qualifying for university admission, Heimschule St. Landolin, Ettenheim, Germany